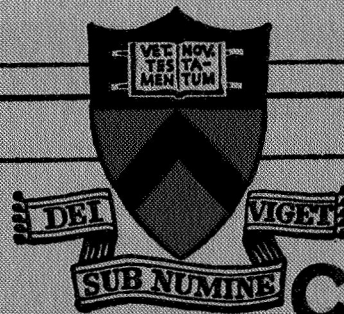


N69-34952
NASA CR 104138

Prepared for
National Aeronautics
and Space Administration

QUASI-STEADY PLASMA ACCELERATION

Report 859*



CASE FILE
COPY

PRINCETON UNIVERSITY
DEPARTMENT OF
AEROSPACE AND MECHANICAL SCIENCES

NASA Research Grant NGL-31-001-005
(Supplement 7)

Prepared for
National Aeronautics
and Space Administration

QUASI-STEADY PLASMA ACCELERATION

Report 859*

Prepared by *Kenn E. Clark*
KENN E. CLARK

Approved by *Robert G. Jahn*
ROBERT G. JAHN
Professor of Aerospace Sciences
and Research Leader

*This report is a reproduction in entirety of the Ph.D. dissertation of Mr. Kenn E. Clark. It is submitted to the sponsor and to the distribution list in this form both as a presentation of the technical material, and as an indication of the academic program supported by this Grant.

Reproduction, translation, publication, use and disposal in whole, or in part, by or for the United States Government is permitted.

May 1969

School of Engineering and Applied Science
Department of Aerospace and Mechanical Sciences
Guggenheim Aerospace Propulsion Laboratories
PRINCETON UNIVERSITY
Princeton, New Jersey

ABSTRACT

A steady state acceleration phase has been shown to occur in a coaxial electrode geometry during the synchronized application of tailored pulses of mass flow and current. This diffuse discharge form, characterized by a stabilized current distribution, constant voltage and current, and a steady argon mass flow rate of up to 50 g/sec, is of considerable interest as both a pulsed thruster and as a simulator of the self-field MPD arcjet over a power range from 100 kW to 100 MW. Terminal voltage measurements, taken over a wide range of power and mass flow rate, are sufficiently precise to allow discrimination among several theoretical models of the acceleration process. Kerr-cell photographs and experimental maps of the current distribution in the exhaust plume and interelectrode region clearly show the rapid transition to this steady configuration, as well as characteristic arc behavior for mass starvation and mass overfeed.

TABLE OF CONTENTS

		Page
Title Page		i
Abstract		ii
Table of Contents		iii
List of Illustrations		v
 Chapter		
1	HISTORICAL BACKGROUND.	1
2	THE MAGNETOPLASMADYNAMIC ARCJET.	10
	I. Introduction	10
	II. Early Observations	14
	III. Mechanisms	23
	IV. Models	29
	V. Summary.	38
3	PULSED ACCELERATORS.	40
	I. Introduction	40
	II. Early Observations	40
	III. Experimental Characteristics	42
	IV. Extended Pulse Operation	48
4	DESIGN CONSIDERATIONS AND REQUIREMENTS	63
	I. Introduction	63
	II. Current Distribution	63
	III. Mass Flow Rate	64
	IV. Other Considerations	75
	V. System Requirements.	77
5	SYSTEM DESIGN.	81
	I. Current Pulse-forming Network.	81
	II. Mass Injection System.	86
	A. Early Systems	86
	B. System Modification	90
	C. Final Configuration	95
	III. Geometry	110
6	RESULTS I; TERMINAL MEASUREMENTS.	120
	I. Introduction	120
	II. Voltage Data	121
	III. Discussion	131

TABLE OF CONTENTS-contd.

	Page
Chapter	
7	RESULTS II: DISCHARGE STRUCTURE 150
	I. Introduction 150
	II. Photographic Studies 150
	III. Conduction Current Distribution. 156
	IV. Discussion 168
8	SUMMARY AND FUTURE WORK. 171
	I. Summary. 171
	II. Future Work. 173
	REFERENCES. 178

LIST OF ILLUSTRATIONS

Figure		Page
1-1	Comparison of current sheet propagation patterns. . .	4
2-1	Specific impulse and thrust density of various propulsion devices.	11
2-2	30-kW radiation-cooled arcjet engine (Ref. 26). . .	15
2-3	Magnetoplasmadynamic thruster efficiency variation with specific impulse (Ref. 13)	17
2-4	Various MPD thruster configurations	19
2-5	MPD arcjet performance with various tank pressures (Ref. 34)	22
2-6	Experimental axial current variation with axial distance.	26
2-7	Measured thrust as a function of arc current for argon and nitrogen (Ref. 42).	28
3-1	Early pulsed thruster (Ref. 2).	47
3-2	Early extended pulse thruster with external magnetic field (Ref. 58).	49
3-3	Switch and pinch-orifice chambers (Ref. 9).	53
3-4	Paschen curve for argon with 2-in. gap (Ref. 64). . .	54
3-5	Current profiles with 9-in. dia. exhaust vessel; 0.12 torr argon, 200 kA x 5 μ sec pulse.	56
3-6	Schematic of early shock tube mass injection system	57
3-7	Large anode with exhaust orifice inside plexiglas vacuum tank	60
3-8	Enclosed current contours in large plexiglas exhaust tank, shock tube injection, 30 kA x 80 μ sec pulse	61
4-1	Mass flow for purely electromagnetic thrust	66
4-2	a) Circuit diagram of fast ionization gauge, with b) typical response oscillogram and c) calibration curve	69
4-3	Pressure development at center of pinch-orifice chamber	71

LIST OF ILLUSTRATIONS-contd.

Figure		Page
4-4	Axial pressure profiles along centerline of pinch-orifice chamber	72
4-5	Radial pressure profiles 2-in. downstream of anode of pinch-orifice chamber.	73
4-6	Characteristic times for current pulse and mass flow.	78
5-1	Capacitor line current pulse capability	83
5-2	17.5 kA current pulse on two different time scales.	84
5-3	Shock tube x-t diagram.	89
5-4	Schematic diagram of "continuum" shock tube mass injection system.	93
5-5	Piezo pressure sensor with plexiglas shock tube end cap	97
5-6	Piezoelectric pressure records at end of shock tube	98
5-7	Shock tube x-t diagram for $P_1 \rightarrow 0$	100
5-8	Effects of driven and driver section lengths on pressure history at end of shock tube; $P_1 \approx 10^{-4}$ torr, 2 msec/div	103
5-9	Effect of driver section diameter on pressure history at end of shock tube; $L_1 = 2.5$ ft, $L_4 = 0.5$ ft, $P_1 \approx 10^{-4}$ torr.	104
5-10	Effect of various diaphragm plunger discs on pressure history at end of shock tube; $L_1 = 2.5$ ft, $L_4 = 0.5$ ft, 500 μ sec/div	106
5-11	Schematic of final mass injection system.	107
5-12	Calculated mass flow for shock tube injection	109
5-13	Cross section of accelerator.	111
5-14	Photographs of shock tube-cathode interface components.	113
5-15	Photograph of mass injection system and gas-triggered switch at back of facility.	117
5-16	Current pulse synchronized to injected mass pulse	118

LIST OF ILLUSTRATIONS-contd.

Figure		Page
6-1	Operating conditions for terminal voltage measurements	122
6-2	Accelerator electrical schematic.	123
6-3	Typical accelerator voltage-current history	125
6-4	Summary of voltage measurements	127
6-5	Voltage current characteristics	129
6-6	Voltage component variation with mass flow rate	136
6-7	Voltage signature for zero injected mass flow; $P_{amb} = 10^{-1}$ torr, $J = 17.5$ kA	138
6-8	Derived resistive voltage components.	142
6-9	Approximate mass flow rate for onset of mass ingestion	143
6-10	Approximate electromagnetic efficiency before mass ingestion	149
7-1	Kerr-cell photographs of discharge luminosity tran- sition to steady phase; $J = 17.5$ kA, $\dot{m} = 5.9$ g/sec.	152
7-2	Stabilized exhaust luminosity patterns for various mass flow rates; $J = 17.5$ kA, $t = 80$ μ sec	155
7-3	Typical magnetic field histories in accelerator discharge; $J = 17.5$ kA, $\dot{m} = 5.9$ g/sec	160
7-4	Enclosed current contours showing discharge tran- sition to stabilized phase; $J = 17.5$ kA, $\dot{m} = 5.9$ g/sec	161
7-5	Typical uncertainty in stabilized current contours; $J = 4.4$ kA, $\dot{m} = 36.0$ g/sec.	165
7-6	Typical magnetic field histories in accelerator discharge for mass starvation; $J = 17.5$ kA, $\dot{m} = 1.2$ g/sec	167

CHAPTER 1

HISTORICAL BACKGROUND

Early pulsed plasma accelerators were extensively studied, initially as plasma injectors for thermonuclear machines [1] and later as space propulsion units [2,3]. In both applications, a large current was passed through a discharge chamber generating a self-magnetic field sufficiently strong for the resulting $\vec{j} \times \vec{B}$ body force to accelerate the ambient gas to a velocity in excess of 10^4 m/sec. Although various electrode geometries were used, such as parallel rail, parallel circular disc, or coaxial tube configurations, the sequence of electromagnetic interactions was essentially the same. Namely, a capacitive energy source at a high voltage was abruptly switched across the electrodes, which were separated by an insulator wall and an enclosed gas at a pressure of $10^{-2} - 10^1$ torr. The subsequent electrical breakdown of the gas was in the form of an intense sheet of current which represented primarily an inductive load to the power supply. This current sheet was initially located at that portion of the interelectrode gap which offered the minimum load to the power supply for that particular geometry. The force resulting from the interaction of this current sheet with

its trapped self-magnetic field then accelerated the sheet into the remaining undisturbed gas imparting to it some fraction of the sheet velocity.

As part of a broad study of the fundamental processes of plasma propulsion, this laboratory has examined accelerating discharges of this type in a variety of configurations and energy ranges. One early aspect of this program was the study of the structure and dynamics of a propagating current sheet in a linear pinch discharge [4-8]. Although this closed chamber configuration did not simulate a useful thruster per se, its demonstrated reproducibility and accessibility to diagnostic equipment made it valuable in the study of the plasma generation and acceleration phases of pulsed plasma propulsion. In this configuration, the electrodes were parallel circular discs, and the initial breakdown took the form of a thin band of current at the insulator wall. This well-defined zone subsequently imploded radially generating an intense plasma column upon its arrival at the chamber axis.

In addition to the generation and acceleration of the plasma to a high velocity, the processes attending its ejection from the pinch chamber were also studied. When a large orifice was cut into the anode and the entire chamber mounted within a vacuum tank, it was observed that while the main body of the current sheet propagated radially inward unaffected, the anode attachment diffracted out through the orifice and traveled radially outward along the outside face of

that electrode [9]. This diffracted plasma front propagated axially as well with a velocity comparable to the initial radial speed of the sheet. A comparison of the current conduction paths for both closed and open configurations is shown in Fig. 1-1. The large double arrows in this figure represent the direction of the $\vec{j} \times \vec{B}$ force and the consequent direction of sheet propagation.

In the interests of a better simulation of space conditions, the usual gas prefill to a given operating pressure was replaced by a dynamic system wherein a puff of gas was released into the discharge chamber at the time of electrical power application. In this way, the associated vacuum vessel was maintained at a pressure several orders of magnitude lower than the chamber pressure, and the plasma ejection process proceeded in a more realistic environment.

The resulting discharge was considerably more diffuse outside the pinch chamber and propagated further out into the low pressure environment for the same current pulse. Since this current pattern continued to propagate for the lifetime of the pulse, it may be reasonably asked whether protracted pulse times would result in continued propagation or whether this current pattern extension would eventually cease. In order to answer this question, the power supply was altered from one which initially consisted of many capacitors connected in parallel around the discharge apparatus to one in which several series-parallel combinations of capacitors were

utilized. By systematically varying the inductance between adjacent series units, a variety of protracted current waveforms was available [10,11].

When this alteration was made, it was found that for sufficiently long current pulses, the previously described process of discrete current sheet propagation was followed by a transition to a steady, more diffuse current conduction pattern [12]. This steady phase, which typically was achieved some tens of microseconds after breakdown, displayed essentially unchanged terminal voltage and current characteristics while continuing to provide a stream of accelerated gas over the entire pulse duration. Such a spontaneous transition strongly suggested that the pulsed plasma acceleration process was simply an initiation phase or "switching transient" on the steady flow acceleration pattern eventually established in the same geometry, and that much of the microscopic scale acceleration and current conduction mechanisms were common to both phases.

Detailed maps of the current distribution throughout the discharge chamber and exhaust plume during this stabilized phase closely resembled those believed to exist in the magnetoplasmadynamic (MPD) arcjet. This latter device is a coaxial steady state accelerator which has recently displayed a high potential for space application as a primary propulsion unit [13-17]. However, despite this promise, the MPD arcjet is not well understood at the present time due to

complexities of reasonable analytical models and to a lack of diagnostic information on the discharge structure—an environment sufficiently hostile to preclude most standard steady-state probing techniques.

The possibility therefore exists that a pulsed plasma accelerator with appropriate mass flow rate and electrical power inputs can be operated on a time scale sufficiently long for the pulsed discharge to stabilize and achieve the essential characteristics of the steady state MPD arcjet over a broad range of input power level. Then, because of the overall transient nature of the quasi-steady discharge and the resulting negligible probe heating, it would be possible to perform self-integrating diagnostic measurements on the exhaust plume and interelectrode region of the simulated thruster and relate these results to the steady state operation.

An additional motivation to a pulsed MPD experiment of this type follows from estimates of projected power consumption of electric thrusters for future space applications. For manned missions to the near planets, the optimum electric power level is in the range from 1 to 10 MW [18-20], i.e., currents from 10^4 to 10^5 A, an operational regime well beyond that available to steady state experimentation. In steady operation, the maximum power is limited to several hundred kilowatts, i.e., currents up to about 4,000 A, by power supply, gas handling, and heat transfer considerations.

It is conceivable that the electromagnetic processes which prevail in MPD thrusters in the multimegawatt power range could be considerably different from those observed in the lower power devices, and accordingly they should be examined. Since quasi-steady operation is possible with power levels up to 100 MW or more, it would be possible to determine the details of the gas acceleration processes, current conduction patterns, and electrode loss mechanisms for accelerators approximating the desired high power devices as well as those common to low power steady state operation.

Yet another motivation for developing a quasi-steady plasma accelerator is that the "long pulse" mode of operation—one in which steady acceleration processes prevail over the bulk of the pulse time—may itself be an attractive space thrusting technique. Whereas purely pulsed plasma thrusters appear to have an efficiency ceiling near 50 percent [21] (directed kinetic energy compared to total input energy), there are some indications that the corresponding efficiency for quasi-steady propulsion may be considerably higher. First, the observed trend in MPD arcs is toward greater efficiencies as the input power is increased. Although these data have been limited to the narrow range of power levels accessible to steady state experiments, say 10 to 300 kW, the trend may be expected to continue to greater power levels to the extent that it is based on the division of electrical input power to the working fluid. This power must be divided between

that necessary to ionize the incoming propellant, that which goes into other internal modes, and that which goes directly into organized streaming energy. From these, useful thrust power is only obtained from the latter category plus that part of the internal energy which can be converted into directed kinetic energy by expansion in a real or magnetic nozzle (in all probability just the random thermal component). If the mass flow is fixed, then as soon as the propellant is completely ionized, additional input power must go into either of the other two modes. In the limit of very high input power, the ionization power becomes negligible and all the power is divided between internal and streaming energies. If the trend observed in the division of these two energies in the steady experiments for currents up to 4,000 A is sustained for currents up to 100,000 A, the resulting overall efficiency can be very high.

Although space power supplies producing tens of kilowatts of usable power appear to be the only available systems in the near future, access to this high power, high efficiency regime is still possible by utilizing quasi-steady pulsing. With the necessary energy storage link between the steady electric power source and the thruster, the advantages of intermittent high power thrusting can be combined with a modest average power consumption by simply controlling the duty cycle.

The following chapters will first describe the genesis

of quasi-steady acceleration from both steady state MPD arcs and early pulsed plasma accelerators by presenting the operational characteristics and particular complexities of each class of thruster. In this way, the relevance of later data to the propulsion problems previously outlined will be more apparent. Subsequent chapters will present design considerations and their proper implementation leading to a quasi-steady accelerator capable of operation over a large range of mass flow rate and power.

CHAPTER 2

THE MAGNETOPLASMA DYNAMIC ARCJET

I. INTRODUCTION

In the past several years, consideration of increasingly ambitious space missions requiring progressively higher specific impulse propulsion systems has fostered the development of a variety of electric propulsion concepts. Initially, emphasis was primarily on the attainment of high propellant exhaust speeds at high electrical conversion efficiencies, with little concern about the low thrust densities characteristic of devices of this family. However, optimum prime propulsion units for deep space missions must combine high specific impulse with reasonably high thrust densities as well. The magnetoplasmadynamic arcjet is the first electric thruster to show promise of this desirable combination.

The potential capability of this new thruster is perhaps best illustrated by casting it on a diagram displaying the specific impulse and thrust density (i.e., thrust per unit exhaust area) attainable with various familiar propulsion devices (Fig. 2-1). In the upper left corner are found the conventional chemical rockets of high thrust but low specific impulse; in the lower right corner reside the electrostatic ion engines and the less well developed pulsed plasma thrusters

JP 25 R 4191 A 66

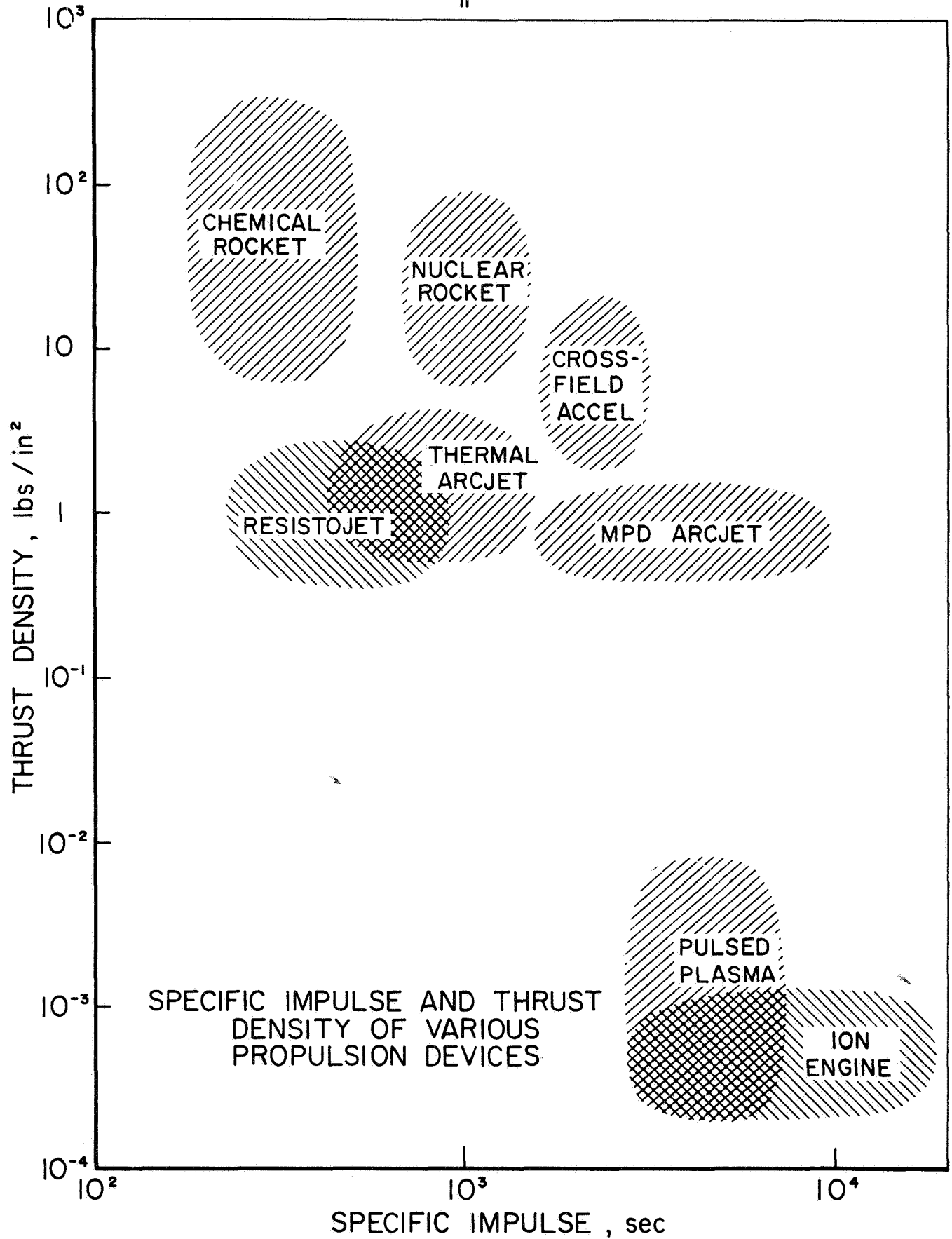


FIGURE 2-1

which provide very high specific impulse, but low mean thrust density. Our interest here is in the accessibility of the upper right domain where both specific impulse and thrust may be optimized for given missions.

The solid-core nuclear thermal rocket takes a step in this direction in providing specific impulses up to 800 sec at thrust densities comparable with chemical rockets. Projections for proposed liquid- and gas-core nuclear rockets extrapolate further into the desired domain. Operational electrothermal systems, such as the arcjet and resistojet provide specific impulses comparable with the nuclear rockets, at one or two orders of magnitude less thrust density.

The desired domain of high specific impulse and substantial thrust density was first attained in the laboratory by a class of steady-flow electromagnetic plasma thrusters wherein an externally applied magnetic field acted upon currents driven through an ionized propellant stream to provide the desired acceleration. Data from laboratory tests of these devices included thrust densities of 10 lb/in^2 at specific impulses from 2,000 to 3,000 sec [22], but was attended with such severe material erosion problems, and involved such massive auxiliary equipment for cooling, magnetic field generation, and preionization of the gas flow, that little space propulsion application could be visualized.

Prior to 1964, no feasible candidate for a space thruster capable of operation in the desired range of Fig. 2-1

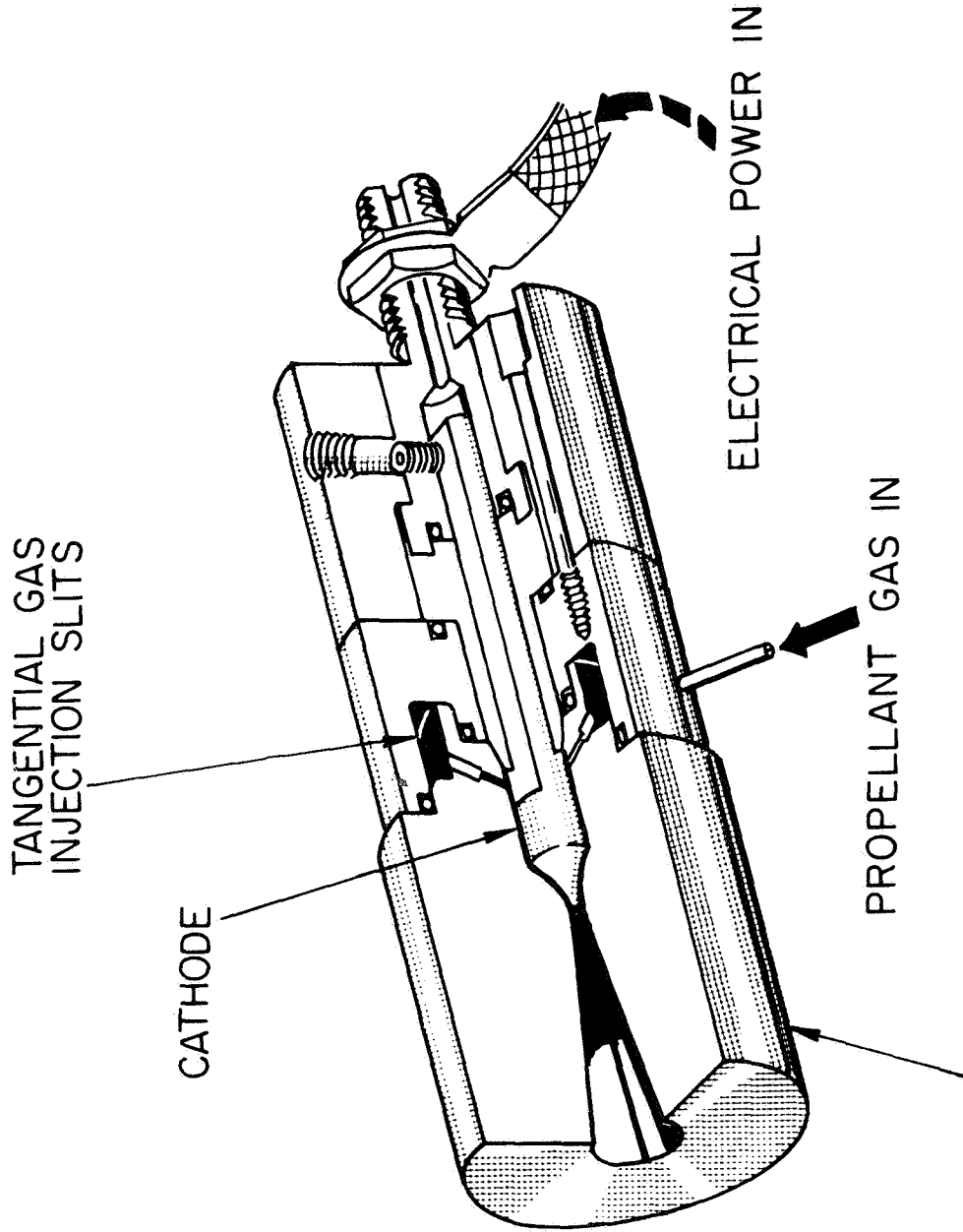
existed. At this time, however, experimentalists stumbled upon a thruster concept which combined certain elements of both the electrothermal and electromagnetic thrust mechanisms, to produce better performance than either mechanism alone. The capability of this thruster, which has generally become designated as the magnetoplasmadynamic or MPD arcjet, has yet to be precisely catalogued. However, recent experiments indicate its operating regime to be approximately that shown in Fig. 2-1, i.e. specific impulse comparable to that of the ion engine but thrust density values at least three orders of magnitude greater. It will be subsequently shown that this performance improvement is accompanied by unique problems which have lead to substantial data discrepancies, to an absence of definitive diagnostic experiments, and to a consequent lack of analytical formulation. Nevertheless, the magnitude of the initial performance increase of the MPD arcjet over other electric propulsion schemes is sufficient to warrant a continuing effort in order to resolve these problems.

This chapter is not meant to be a complete review or catalogue of MPD arc operating characteristics since these exist in the literature [23-25]; instead, its intent is to provide a familiarity with the chronological development, operational idiosyncrasies, and postulated thrust mechanisms and analytical models of the MPD arcjet. Within this framework, later chapters describing the results of

the present pulsed experiments can be appropriately related to the associated steady state phenomena.

II. EARLY OBSERVATIONS

The MPD arcjet was a by-product of experimental efforts to extend the operating regime of the conventional thermal arcjet, a device that itself was being developed to exceed the specific impulse level of chemical rockets by circumventing the limitation imposed by the energy content of the combustible propellants. Typical of the variety of thermal arcjets is the radiation-cooled thruster shown in Fig. 2-2 [26]. In this engine, an arc is struck between the central cathode and the diverging anode nozzle, and is constrained to pass through the short constrictor channel. The tangentially injected propellant is heated by both the arc and the thruster walls and in turn stabilizes the arc filament while maintaining the thruster walls at a tolerable temperature. The specific impulse for this 30-kW engine ranges from 1,000 to 1,500 sec for hydrogen propellant with an overall energy conversion efficiency of up to 45 percent. The upper value on specific impulse attainable in this device and in others like it is established by the thermal limitations of the tungsten electrodes, and of the other material surfaces. Yet, there is considerable motivation to operate thrusters of this class at substantially greater power density, since any additional energy input beyond that



ANODE NOZZLE

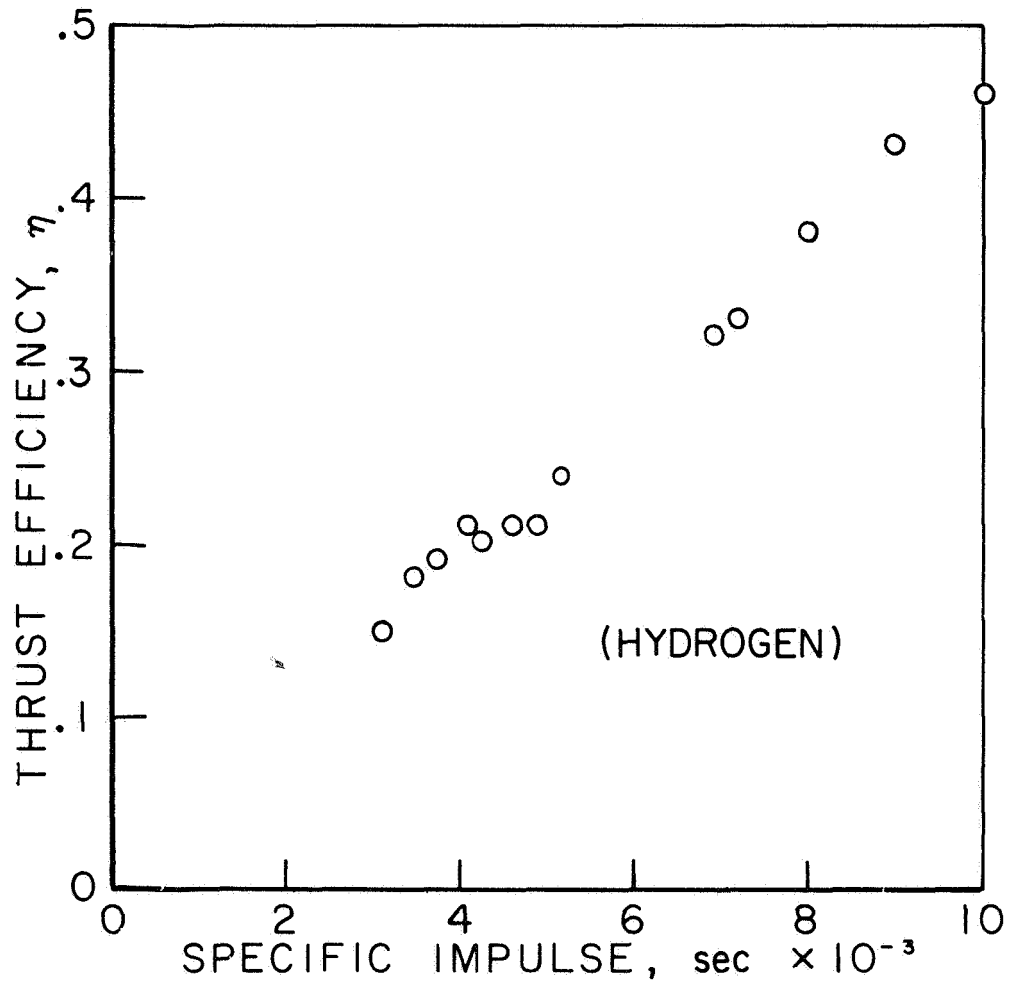
30 kW RADIATION-COOLED ARCJET ENGINE (REF. 26)

FIGURE 2-2

required to ionize and dissociate the propellant will go directly into random thermal modes, most of which can be converted to kinetic energy in the nozzle. However, attempts to operate in these higher power regimes were accompanied by frequent burnouts at the anode attachment of the arc filament, and the arcjet concept seemed fundamentally confined to specific impulses below 2,000 sec.

Then, in late 1963, Ducati reported a remarkable change in the operating range of a hydrogen arcjet [13]. Namely, that by drastically reducing the mass flow and hence the chamber pressure, the arc could be caused to diffuse over the cathode surface, and to extend far out into the exhaust stream, in which configuration the arc current could be increased from about 300 A to 3,000 A or more with no noticeable structural damage. Operating under these conditions, a luminous exhaust plume was observed to blossom out into a large ball behind the nozzle, and the thruster performance could be increased to the level shown in Fig. 2-3, attaining efficiencies of nearly 50 percent at a specific impulse of 10,000 sec.

In order for a purely thermal expansion to produce velocities of such magnitude, stagnation temperatures of the order of $100,000^{\circ}\text{K}$ would be required. Since this seems substantially beyond the thermal limitations of the thruster, it may be surmised that the large arc current generates a magnetic field of sufficient intensity to react on the



MAGNETOPLASMA DYNAMIC
THRUSTER EFFICIENCY VARIATION
WITH SPECIFIC IMPULSE
(REF 13)

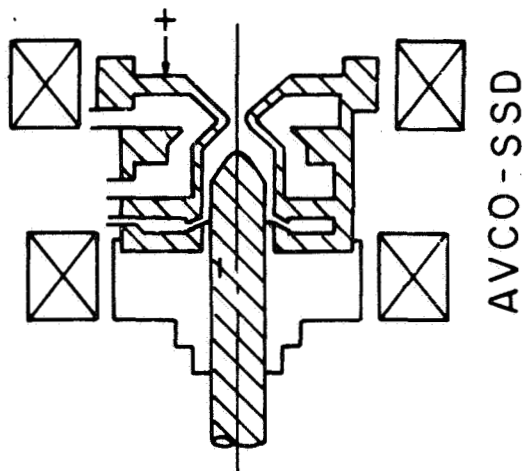
AP25-R4130A 66

FIGURE 2-3

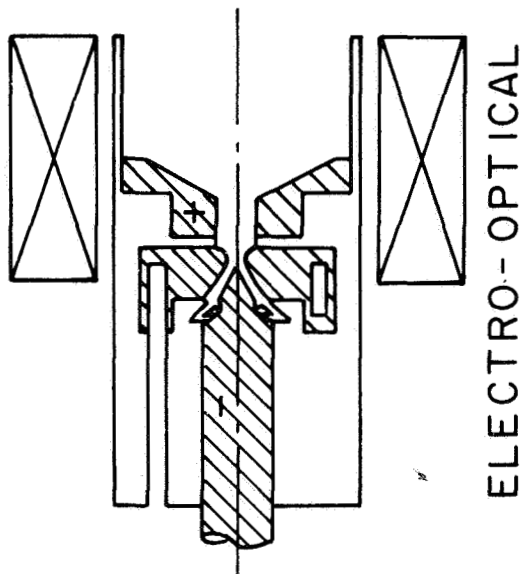
current pattern itself, and thus to produce a substantial electromagnetic thrust component. Hence, contrary to the discouraging predictions of the early plasma propulsion experiments, Ducati had constructed a steady electromagnetic accelerator which required no external magnet, no preionization equipment, and no gas-seeding system, and which operated with negligible electrode erosion.

Immediately following Ducati's report, several other laboratories undertook a sequence of rather empirical confirmatory experiments in which thruster geometry, propellant type, mass flow rate, and power level were varied [14-17]. External magnetic fields were also added to diffuse further the anode arc attachment, resulting in significant increases in thruster lifetime. In retrospect, some hints of the high performance capability could be identified from much earlier experiments on steady electromagnetic thrusters of the "Hall-current" class [27,28]. Typical of the many configurations which were found capable of operating in this high specific impulse domain are the five thrusters shown schematically in Fig. 2-4. In contrast to the design shown in Fig. 2-2, these geometries cover a wide range in both degree of throat constriction and magnitude and configuration of the externally applied magnetic field. However, since each of these thrusters is capable of a performance level at least equal to that of Ducati's, each should logically be regarded as a type of MPD arcjet.

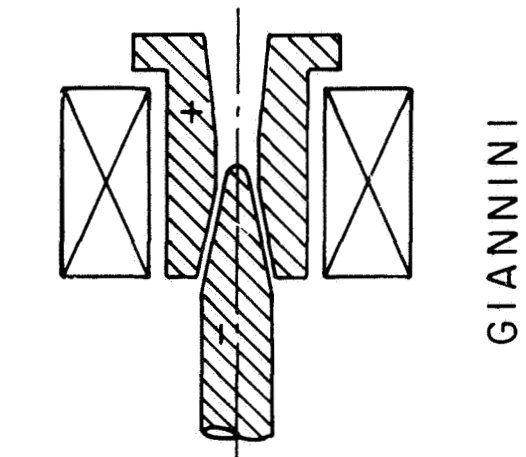
JP25-R4190 A 66



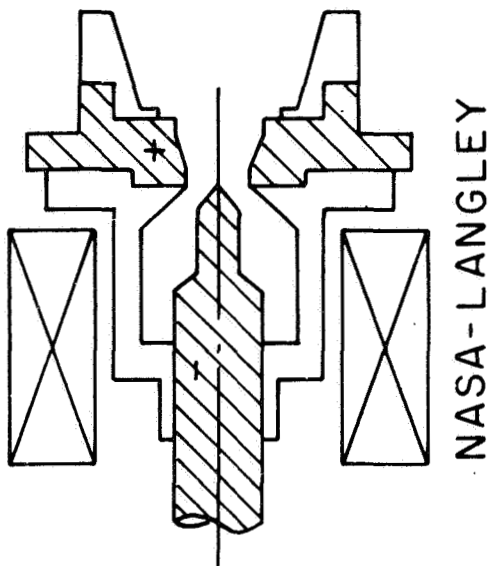
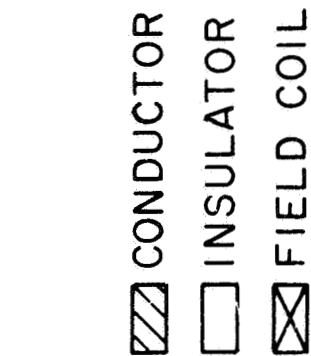
AVCO-SSD



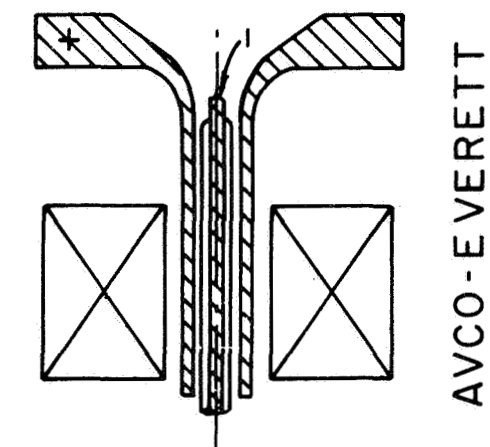
ELECTRO-OPTICAL



GIANNINI



NASA-LANGLEY



AVCO-EVERETT

VARIOUS MPD THRUSTER CONFIGURATIONS

FIGURE 2-4

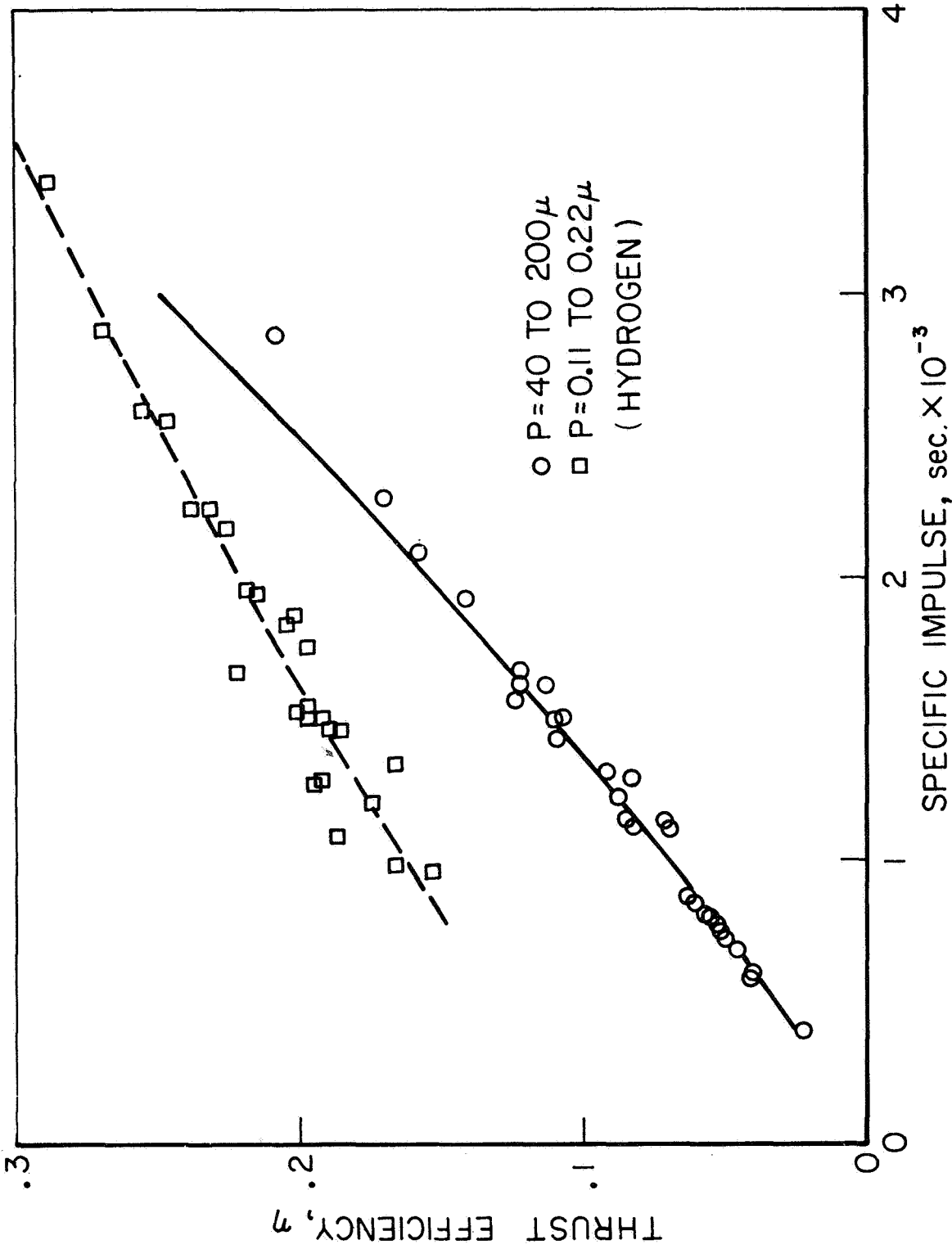
In the process of cataloging the performance of these various thrusters, it soon became apparent that a considerable problem existed in determining the influence of the testing environment, i.e., vacuum tank size, material, and back pressure level. In some cases it was observed that current loops in the exhaust plume were completed through the metallic vacuum tank walls [29,30]. In others, the ambient pressure level was high enough to provide a significant fraction of the total accelerated mass flow by ingestion and acceleration of the residual exhaust gases back through the arc exhaust plume. In fact, arcs have been observed to continue to produce significant thrust and an extended, luminous plume with zero externally injected propellant [31, 32]. Subsequent tests showed that for very low mass flow rates and cathode diameters less than 1/4 in., the arc discharge was principally sustained by vaporization of electrode material [33]. For larger diameter cathodes, however, negligible erosion was found, and stable operation with no incoming gas flow could be maintained indefinitely, presumably by recirculation of the background gas [32].

In order to minimize the effects of ingestive recirculation of the exhaust gases and current loops in the environmental chamber, several MPD thrusters have been operated in the large vacuum facility at the National Aeronautics and Space Administration's Lewis Research Laboratory [34,35]. Specifically, this vacuum tank is 15 ft in diameter by 65 ft

long and is equipped with a liquid nitrogen-cooled wall and twenty 32-in. diffusion pumps making it one of the few vessels of its size capable of maintaining a vacuum of 10^{-5} torr at characteristic steady state MPD arcjet flow rates.

Typical of the results of these tests is the efficiency-specific impulse data shown in Fig. 2-5. The thruster used for this test was an Avco-SSD model identical to the configuration shown in Fig. 2-4, and the propellant was hydrogen. The solid line in the figure represents the average of performance data recorded in a vacuum tank 3 ft in diameter at a back pressure of 0.2 torr. The small circles are performance data recorded in the large facility at approximately the same back pressure as in the smaller tank indicating that at this pressure, the smaller tank does not appear to prejudice the data. As the ambient pressure is lowered by three orders of magnitude, it is observed that the thrust monotonically increases, and consequently the thruster performance increases as shown by the square data points and the dashed average line through them. However, even in this case, the author expresses concern that entrainment effects may still be significant due to the large plume growth as the back pressure was lowered. Nevertheless, within the geometrical and environmental capabilities of this large vacuum facility, the original high performance of the MPD arcjet with a low propellant flow rate has been sustained.

AP25-R4124 A 66



MPD ARCJET PERFORMANCE WITH VARIOUS TANK PRESSURES
(REF 34)

FIGURE 2-5

III. MECHANISMS

From the operation of these different thruster configurations over a wide range of conditions, it is apparent that a variety of mechanisms contribute to the total thrust: (1) a self-field contribution arises from the interaction of the current with its self-induced magnetic field. The resulting thrust component clearly varies with the square of the arc current and becomes significant for currents greater than approximately 1,000 A. This contribution can be further subdivided into an axial component and a radially inward component, the latter being counterbalanced by a radial pressure gradient which, when integrated over the cathode face, also produces an axial force. (2) The arc current interacts with the external magnetic field to produce (a) an azimuthal current which can further interact with the applied magnetic field to yield axial forces and (b) a bulk azimuthal motion of the plasma in which the rotational kinetic energy can be exchanged for axial kinetic energy by expansion in a nozzle. (3) Some electrothermal thrust contribution must remain as a vestige of the original function of the arcjet accelerator.

Beyond the initial identification of these mechanisms, and the general observation that their relative importance is a sensitive function of the particular operating conditions and electrode geometry, little specific correlation of performance with physical phenomenology has been achieved.

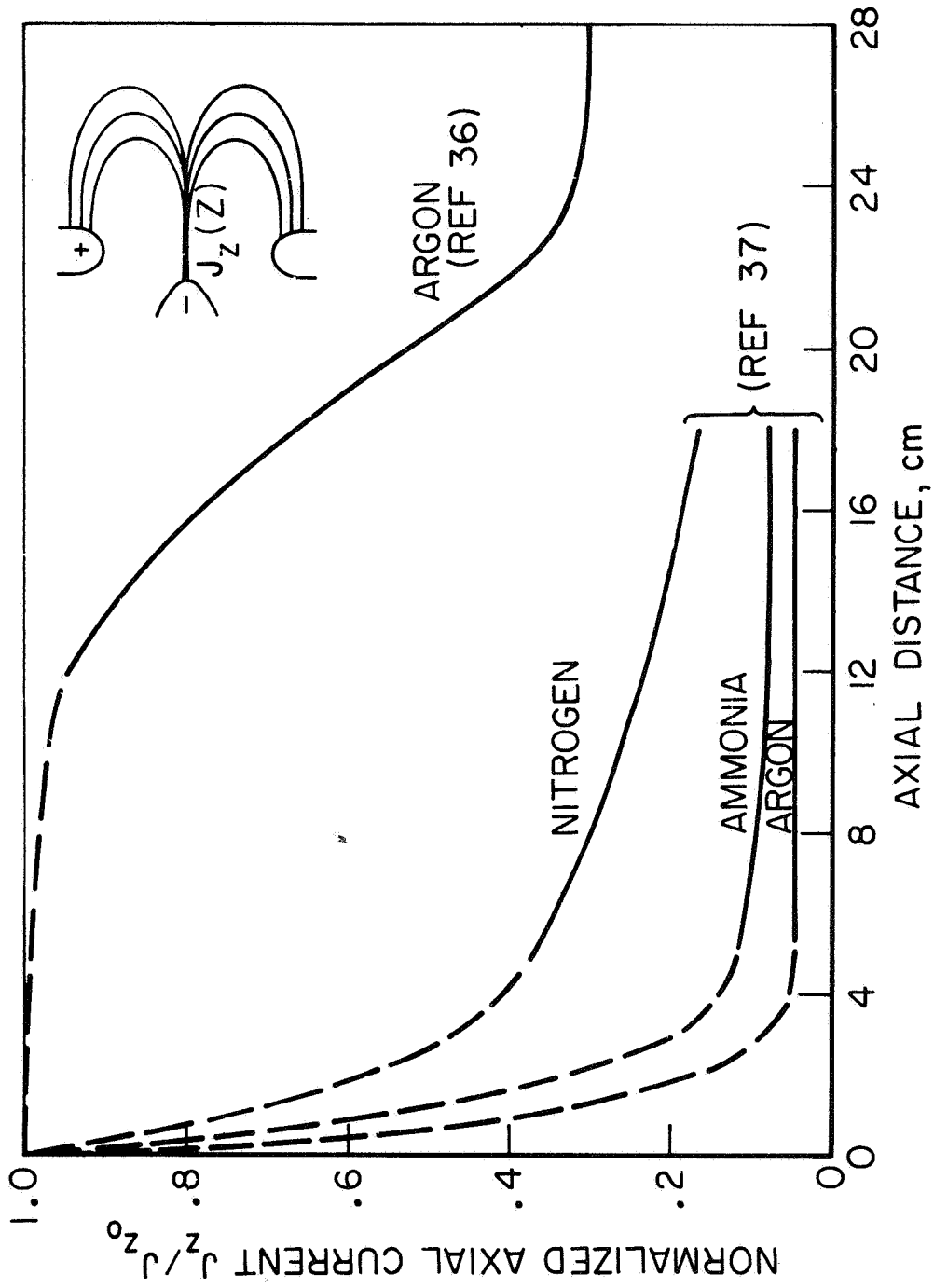
Clearly needed is a thorough examination of the plasma flow both within the interelectrode gap and in the exhaust plume over the entire operational regime. However, routine techniques for probing the exhausts of more conventional high performance thrusters are not applicable to the MPD arcjet due to the high power density in the arc discharge. Instead, a limited degree of success has been experienced with spectroscopic techniques, probes swung through the exhaust, and large vigorously water-cooled probes. Even using these techniques, data acquisition is limited to the low power regime with virtually no possibility of probing the interior of the arc chamber due to the small interelectrode spacing.

Even that data which can be acquired by operating the arcs at a sufficiently low power level to permit limited diagnostic measurements are found to differ considerably from one laboratory to another. The determination of the current density distribution in the exhaust plume offers an interesting example of this problem. This measurement is of fundamental value in ascertaining the fraction of the total current which is flowing in the exhaust plume, the distribution of current over the electrodes, and the resulting contribution of the plume to the total thrust. Consequently, the details of the current density distribution and its variation with mass flow rate, total current, back pressure, and geometry have been one of the primary objectives of steady state experimental programs. Two separate determinations

of this distribution in the exhaust plume have been made for approximately similar operating conditions. The first of these employed a water-cooled Hall effect transducer on an argon MPD arc operating at a total current of 400 A, an external magnetic field of 1.5 kG, and a back pressure of the order of 0.1 torr [36]. The second effort employed a similar technique on an MPD arc using argon, ammonia, and nitrogen with roughly the same external field and back pressure, but a total current of 1,000 A [37]. The results agree qualitatively on the radial dependence of axial current density which is strongly peaked in the center near the exit plane and broadens smoothly as axial distance from the exit plane increases. The disagreement arises in connection with the axial decay of axial current as shown in Fig. 2-6. Here, it is seen that the higher current data decays axially faster than the lower current data, a trend which conflicts with the observation of higher currents producing a greater plume extension, assuming that the highly luminous regions can be associated with regions of high-current density. Thus, even for this important parameter, there is considerable disagreement regarding both qualitative and quantitative characteristics of arc operation.

As yet another complication, recent results have shown that for most thrusters utilizing an external magnetic field, the arc discharge assumes the form of a spoke rapidly rotating in the azimuthal direction [35,38,39] instead of the axisym-

AP15-RA126 A 66



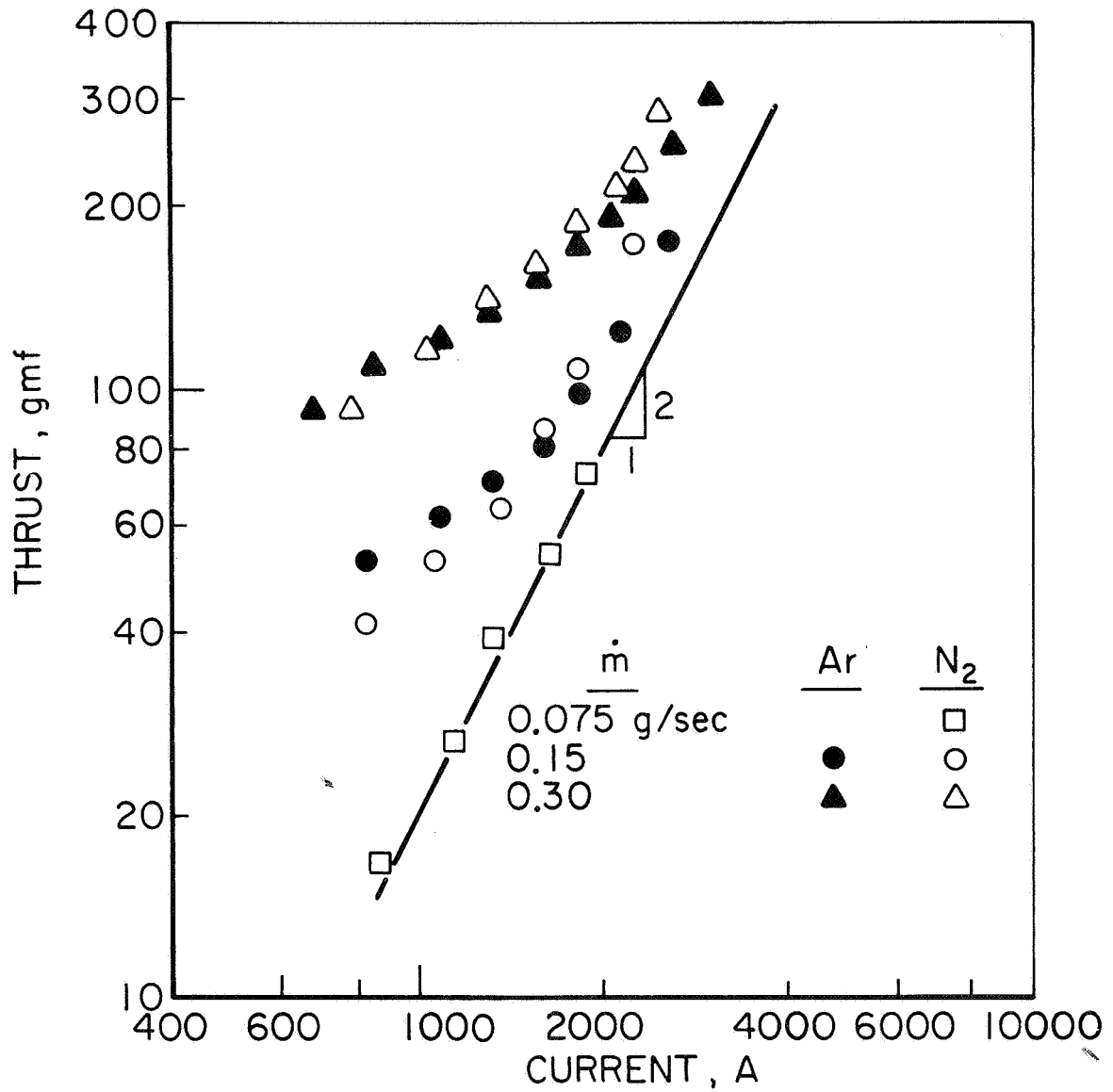
EXPERIMENTAL AXIAL CURRENT VARIATION WITH AXIAL DISTANCE

FIGURE 2-6

metric diffuse discharge observed in the self-field configurations [39,40]. In addition to the obvious implications for thruster performance, this predicates additional complexities in experimental techniques and analytical formulations, both of which up to this time had assumed axisymmetric flow conditions.

A few illuminating tests, however, have produced significant information and insight into the operating characteristics of the MPD arc. One of these has been the study of the electron number density and electron temperature distribution in an exhaust plume by the use of microwave and Langmuir probes swung through the plume and spectroscopic techniques [41]. From these data, it was concluded that the plasma was in a highly nonequilibrium state. However, the data was taken at only one test condition (input power up to 50 kW, no external magnetic field, and back pressure from 0.1 to 0.5 torr), and its extension to higher power operation can only be assumed.

Another significant result has been the positive identification of the self-field thrust mechanism by Hügel [42]. Figure 2-7 shows a log-log plot of thrust as a function of total current for argon and nitrogen at various propellant flow rates. It is seen that as the current is increased, the measured thrust eventually follows a line of slope 2 reflecting the interaction of the current with its own magnetic field. This latter region is also



MEASURED THRUST AS A FUNCTION OF ARC CURRENT
FOR ARGON AND NITROGEN (REF. 42)

categorized by an increasing overall efficiency of the thruster. It is further observed that at higher mass flow rates, the transition to current-squared thrust dependence occurs at larger currents due to the increased influence of the aerodynamic thrust components. This latter effect illustrates one of the principle problems in systematic examination of MPD performance. That is, although the arc shows a trend towards improved performance and greater efficiency as the current is increased, this effect can only be observed for currents from about 1,500 to 3,000 A—the lower boundary being that where the self-field mechanism becomes dominant, and the upper limit being imposed by the power supply itself. This limited range has proven to be inadequate for any parametric study to reveal significant trends leading toward an optimum configuration. More troublesome is the fact that although all indications point toward further performance gains for currents well above 3,000 A where magnetoplasma-dynamic effects will dominate other thrust contributions, this is precisely the regime that is inaccessible to steady state testing.

IV. MODELS

Several physical models have been proposed for the MPD arcjet, but because of the paucity of diagnostic experiments, these models invoke a variety of assumptions with a consequent wide range of predictions and limitations. Selection of the most pertinent model awaits better determination

of the physical parameters of interest in the exhaust plume. Rather than describe each candidate model in detail, only the salient features or parametric implications of each will be discussed. A more complete review of these models is available in Ref. [43] wherein their mathematical background and particular subtleties are developed.

The main distinction among the models is between the continuum or magnetogasdynamic point of view and the free particle or gaskinetic approach. In the continuum representation, the crossing of the radial and axial current components with the azimuthal self-magnetic field produces axial forces as discussed previously. In addition, either the radial or axial component of an external magnetic field when crossed with the proper current component can produce an electromagnetic swirling of the gas. Finally, allowing tensor conductivity effects, various Hall interactions can be present, such as the crossing of an azimuthal Hall current component with the radial component of an external field to produce an axial force.

For the purely self-field contributions, it has been shown that the total electromagnetic thrust for uniform current density over the cathode end surface varies as

$$T = \frac{\mu J^2}{4\pi} \left(\frac{3}{4} + \ln \frac{r_a}{r_c} \right) \quad (2-1)$$

where T = total electromagnetic thrust (N)

J = total arc current (A)

μ = magnetic susceptibility (mks)

r_a, r_c = radii of arc attachment on anode and cathode
respectively [43]

Note that this thrust component is independent of the detailed pattern of the arc, and independent of the mass flow rate to the extent that the mass flow does not alter the total arc current or the effective radii of arc attachment on the cathode and anode surfaces. To this extent, then, the exhaust velocity should scale inversely with the mass flow rate if the acceleration conforms with the postulated mechanism.

Although the magnetogasdynamic model of the MPD arc makes no reference to gas properties, it assumes a continuum interaction in the manner in which it invokes the $\vec{j} \times \vec{B}$ body force. However, since the large arc currents and high exhaust velocities are favored by low gas pressures in the arc chamber, some particle mean free paths and gyro radii may become comparable with the chamber dimensions. The extreme case of completely collisionless current conduction and particle acceleration forms the basis for the second proposed model for the MPD arc [44]. In this model, sufficient collisions are allowed to ionize the incoming propellant near the anode. The ions thus created are accelerated radially inward by the electric field without further collisions and are subsequently deflected axially outward by the azimuthal self-magnetic field until they join an axial stream of electrons emitted from the

cathode. Hence, the thruster basically acts as an electrostatic ion accelerator with space-charge neutralization provided by the cathode electron beam.

This postulated behavior predicts certain correlations of its terminal properties which differ from the continuum case. Implications of the model are that the mass flow rate is now directly coupled to the current through the ion radial conduction, and that the ion gyro radius must be the order of its radial position in order to negotiate the turn from the radial to the axial direction. Taking these into account predicts an arc voltage and thrust that each vary with the square of the current, and an exhaust speed proportional to the current and inversely proportional to the ion mass.

The validity of the particle model clearly hinges on the collisionless assumption, one which may be unreasonable for much of the domain over which the MPD arc is observed to function. However, two features of it are more generally relevant and provide some insight into two prominent aspects of the arc operation. The first relates to the ability of the cathode to withstand the extremely high-current densities, of the order of 10^9 A/m². Normally, concentrations of current this intense will rapidly erode a cathode surface by ion bombardment, but here the strong magnetic field near the cathode tip can deflect the incoming ions sufficiently to protect the cathode from excessive heating. Because of the inverse de-

pendence of the magnetic field on the radius, this magnetic protection of the cathode can prevail at far higher particle densities than could be allowed for application of a purely collisionless theory throughout the arc chamber.

The second instructive contribution of the collisionless approach concerns the coupling of arc current to mass flow rate which may be relevant to the "zero mass flow" operation discussed earlier. If the device is operated in a regime where ions alone carry the current and the mass flow is then reduced, the arc would be starved for current carriers, and the current would tend to decrease. However, if the current were forcibly maintained at its previous level by the external circuit, the arc would be obliged to obtain current-carrying particles from other than the inlet mass flow, e.g., from the electrode surface material, or by recirculating a fraction of the exhaust plume. Thus, while this model may not describe the higher mass flow domain of MPD arc operation, it may establish the lower mass flow limit before recirculation or electrode consumption begins.

The gap between the continuum and collisionless approaches can be bridged by incorporating collisional effects in the particle orbit mechanics, a formidable task if done precisely. However, qualitative patterns of current and thrust densities can be predicted from examination of the electron and ion Hall parameters and their respective gyro radii over the arc chamber and plume regions [45]. This

approach requires some initial estimates, presumably based on experimental data, of the patterns of the various gas properties which determine the Hall parameters and gyro radii, namely the degree of ionization, the electron number density, the electron and heavy particle temperatures, and the magnetic field.

When this procedure is applied to a typical MPD arc geometry, it is found that most of the phenomenological traits characteristic of the experimental operation can be qualitatively displayed. Plume protraction, ambient gas ingestion, arc swirling, cathode protection, and the gross aspects of the current density distribution all follow logically from its self-consistent application under the prevailing conditions. The extent to which it can provide quantitative information of these phenomena clearly rests on the accuracy with which the appropriate parameters can be determined over the range of interest.

A model which attempts to take entrainment effects into consideration has been postulated by Cann [46] for a predominantly ion current and later by Bennett [47] for either electron or ion current conduction processes. In this "critical mass flow" model, it is assumed that the arc will operate at that mass flow rate for which the total voltage is a minimum, and consequently, a distinction is made between the mass flow which is externally provided and the total mass flow accelerated through the arc dis-

charge. In cases of entrainment or electrode erosion, the latter can be greater than the former; the reverse situation can exist if only some fraction of the injected mass is ionized and accelerated in the discharge. When these assumptions are incorporated into an energy balance, the voltage is minimized at that mass flow rate for which 50 percent of the energy is in directed streaming energy and 50 percent in ionization energy (assuming a monatomic gas with negligible electrode loss and thermal contribution). Only by operating at mass flows less than the critical value without entrainment or erosion is it possible to have an efficiency greater than 50 percent. At this critical mass flow rate, the ion exhaust velocity is shown to be that value for which the ion kinetic energy equals the ionization energy of the neutral species, i.e.,

$$U_{\text{crit}} = \left(\frac{2e \mathcal{E}_i}{M_i} \right)^{1/2} \quad (2-2)$$

where U_{crit} = critical ion velocity (m/sec)
 e = electronic charge (coul)
 \mathcal{E}_i = ionization energy of a neutral (eV)
 M_i = mass of the ion (kg)

In addition, for an external field accelerator, the minimum or critical voltage is shown to be proportional to the product of this "critical velocity" and the external field strength. In retrospect, the formulation of a critical velocity and its function as the constant of proportionality

between voltage and magnetic field can be shown from a one-dimensional channel analysis. The straightforward application of momentum and energy integral relations across an acceleration zone generated by an external magnetic field, and the assumptions of negligible inlet conditions and negligible thermal energy, lead to identical relations and implications.

Experimentally, there is some evidence of operation in accord with parts of this model. The linear relation between voltage and applied magnetic field is common among thrusters in this category and, in fact, the critical velocity concept in the MPD field was first invoked to explain this behavior [17]. More recently the identification of a high velocity ionized species and a low velocity neutral species in the same exhaust plume [48] reflects on one of the initial assumptions of this model.

The concept of a critical velocity in plasma accelerators is not new. Early results by Fahleson [49] from closed chamber, rotating plasma experiments displayed a linear relation between total voltage and applied magnetic field, the constant of proportionality being the same critical velocity. Again, this velocity was only observed among the ionized species and was not exceeded until all of the neutrals were ionized.

In both the closed chamber and MPD experiments, the critical velocity concept suffers from a lack of understanding

of the detailed physical processes involved. In particular, the mechanism by which the ionized specie interacts with the neutral gas is still subject to question. Whereas an electron is an effective ionizer of a neutral when its energy equals the ionization energy, an ion must travel with a velocity nearly ten times the critical velocity to be equally efficient. To get energy from the streaming ions into the electrons, Alfven [50] has postulated local charge imbalances which sufficiently accelerate the electrons, while Lin [51] claims elastic collisions between ions and electrons are sufficient. Like the other models, the extent to which this one will be useful to both external and self-field MPD arcs will most probably depend on the quality of diagnostic experiments in the interelectrode region and the examination of terminal property functional dependencies over the entire power spectrum of arc operation.

It is important to realize that none of the previous models includes an electrothermal thrust contribution which, as has been mentioned previously, is a strong possibility considering the evolution of the MPD arc. At first glance, the electrothermal contribution might seem to be minor in a thruster producing exhaust velocities up to 10^5 m/sec because of the excessive gas temperatures which would be required. However, a characteristic feature of the previous models has been the displacement of the collision dominated regime downstream from the material electrodes due to the large self-

induced or external magnetic fields. In this way, the arc may now be able to sustain much higher currents and gas temperatures in this "ohmic" region than if the latter were in direct contact with the electrodes. The extreme point of view would be to regard the device as still an electrothermal arc, with the hottest portion of the gas constrained away from the electrodes and the exhaust stream expanding in a magnetic nozzle established by the field pattern. This postulated electrothermal component is important from the standpoint of the overall efficiency of the arc. Were only electromagnetic effects producing the gas acceleration, all joule heating of the gas would be regarded as an energy loss. If on the other hand, the device retains some of its electrothermal characteristics and can redirect a significant portion of this randomized energy into streaming energy, the overall efficiency will benefit accordingly. In the limit, only some radiation and electrode losses would detract from its performance, and its efficiency can be extremely high.

V. SUMMARY

After several years of intense study in several laboratories, little insight has been gained into the MPD arcjet beyond the verification of the performance level first demonstrated by Ducati. Subsequent estimates of the high potential of MPD thrusters—specific impulses above 3,000 sec with thrust densities at least three orders of magnitude greater

than the ion engine—still appear realistic and pertinent to future space applications. In isolated instances, illuminating experiments have clearly identified particular thrust mechanisms or phenomenological characteristics in a given configuration, but a cohesive model for the thruster operation continues to be elusive. The principle obstacle blocking a systematic solution to the problem is the lack of diagnostic information, this in turn being due to the extreme conditions throughout the entire discharge region and the poorly defined influence of external environmental factors. Parametric investigations, which usually play a key role in the development of new thrusters, have been largely ineffective with the MPD arc due to complex inter-parameter dependencies and limitations of steady state testing facilities. Most troublesome has been the inability to explore the operating regime above 3,000 A where the most efficient acceleration is indicated. The cumulative implication of these steady state results is that the only way in which complete diagnostic information can be gained throughout the entire operational domain is by an intermittent or quasi-steady thrusting technique. Only then will it be possible to ascertain the relative importance of specific geometrical and environmental factors and thus construct an optimum thruster for most efficient MPD propulsion.

CHAPTER 3

PULSED ACCELERATORS

I. INTRODUCTION

In the previous chapter, the migration of steady state plasma accelerators toward a quasi-steady operation was related to the desire to observe arc operation at power levels up to several tens of megawatts and to the need for detailed diagnostic measurements in this range as well as for lower powers. Concurrently, experimental results with pulsed (i.e., completely unsteady) plasma accelerators were suggesting the extension of these pulse lengths to considerably longer times, thus approaching the quasi-steady mode from the opposite end of the time spectrum. Since the design of the quasi-steady accelerator, which is central to this thesis, draws heavily on experience gained with transient discharges, a brief review of this related trend will be profitable.

II. EARLY OBSERVATIONS

Initially, pulsed plasma thrusters were studied because of certain potentially advantageous phenomenological differences from steady state plasma thrusters, associated with the transient nature of the discharge:

1. If the acceleration event is sufficiently rapid, it may be possible to avoid thermalization of the free

electron component with the ion streaming energy and the subsequent loss of this energy by inelastic collisions and radiation.

2. The characteristic time derivatives of the acceleration process produce certain spatial nonuniformities, such as the "skin effect." Briefly, this effect is associated with the tendency of high-frequency currents to flow along the outer surface of a conductor, and is fundamental to the generation of an intense, thin current sheet in a gaseous discharge.

3. Higher instantaneous power operation is possible by utilizing intermittent intense pulses from a capacitive energy storage bank.

It was felt that these potential advantages, if properly harnessed, could manifest themselves in higher overall efficiencies.

In Chap. 1, the pulsed plasma discharge was broadly classified into three principle phases: plasma generation, wherein the application of a high voltage electrical pulse is synchronized with the arrival of a puff of gas into the discharge chamber to produce a gaseous breakdown in the form of a thin, intense current sheet; plasma acceleration, in which the current sheet, driven by its self-magnetic field, sweeps over the injected mass and accelerates it to a high velocity; and plasma ejection, wherein the current sheet and accumulated mass are exhausted into a vacuum, thereby

imparting a thrust increment to the accelerator. Although these phases overlap in any actual thruster, their separation provides a useful conceptual framework to which the experimental results and difficulties will be related.

III. EXPERIMENTAL CHARACTERISTICS

Whereas certain experiments were centered about the development of the complete thruster and the measurement of its performance [3,52,53], others were directed toward a study of the more basic processes contributing to the acceleration [5,7,54,55]. The principle departures from idealized operation, as observed in this latter group of experiments, were associated with the plasma acceleration phase. Since the characteristic impedance of the discharge, about $10^{-2} \Omega$, was considerably lower than the characteristic impedance of early capacitor power supplies, the typical current pulse driven through the discharge was a damped sinusoidal ringdown. In most experiments the first current reversal in this ringdown pattern occurred before the propagating sheet reached the ejection port. Instead of the current in this sheet also reversing and the acceleration process continuing, a second sheet was generated at the initial location of the first. This in effect severed the electromagnetic coupling between the power supply and the first current sheet resulting in a degradation of the latter's velocity by viscous interaction with the chamber walls. Since nearly all of the mass was

accumulated by the first sheet, the overall effect of this current reversal was a performance reduction. Capacitors large enough to extend the half-cycle time beyond the characteristic acceleration time would have been unreasonably large and expensive, and would have predicated rise times too long for effective utilization of the skin effect. Consequently, the experimental tendency was to shorten the length of sheet travel and increase the driving current time by the use of specially tailored current pulses [10,11].

A second problem in the acceleration phase was the nonideal behavior of the current sheet as a mass sweeper. Photographic and diagnostic studies revealed that the sheet in fact tilted during its propagation and lost its effectiveness at the electrodes, predominantly the anode, due to a diffuse attachment [56]. The cumulative effect of these and other imperfections was the reduction of the efficiency of mass accumulation to some fraction of the ideal value.

A third inefficiency in converting electrical energy into directed streaming energy was associated with the inelastic collisions between the ambient neutral particles and the propagating current sheet, the resulting dissipation being termed the dynamic inefficiency. Analysis has shown [21] that for a constant velocity current sheet perfectly sweeping a uniformly distributed mass, only 50 percent of the total energy imparted to the gas goes into streaming energy; the other 50 percent is absorbed in internal modes.

This distribution of useful and dissipative energy can be improved by the selection of a converging geometry and by judicious tailoring of the current pulse and injected mass profile. However, a sharply decreasing density profile in front of the sheet, shown favorable from this analysis, in some cases resulted in an instability which caused the formerly uniform current sheet to degenerate into arc filaments useless for plasma sweeping functions [57].

In the plasma initiation phase, the primary concern is to have the expended energy small compared to that later delivered to the gas during the acceleration phase. However, the energy expended in breaking down a cold gas by applying a high voltage to initially cold electrodes can be substantial. In fact, for the short pulse times typical of these early accelerators, this loss can be the dominant loss of the system. With longer pulse times, the amount of energy expended in the initiation process will not change, but it will be a relatively smaller fraction of the total energy input to the gas over the entire pulse time.

In the plasma ejection phase, it was shown that the accelerated plasma could be exhausted without a significant loss of momentum [9]. This result was of course subject to the qualification discussed earlier--the plasma must not be decoupled from the driving circuit (by current reversal) before the bulk of the ejection process is complete. It was further observed that before current reversal occurred, the current flowed out into the exhaust plume during the ejection

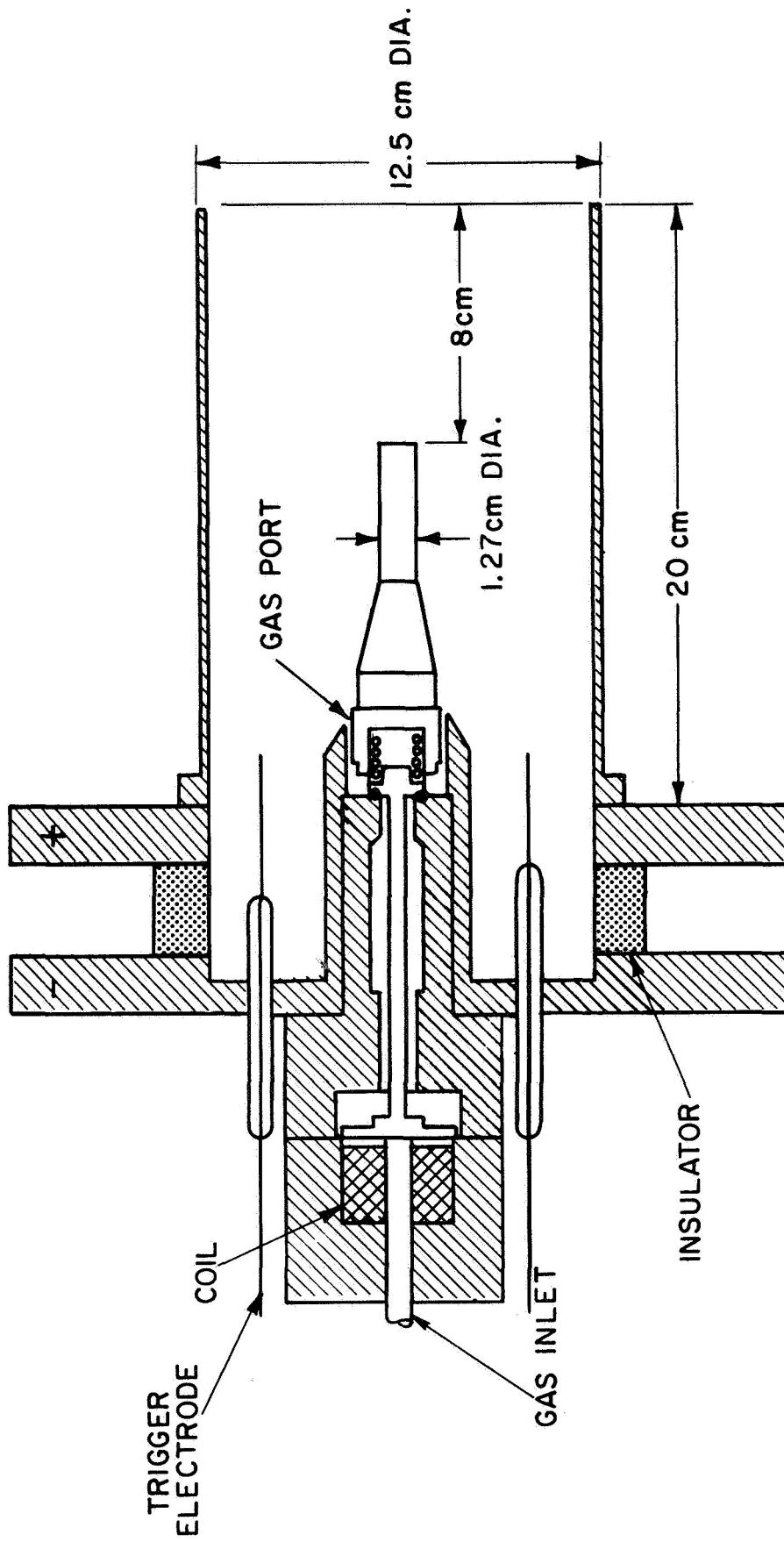
phase and continued to accelerate the working fluid. This has obvious implications for higher exhaust velocities if the current pulse could be sufficiently protracted.

Two problem areas remain that are not directly associated with any one of the three distinct phases. The first of these concerns the electrode emission process throughout the pulse. Superficially, there is a tendency to feel that the time scale on which the pulsed accelerator operates is probably inadequate to attain the prolific thermionic emission of electrons from the cathode which is characteristic of high-current steady arcs. Nevertheless, it is important to achieve this type of emission because the associated small voltage drop at the cathode (the cathode fall voltage) is reflected in a greater overall efficiency. Larger cathode fall voltages associated with nonthermionic emission not only cause greater power losses, but frequently cause cathode erosion due to the sandblasting effect of ions accelerated by this voltage. Longer pulses may alleviate this problem in that a more stable discharge might be generated, allowing in turn sufficient local heating for thermionic emission to prevail.

The second problem area concerns the reliability of the complete thruster system. Since the pulse duration was limited to one to ten microseconds, delivery of a required total impulse dictated a total number of individual pulses. For realistic missions, this implied 10^7 to 10^9 pulses [58]

indicating the importance of system reliability and electrode integrity. Particularly significant is the burden that such a large number of pulses places on the capacitors and on the switch between the power supply and the thruster. Several types of switches have been used in pulsed plasma propulsion, with a complete description of each given in Ref. [43]. Regardless of the particular configuration, it was clear that if a longer pulse were used, and if the thruster continued to accelerate injected mass during this increased pulse, then fewer pulses would be required for the same total impulse. Consequently, the reliability demands on the switch, capacitors, and thruster would be considerably relaxed.

The summation of these observed difficulties was reflected in the overall efficiency measured in typical pulsed systems. Larson [3] measured an overall efficiency of up to 45 percent and speculated that 50 percent appeared to be a ceiling for that system. Gorowitz, using the configuration shown in Fig. 3-1 [2], claimed a maximum overall efficiency of 70 percent at a specific impulse of 9,000 seconds. However, due to the specific mass of anticipated electric power supplies, the optimum specific impulse for near-planet missions is approximately 5,000 seconds [18,19]. At this value, the latter system had an efficiency of 45 percent. Thus, it appears that although certain advantages accrue from rapidly pulsed plasma accelerators, this same transient process predicates unique loss mechanisms which limit the overall efficiency to values considerably lower than desired.



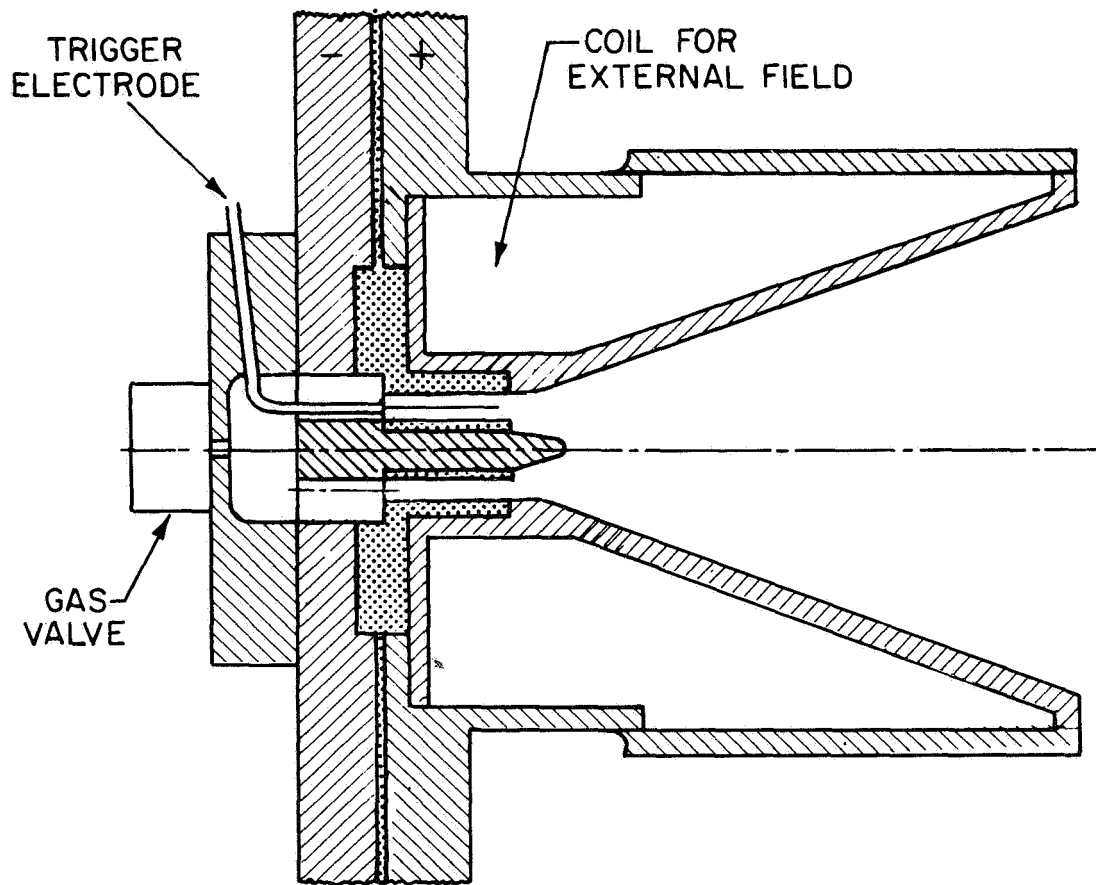
EARLY PULSED THRUSTER (REF. 2)

FIGURE 3-1

IV. EXTENDED PULSE OPERATION

From studies like those mentioned above, it has become apparent that many of the operational difficulties could be reduced by protraction of the driving current pulse. In essence, performance improvements may be anticipated by extension of the electrical and injected mass inputs thereby confining the more troublesome aspects of the acceleration process to the extremities of the pulse. In other words, the problems of sheet formation, mass sweeping, and uncoupling of the sheet from the power supply may assume a relatively lesser importance if, during the center portion of the pulse, the discharge functions as a high-power steady state accelerator.

One of the first attempts at operation of a thruster with an extended pulse was reported by Ashby [58]. Since the implications of prolonged pulses regarding both MPD simulation and quasi-steady propulsion had been realized by this time [59,60], the geometry of this thruster more closely resembled the steady state device (see Fig. 3-2). Note that an external magnetic field was added to improve the performance in the lower power regime. The performance of this accelerator was in fact lower than the older pulsed thrusters (overall efficiency of about 25 percent at a comparable specific impulse) and was complicated by two problems. First, with these longer pulse times, current was able to flow in the expanding exhaust plume and consequently in the metallic vacuum tank walls. In fact, the maximum input power conditions were stipulated as



0 1 2
SCALE: inches

AP 25 R 4478 - 68

EARLY EXTENDED PULSE THRUSTER WITH EXTERNAL MAGNETIC FIELD (REF. 58)

FIGURE 3-2

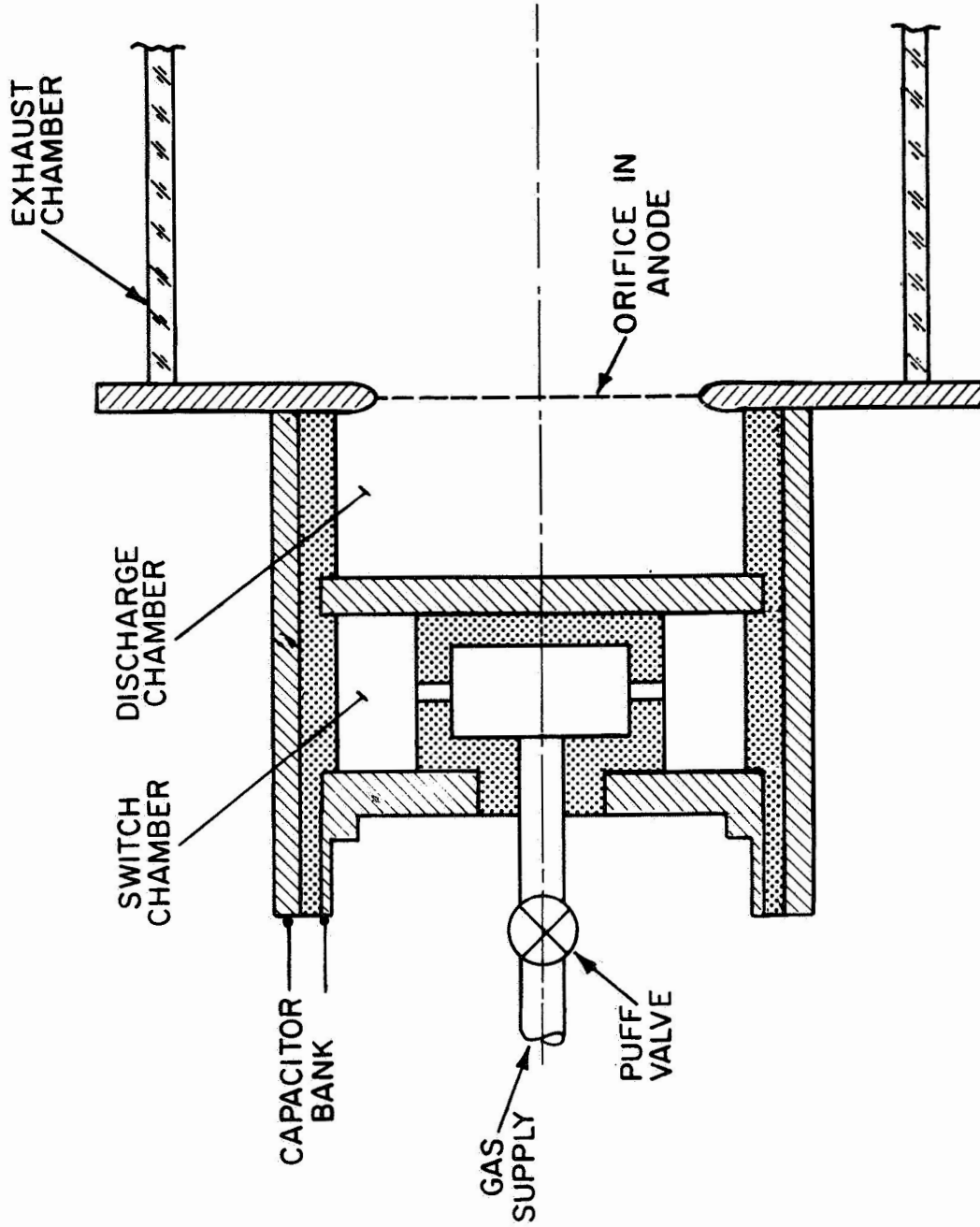
those where tank currents did not flow - 25 to 250 kW depending on the propellant. The second problem was associated with the mass injection system. Because this thruster was an extension from the operation at shorter time scales, the mass supply system closely resembled its forerunner. This apparatus consisted of a small, high pressure plenum whose passages to the main arc discharge chamber were sealed by an electromagnetic valve (see Figs. 3-1 and 3-2). The advantages of such a system are that it can be repetitively pulsed and easily synchronized with respect to the electrical pulse by an electronic delay network. The disadvantages are twofold: First, the time starting when this valve begins to open until "steady" mass flow conditions are reached in the arc chamber can be several milliseconds. For a quasi-steady acceleration experiment, the electrical pulse should be delayed until this steady condition has been reached. Consequently, sufficient mass can enter the vacuum chamber in this time increment to lower the mass utilization and compromise the space environment established initially. In addition, the resulting higher back pressure may prohibit certain exhaust plume diagnostics, such as ion energy analyzers, which require a large mean free path outside the exhaust plume. The second disadvantage of this technique is that no truly steady mass flow is reached since the pressure in this small reservoir continually decays with time. This can become especially serious as the electrical pulse time is increased.

A later long-pulse thruster for MPD simulation was developed by Lovberg, et al. [61]. It too had an external magnetic field, a similar mass injection system, and was confined to power levels below approximately 100 kW. An added feature of this experiment was artificial heating of the cathode to ensure thermionic emission. Although overall performance measurements were not the purpose of this experiment, detailed diagnostics in the interelectrode region quickly revealed the presence of a rotating spoke discharge. Only after this result was reported was the same phenomena verified in steady state experiments operating at similar conditions. This point should be emphasized; namely, this well-designed pulsed simulation experiment revealed particular information on low power MPD thrusters which had not been realized in two years of steady state testing. The similar application of appropriate diagnostics to a properly designed quasi-steady accelerator operating in the high power regime may well be equally productive.

Both of these extended-pulse thrusters performed mainly in the low power, external magnetic field domain characterized by rotating arc filaments, ponderous auxiliary magnets, and a complex interplay between various $\vec{j} \times \vec{B}$ forces. However, as shown earlier, the indicated high-efficiency operation is at the high power end of the spectrum dominated by the self-magnetic field effect. Long-pulse experimentation in this latter regime has been done by Jahn [9] at about the same time as the

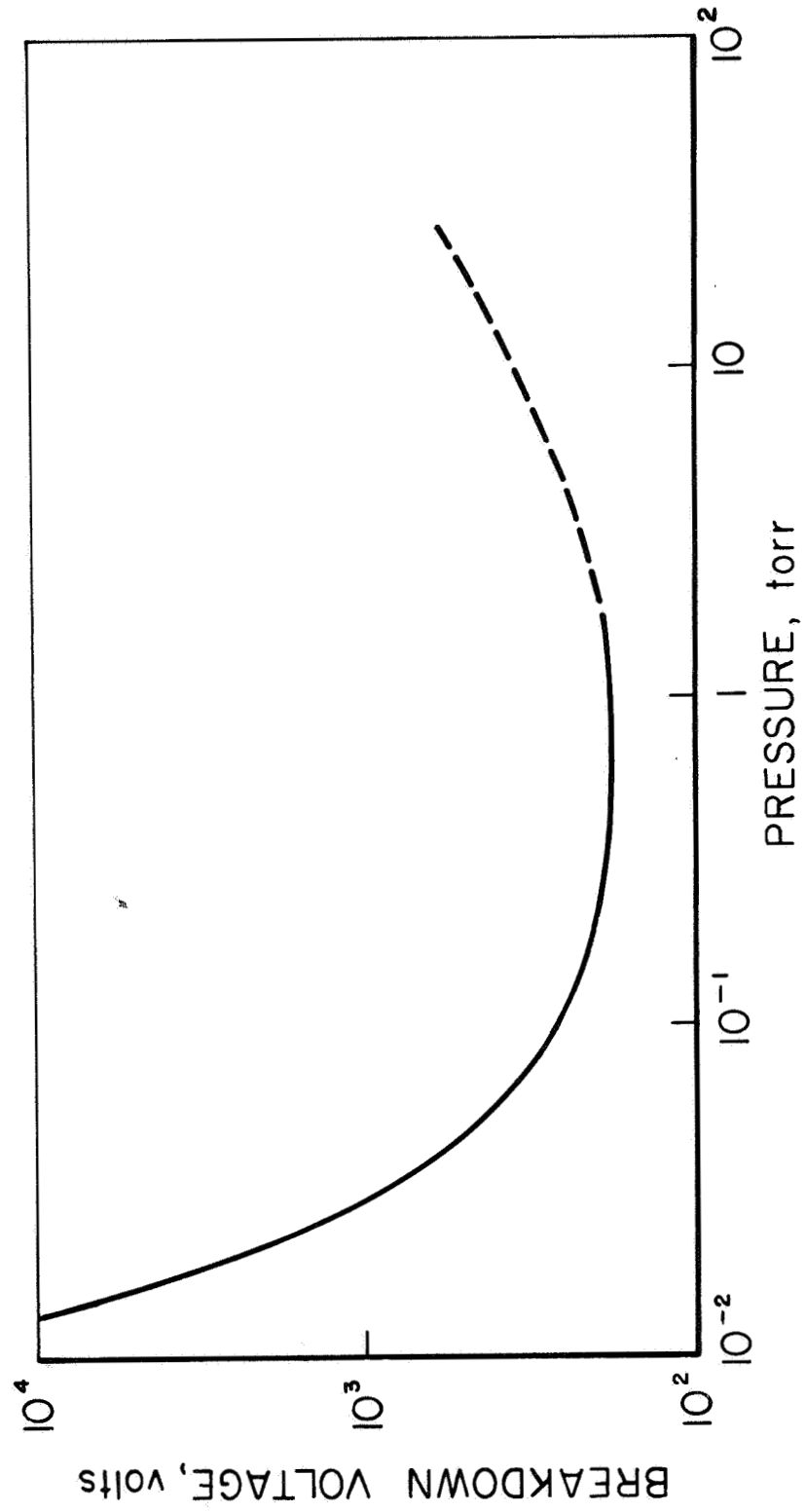
early external field work of Ref. [58]. The configuration used is shown in Fig. 3-3 and is seen to be similar to that shown in Fig. 1-1b — with internal arc chamber dimensions of 2-in. height by 5-in. diameter, an orifice diameter of 4 in., and a Pyrex exhaust vessel diameter of 9 in. The gas-triggered electrical switch, which has been described in detail elsewhere [62], is shown directly behind and coaxial with the main discharge chamber. The electrical breakdown in both chambers is governed by the Paschen curve for the particular electrode spacing [63]. Figure 3-4 shows this characteristic breakdown voltage versus pressure for a 2-in. gap in argon. The pressure in the switch is maintained sufficiently low so that the full power supply voltage can be applied across it without causing a breakdown, i.e., a switch pressure of less than 10^{-2} torr for the 10 kV maximum voltage. The pressure in the main chamber is preset to a value that will not hold off this same voltage. When a puff of gas is then injected into the switch chamber, a spontaneous breakdown occurs transferring the bank voltage to the main chamber and thereby initiating the acceleration process at the preset pressure.

Initial tests were performed with a flattop driving current pulse of 200 kA for 5 μ sec using the pulse-forming network described in Ref. [10]. A uniform argon pressure of 0.12 torr was set throughout the main chamber and exhaust vessel. Routine probing of the discharge region by magnetic



SWITCH AND PINCH - ORIFICE CHAMBERS (REF. 9)

FIGURE 3 - 3



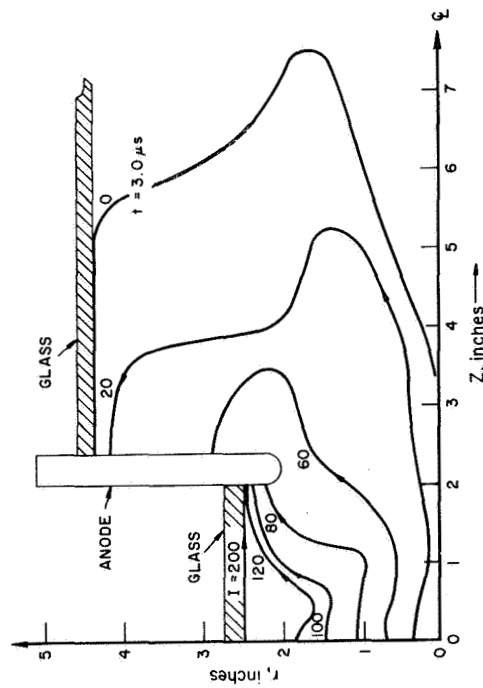
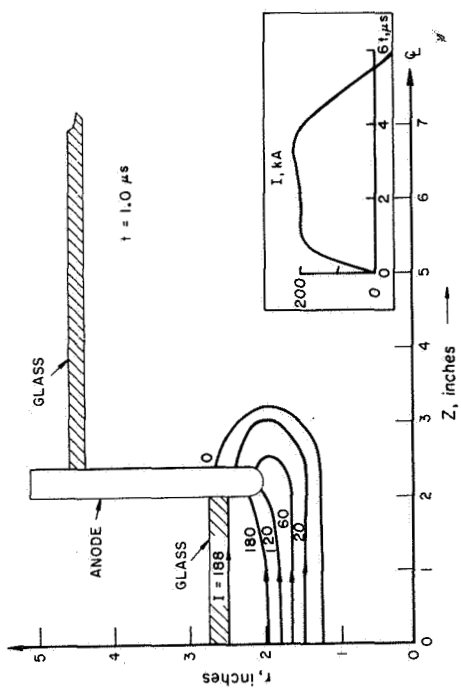
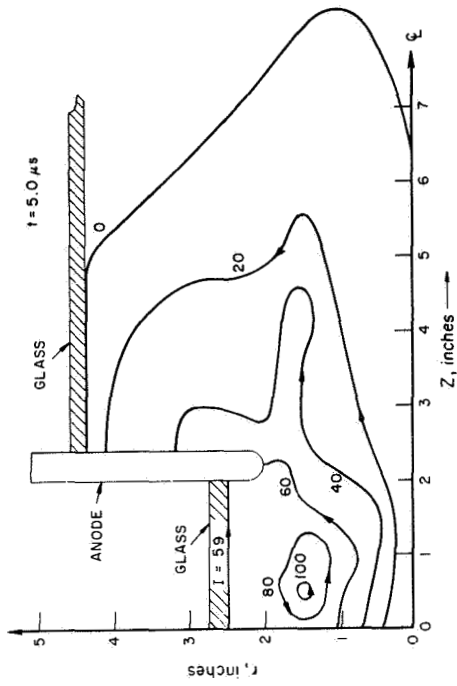
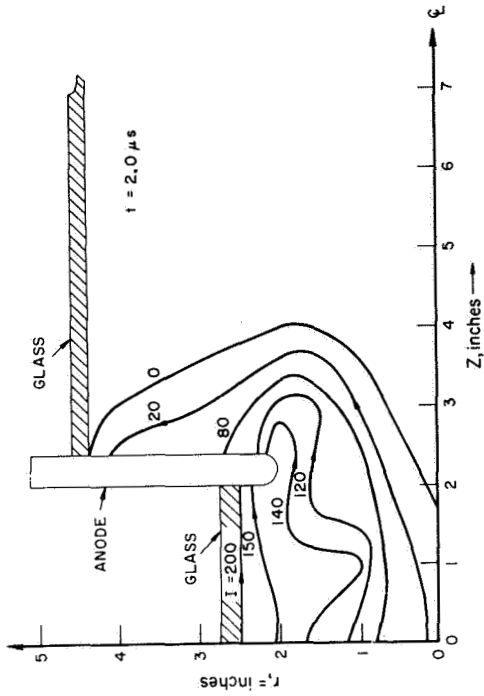
PASCHEN CURVE FOR ARGON WITH 2 in. GAP (REF. 64)

probes¹ revealed the current distribution development shown in Fig. 3-5. The data here are presented as contours of total current enclosed within the radius of the field point. The observed slowing of these enclosed current contours along the anode face could have been caused by either a gas-dynamic influence of the exhaust vessel wall or the natural development of a stabilized discharge current pattern. Experimental indications of this latter possibility were also being reported by Larson at this time [3].

In order to determine unambiguously the cause of the observed current pattern slowing, the experiments were continued with the following changes: First, a larger capacitor power supply was installed. It consisted of a bank of $40 \times 3.2 \mu\text{F}$ units, replacing the former bank of $20 \times 2.5 \mu\text{F}$ units. The bank was charged to 10 kV before each pulse, representing a total stored energy of 6,400 J. With the appropriate interchangeable inductors between the capacitors, this system was capable of providing flattop current pulses from 35 kA to 140 kA. At the highest current, the pulse was 20 μsec long, with lower currents being driven for proportionally longer times.

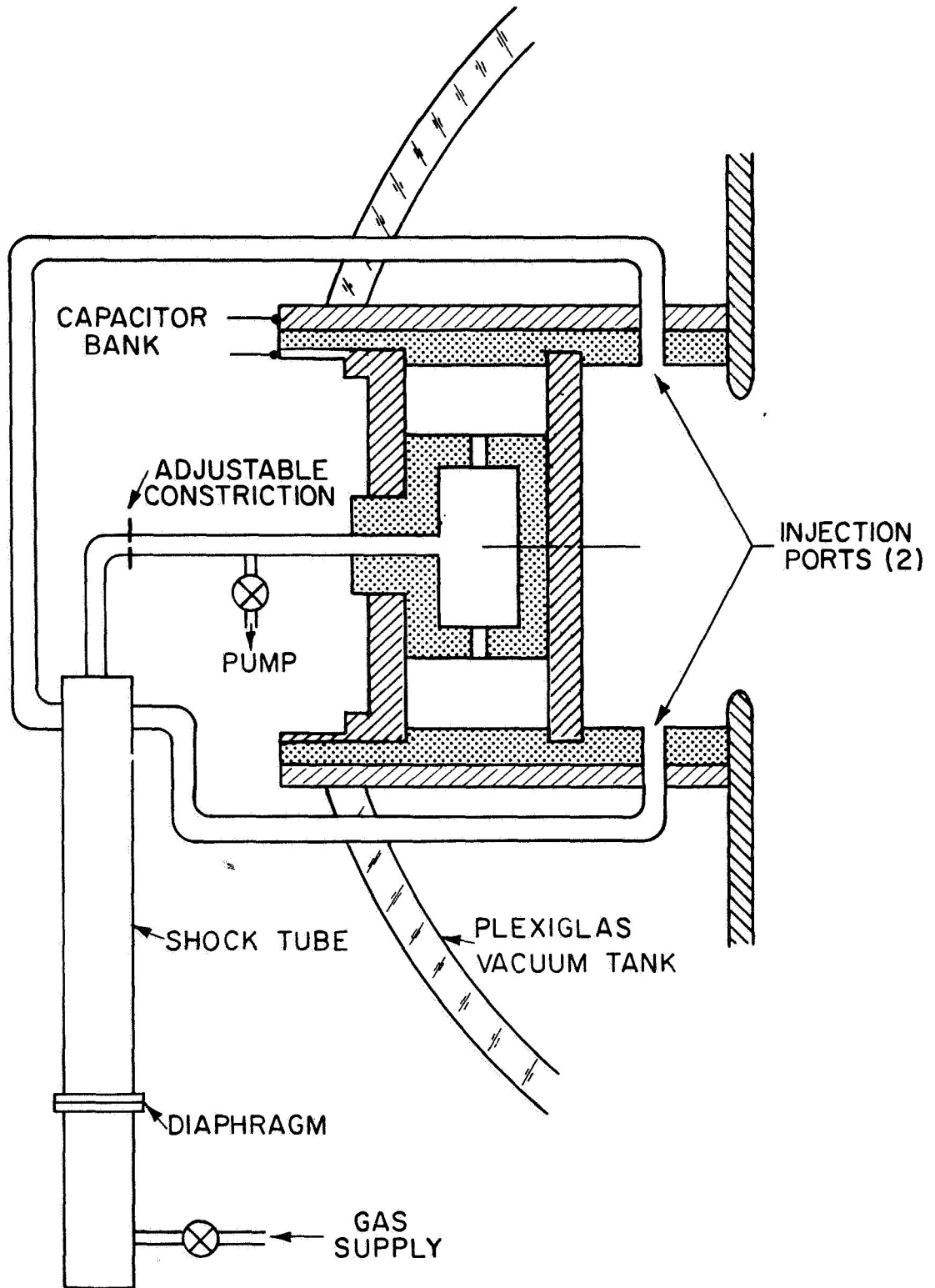
Second, a shock tube gas injection system was installed. This system, shown schematically in Fig. 3-6, utilizes a small shock tube (12-in. driver section, 21-in. driven section,

¹A complete description of magnetic probes and their applications has been presented in Ref. [65].



CURRENT PROFILES WITH 9 in. DIA. EXHAUST VESSEL,
0.12 torr ARGON, 200 kA X 5 μsec PULSE

FIGURE 3-5



AP 25 R 4480 - 68

SCHEMATIC OF EARLY SHOCK TUBE MASS INJECTION SYSTEM

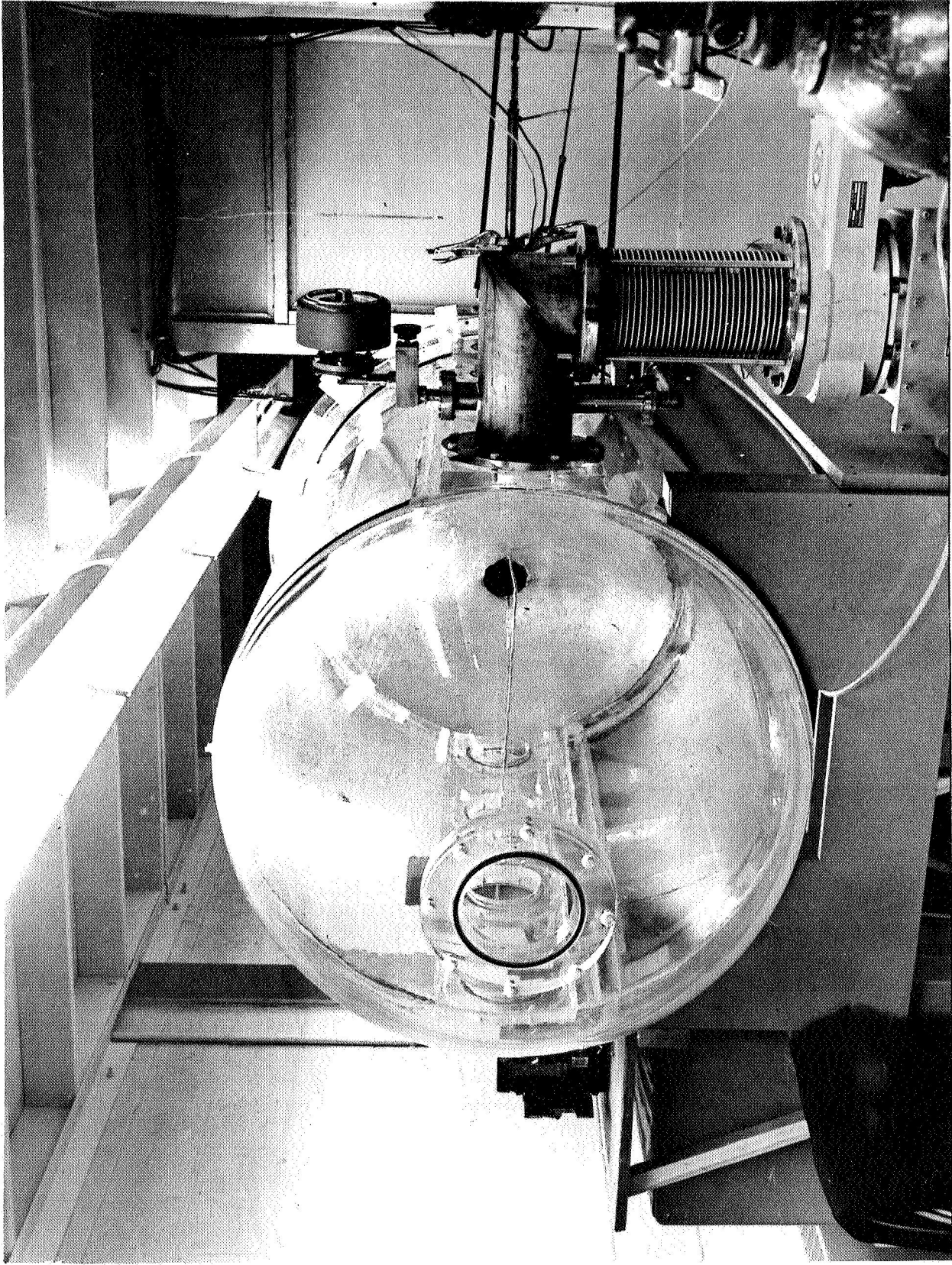
FIGURE 3-6

7/8-in. diameter) whose driven section is connected by flow passages to both the main discharge chamber and the switch chamber. Initially, these interconnected elements are all pumped out to some low pressure (10^{-3} torr or lower) while the driver section is pressurized to two atm argon and the capacitor bank charged to 10 kV. When the diaphragm is ruptured, a puff of gas goes into the main chamber and a secondary puff begins to fill the switch chamber. By proper adjustment of the orifice in the line feeding the switch, the breakdown can be delayed until a prescribed pressure exists within the main chamber. (The pressure level is established by a comparison of Kerr-cell photographs of the pressure-dependent pinch process for both the shock tube mode and ambient prefills to various uniform pressures. Agreement of the pinch times between the two modes indicates an average pressure for the shock tube case equal to the corresponding ambient case.) The primary advantage of such a gas injection system when compared to the previously mentioned electromagnetic valve resides in its rapid mass flow rise time to an appropriate operating condition (less than 1 msec), thus producing a better simulation of a space environment. In addition, such a system does not require a special external synchronization circuit. However, due to its relatively long reset time, it cannot be incorporated into a configuration which will be repetitively pulsed at a high frequency.

Finally, unhindered development of the exhaust plume

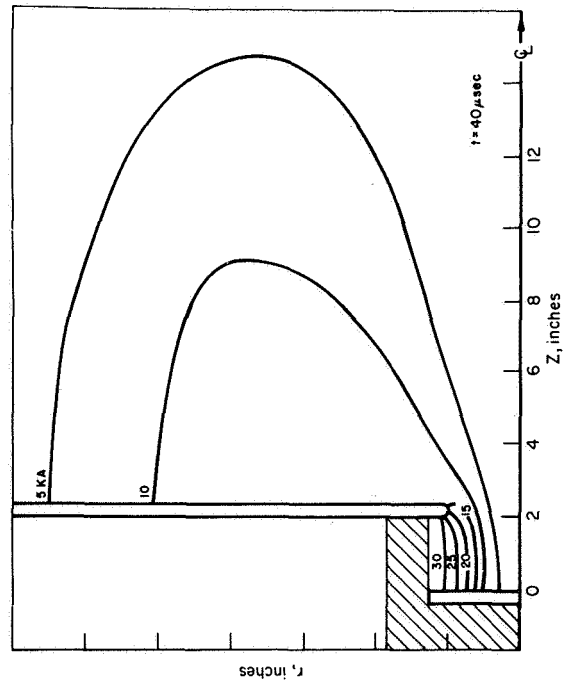
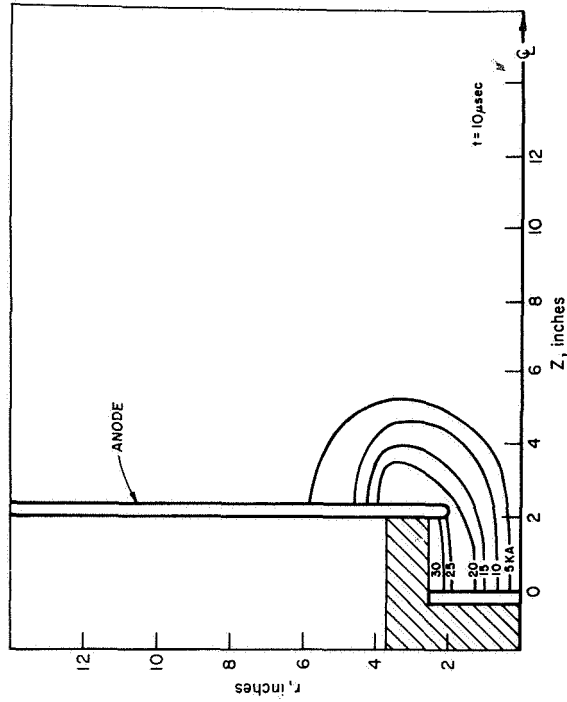
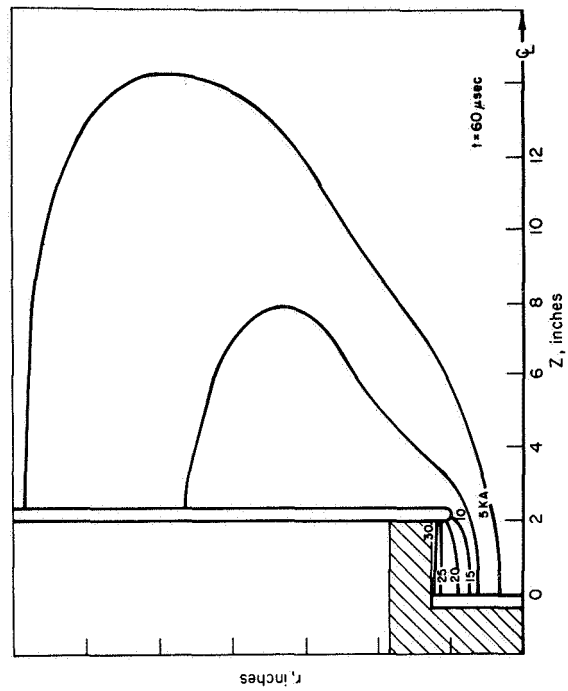
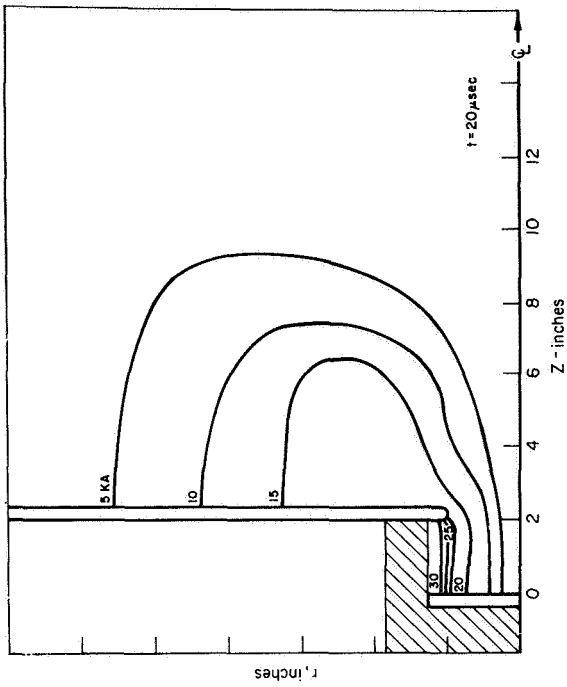
was allowed by the construction of a special plexiglas vacuum tank [66]. This 3-ft. diameter by 6-ft. long tank, shown in Fig. 3-7 with its 6-in. oil diffusion pump and associated backup pumping apparatus, was constructed entirely of dielectric material to prevent current conduction or induced currents from flowing in its walls. Its large size enables the anode face diameter to be increased to 34 in. as seen in Fig. 3-7 while maintaining the same discharge chamber and orifice dimensions. With this tank, back pressures of less than 10^{-5} torr provide an effective simulation of a space environment since the mean free-path of the resident particles is then larger than the tank dimensions. Details of the method of construction and outgassing characteristics of this unique facility are available in Ref. [66].

Having made these changes, the development of the chamber discharge and exhaust plume for shock tube injection of argon with a 35 kA by 80 μ sec input pulse is shown in Fig. 3-8. It is observed that after about 40 percent of the pulse time, the initially rapid propagation of an intense current sheet has stabilized into a much more diffuse current conduction pattern. Experiments with a parallel-plate accelerator have shown that a similar stabilized current configuration can be obtained, and that in this one-dimensional geometry, the current sheet continues to accelerate mass through itself after stabilization [67]. This distinct transition from a sweeping mode characteristic of early pulsed plasma accel-



LARGE ANODE WITH EXHAUST ORIFICE INSIDE PLEXIGLAS VACUUM TANK

FIGURE 3-7



ENCLOSED CURRENT COUNTERS IN LARGE PLEXIGLAS EXHAUST TANK,
SHOCK TUBE INJECTION
35 kA X 80 μ sec PULSE

FIGURE 3-8

erators to a diffuse "blowing" mode typical of steady state accelerators indicates that the former may just be the starting phase for the latter. Thus, the possibility of variable-power MPD simulation and high power, high efficiency intermittent acceleration has again been broached, only this time as a result of a logical development from a completely unsteady plasma accelerator.

CHAPTER 4

DESIGN CONSIDERATIONS AND REQUIREMENTS

I. INTRODUCTION

In the preceding brief reviews of both steady and pulsed plasma propulsion, it has become obvious that both of these disciplines provide some basis for a long-pulse mode of operation. Although the respective arguments are guided by totally different experimental results and problems, the goal is essentially the same: namely, access to the high power regime which appears to provide the best potential for highly efficient plasma acceleration, at modest average power consumption. Thus, quasi-steady operation represents the merger of two initially distinct propulsion techniques into one which may embody the most favorable aspects of each. With the development of a quasi-steady facility which would permit detailed study of various aspects of this mode as the immediate goal, the following considerations and requirements are examined.

II. CURRENT DISTRIBUTION

The fundamental requirement for any quasi-steady accelerator to fulfill in order to bear relevance to a similar steady state configuration is that its current distribution

must stabilize to some steady pattern on an appropriately short time scale. This transition from a propagating current sheet to a steady distribution has been observed to proceed via various routes. In one experiment, for example, the enclosed current contours initially billowed outward into the near exhaust, gradually slowed as the transition took place, and stopped at some equilibrium position [12]. In another experiment, an intense current front was driven outward from the exhaust plume unrolling behind it a steady distribution of current density [68]. The particular transition mode which a given discharge elects may be due in part to geometry, initial mass distribution, or some unknown factor, but regardless of the contributing elements, the resulting stabilization is an absolute necessity for a quasi-steady accelerator. It seems reasonable to anticipate that, because of the widely variant geometries and mass injection schemes where stabilization has been observed, new accelerators, based largely upon extensions of earlier configurations, will also produce stabilized current patterns.

III. MASS FLOW RATE

Merely duplicating the exhaust current density profiles is not sufficient to establish full relevance of the quasi-steady operation to its steady counterpart. A second major factor to be considered is the establishment of a quasi-steady mass flow of appropriate and adjustable rate

through the discharge chamber, on the time scale of the rest of the experiment. This required mass flow rate must conform to the thrusting capability of the self-field pattern for the desired specific impulse. For a purely self-magnetic thruster with a uniform cathode current distribution, the electromagnetic thrust generated has been shown on page 30 to be

$$T = \frac{\mu J^2}{4\pi} \left[\ln \left(\frac{r_a}{r_c} \right) + \frac{3}{4} \right] \quad (4-1)$$

Since this must be equal to the momentum increase of the working fluid, the appropriate mass flow rate can then be found for any specified exhaust velocity or specific impulse from

$$T = \dot{m} U_{ex} = \dot{m} I_{sp} g \quad (4-2)$$

where \dot{m} = mass flow rate

U_{ex} = exhaust velocity

I_{sp} = specific impulse

g = sea level gravitational acceleration

Such a set of calculations are shown in Fig. 4-1 for an anode-to-cathode attachment radius ratio of 5.6, a value which corresponds to current density distributions presented in a later chapter. (It should be noted, however, that this thrust calculation is not sensitive to r_a/r_c due to the logarithmic behavior.) It is seen from Fig. 4-1 that currents from 10^3 to 10^5 A dictate mass flow rates from 10^{-2} to

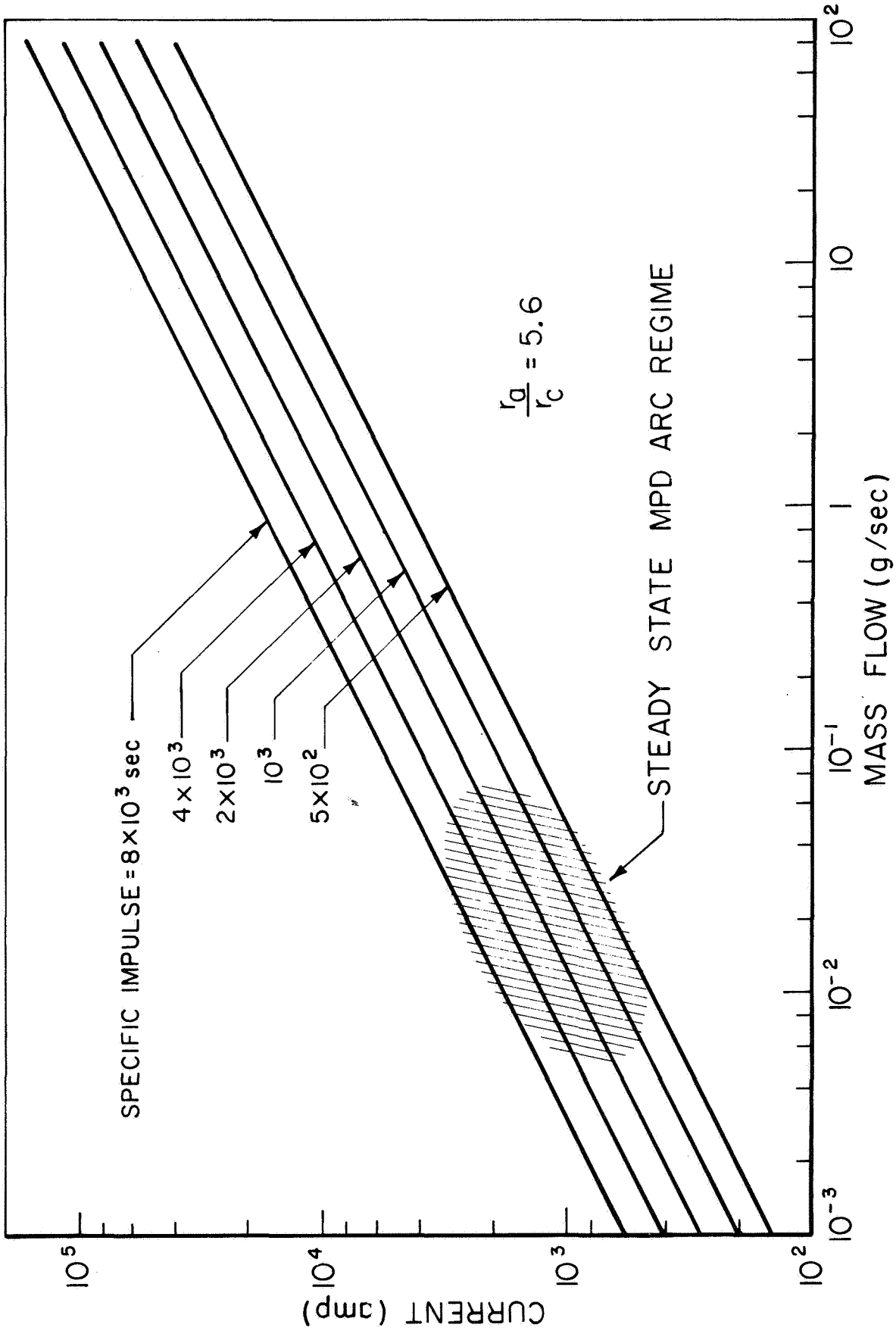


FIGURE 4-1

MASS FLOW FOR PURELY ELECTROMAGNETIC THRUST

10^2 g/sec. A mass injection system capable of providing these flow rates would enable operation over the range from present steady state MPD arcs up to power levels several orders of magnitude higher. It is interesting to note that operation in the upper left portion of Fig. 4-1 implies extremely high specific impulse values. However, if the mass flow rate is continually decreased for a fixed current in order to get into this regime, the arc operation may change in a manner such that this high performance is impossible. This point will be discussed at greater length when the voltage measurements are presented.

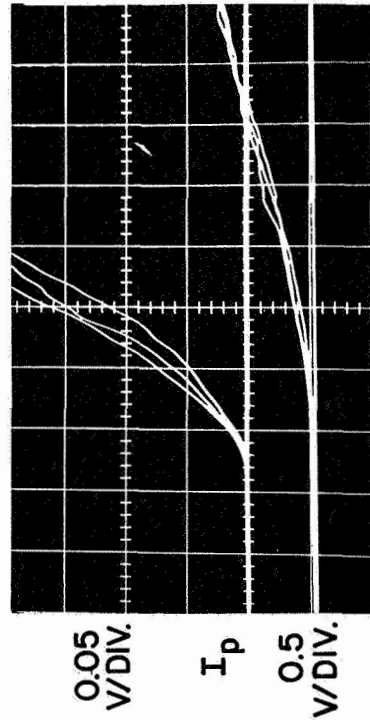
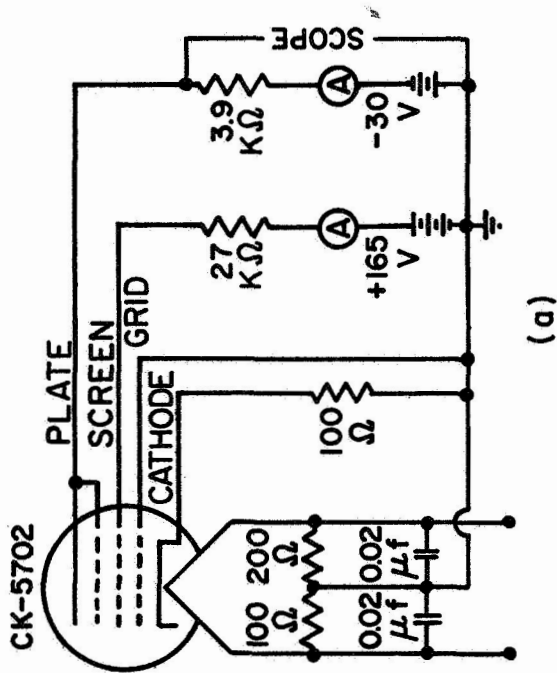
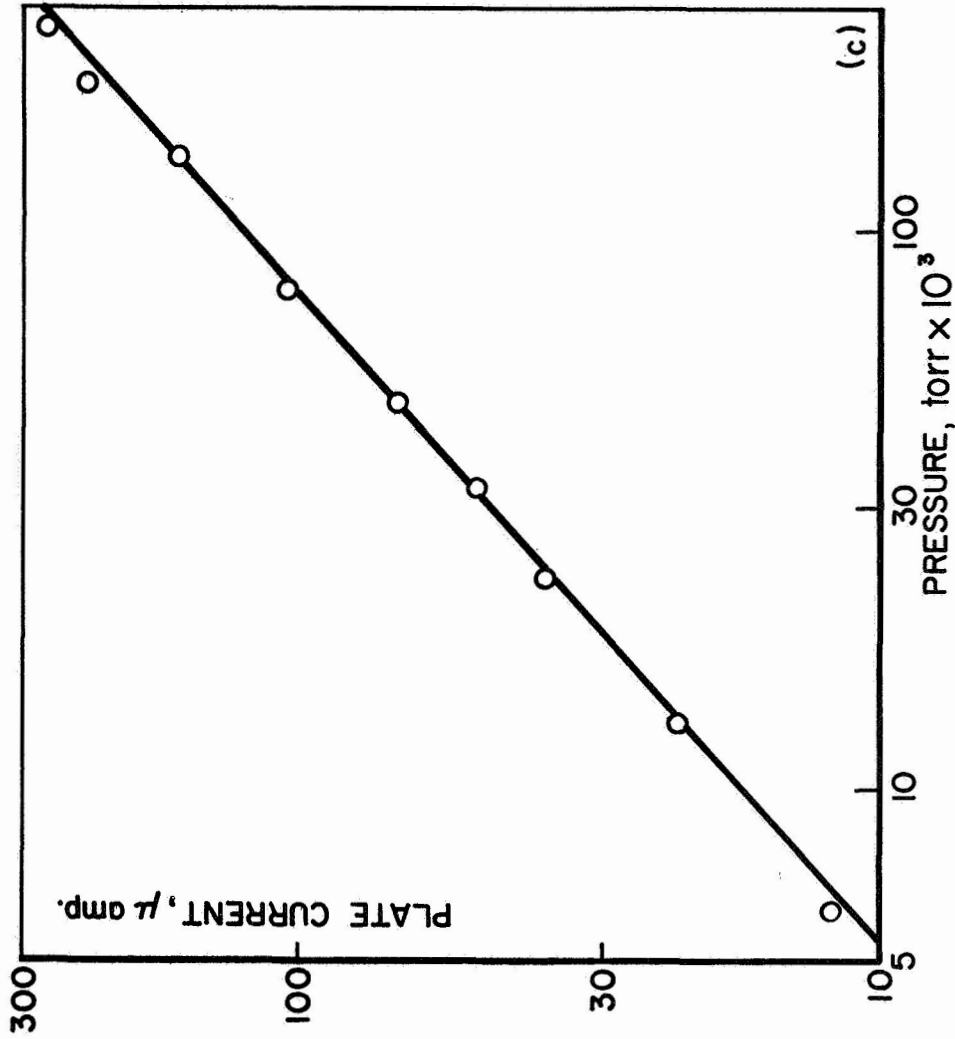
In addition to demanding a large and quasi-steady mass flow rate from the mass injection system, it is equally important that this mass flow be pulsed into the thruster in order not to compromise the space environment in the region downstream of the arc chamber. It follows that the rise time to the steady value be as short as possible in order to maintain the highest possible mass utilization fraction and the best simulation of a space environment. A further benefit that would accrue from a short rise time would be the ability to perform certain exhaust beam diagnostics (such as ion energy analyzers) which require nearly collisionless flow of the ionized accelerated species through the background gas.

In order to establish the gasdynamic characteristics of various injection systems, a fast response miniature ionization gauge [69,70] was constructed for measuring neutral

particle densities. This device consists of a small pentode (CK-5702) operating without its glass envelope and with its elements biased as shown in Fig. 4-2a. Ions, formed in the vicinity of the screen by collisions between high velocity electrons and resident neutral particles, are collected by the negatively biased plate and suppressor. The choice of resistances in the cathode and screen legs provides sufficient negative feedback to keep the electron emission current constant to within 5 percent during a gas pulse. When mounted within the environmental tank, the gauge is capable of measuring pressures in the range of 10^{-5} to 0.3 torr, with a time response considerably shorter than 10 μ sec, and with a measuring volume of approximately 1 cm^3 .

This device was first used to map the neutral density profile for the shock tube gas injection system described previously. The gauge was mounted on a movable probe carriage in the plexiglas vacuum tank to enable both axial and radial traversing. Tank pressure before each shot was less than 10^{-5} torr and the shock tube driver pressure was 2 atm to match the conditions for the earlier exhaust plume current conduction pattern measurements. An accurate time reference to correlate the pressure profiles was obtained by triggering the oscilloscope from the output of a piezoelectric pressure transducer mounted in the driven section of the shock tube.

Figure 4-2b displays a typical triple overlay of the gauge plate current versus time at the center of the pinch



a) CIRCUIT DIAGRAM OF FAST IONIZATION GAUGE, WITH b) TYPICAL RESPONSE OSCILLOGRAM AND c) CALIBRATION CURVE

(b) PLATE CURRENT AT CENTER OF PINCH CHAMBER
100 μ sec./DIV.

FIGURE 4-2

chamber. The plate current was measured at three sensitivities, each an order of magnitude apart (the most sensitive not shown) to facilitate accurate pressure determination over the entire range of the gauge. Conversion of the plate current data to pressure data was accomplished by the calibration curve of Fig. 4-2c which was found to be the same for all pentodes used.

In Fig. 4-3, the oscilloscope traces shown in Fig. 4-2b have been reduced to give the pressure history in the center of the discharge chamber. Superimposed on each data point is an error bar which represents the total error due to emission current drift and statistical fluctuations in the piezoelectric trigger, diaphragm rupture, and actual gasdynamic exhaust pattern. Although the nature of the ionization gauge precluded its operation during an actual discharge of the accelerator, the chamber static pressure at the time of electrical breakdown was established as 0.1 torr to 10 percent accuracy by a Kerr-cell comparison of shock tube and ambient fill pinch times as discussed in Chap. 3. Referring to Fig. 4-3, it is evident that the electrical breakdown occurs with this configuration approximately 560 μ sec after the pressure first begins to rise in the chamber.

Figure 4-4 shows the axial pressure profile at 100 μ sec intervals after the pressure first begins to rise in the arc chamber. In Fig. 4-5, the radial pressure profile growth in a plane perpendicular to the axis and two inches downstream of the anode is also shown. It is apparent that at the time

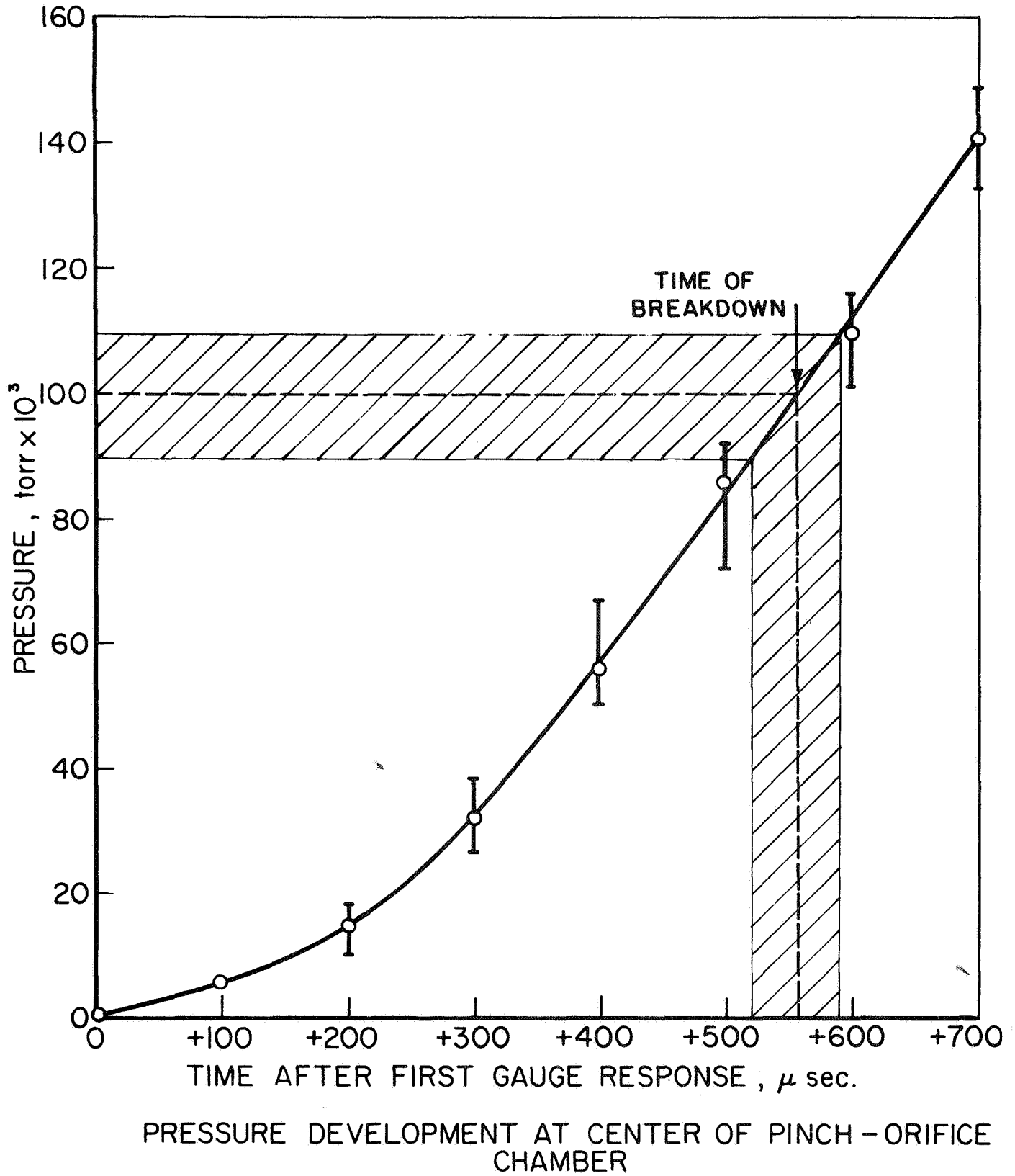


FIGURE 4-3

AF 25 9328A-67

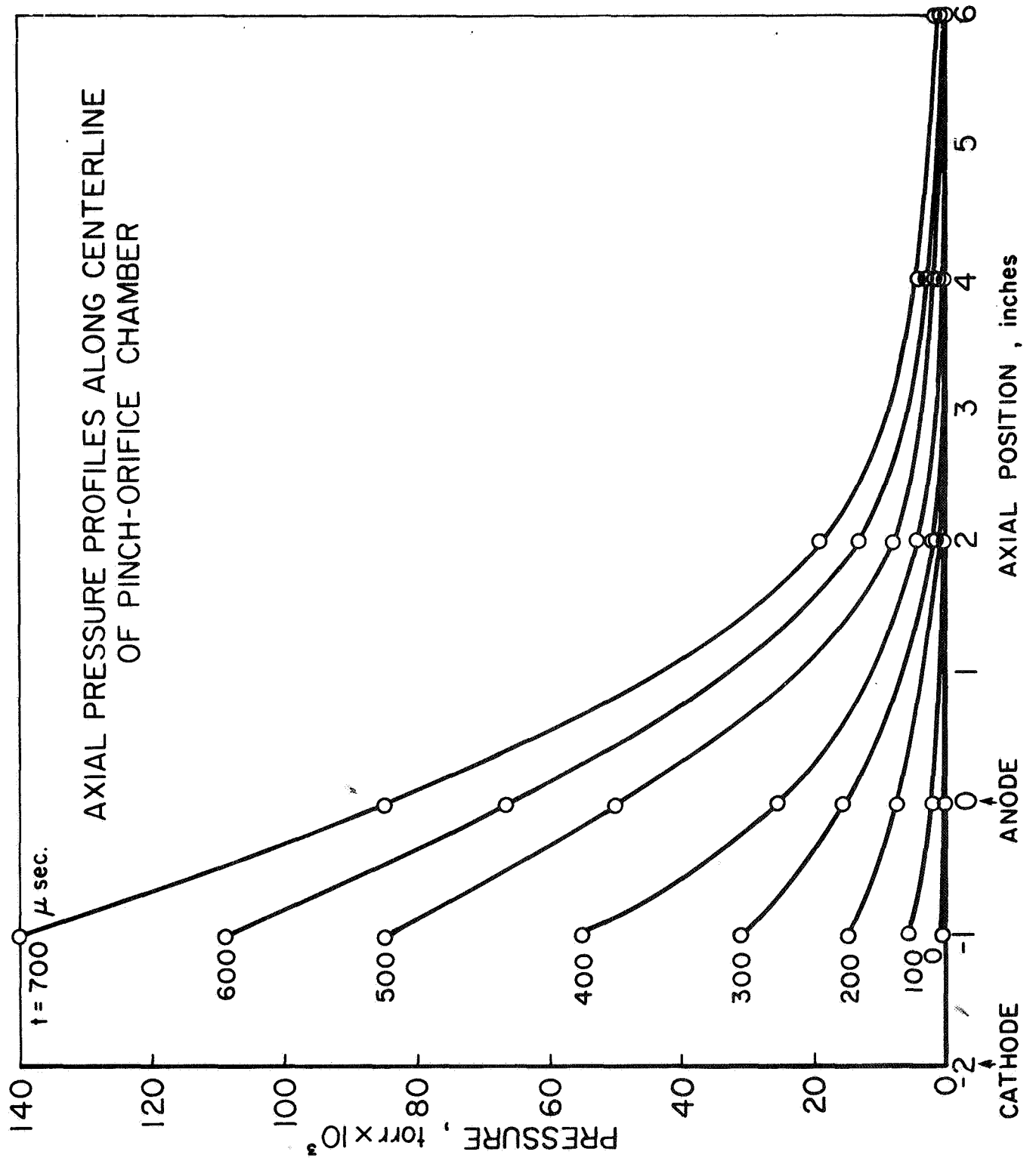
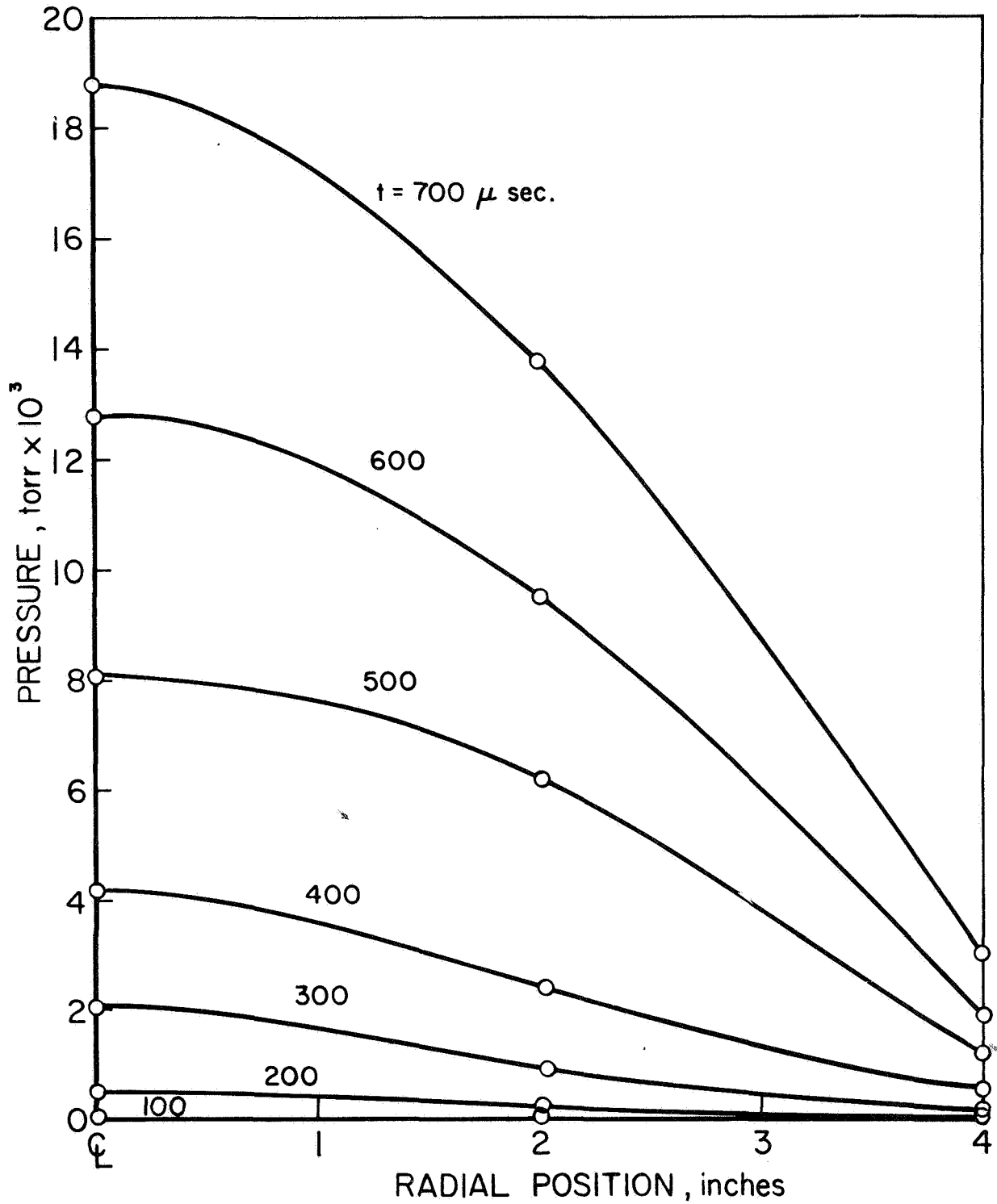


FIGURE 4-4



RADIAL PRESSURE PROFILES 2" DOWNSTREAM OF ANODE
OF PINCH ORIFICE CHAMBER

FIGURE 4-5

of electrical breakdown, both the axial and radial pressure decays are sufficiently rapid so that the tank walls do not interfere with the exhaust plume growth.

The steep pressure-time history observed with this gas injection system was appropriate for the shorter current pulses used in conjunction with it. However, for pulses longer than about 100 μsec , as contemplated for MPD simulation and quasi-steady thrusting, this system is inadequate in that no steady mass flow phase occurs on a reasonable time scale.

A further complication surrounding the mass injection system arises when the interaction between it and the superimposed current pulse is considered. If the mass pulse is properly injected, then the pressure distribution awaiting the current pulse will be some steady value within the discharge chamber, corresponding to the steady mass flow rate, with a rapid decay outside the chamber to the background value. When the discharge initiates, the propagation of the current density distribution characteristic of the initial transient phase will disturb the injected mass distribution to a certain extent. In the extreme case of a perfectly snowplowing current sheet, the chamber would be evacuated completely. It follows that for a steady acceleration phase to occur, the current pulse must be sufficiently long to enable fresh gas to be processed by the subsequently stabilized current distribution, i.e., the current-mass flow interaction

must reach a state of dynamic equilibrium. Since the time constant for attaining this equilibrium will scale like a characteristic accelerator dimension divided by the acoustic speed of the incoming gas, it could become comparable to the total available pulse time from the power supply, whereas its desired magnitude is less than or equal to the time necessary for the current distribution to become steady. The specific value for this time constant will obviously depend upon the location of the anticipated stable current distribution. Hence, this effect can only be fully evaluated after detailed exhaust plume probing has revealed the nature and location of the transient and stabilized phases.

IV. OTHER CONSIDERATIONS

One obvious change that must be made between that geometry shown in Fig. 3-6 and one resembling a steady MPD configuration is the size and shape of the cathode. In the earlier configuration where stabilization was observed, the cathode was a large, flat disc instead of a cylindrical or conical shape. Nevertheless, for many operating conditions, the enclosed current contours were tightly constricted at their cathode attachment giving the impression of a virtual cylindrical cathode [71]. Not only would a conical cathode be better from a geometrical simulation point of view, but the forced constriction of all the current to a smaller area may bear favorably on the cathode emission factor, discussed below.

It has been emphasized that proper quasi-steady opera-

tion involves certain gasdynamic considerations as well as current conduction pattern stabilization. In addition, one of the most important, and perhaps the most troublesome aspect of this technique is the proper simulation of the electrode processes--emission, potential falls, and heat transfer. The desirability of thermionic emission of electrons from the cathode, both from the point of view of MPD simulation as well as improved overall efficiency, has been discussed in Chap. 3. Attainment of this emission mechanism will ultimately depend on the length of the current pulse and on the current density distribution over the cathode.

Although the cathode may get hot enough on the tip for thermionic emission, it is reasonable to expect that the bulk of the accelerator (insulators, anode, supporting structure) will not reach thermal equilibrium conditions commensurate with the arc operating power. This is unfortunate from the point of view of exact simulation of the steady state thruster. However, this same characteristic is a distinct advantage when considering quasi-steady operation at power levels much higher than steady state operation. In fact, the principle restriction on the maximum length of a high-current pulse may be based upon temperature limitations of the accelerator components. This is anticipated to be of the order of several milliseconds, which is considerably longer than the present capacitor bank capability.

V. SYSTEM REQUIREMENTS

In the above discussion, frequent reference has been made to the time constant of a particular event or the timing between several events. Since the distinction between a steady phenomenon and a transient one resides in the time scale by which the event is observed, the appropriate time constants of the problem will now be defined and the experimental requirements for proper quasi-steady operation expressed in this framework.

There are three characteristic times associated with the output of the capacitor bank and the subsequent electrodynamic plume development (see Fig. 4-6):

τ_l = the duration of the flattop current pulse

τ_r = the rise time of the current to its steady value

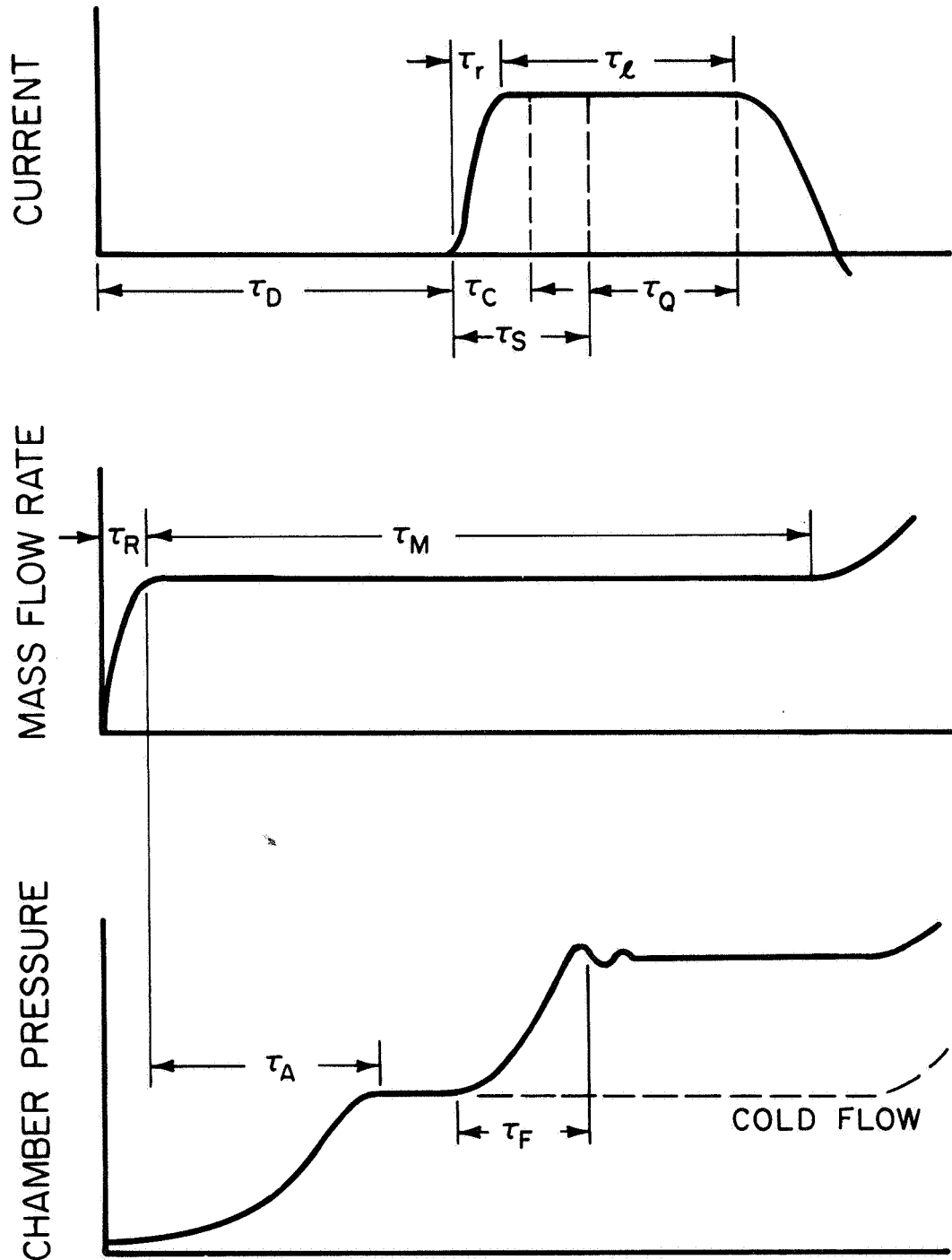
τ_s = the time from current initiation until stabilization occurs

An additional time of interest associated with the current pulse is

τ_c = the time which relates to the onset of thermionic emission from the cathode

In comparison to these, the following gasdynamic times are of interest:

τ_M = the interval over which the mass flow rate into the arc chamber is constant



CHARACTERISTIC TIMES FOR CURRENT PULSE AND MASS FLOW

τ_R = the time required for the mass flow rate into the arc chamber to reach its steady value

τ_A = the time required to reach a steady pressure in the arc chamber after the mass flow rate into it has become constant, i.e., the time from when the mass flow rate into the chamber is constant until the mass flow out of it is also constant

τ_F = the time necessary to get additional mass through the discharge region after the initial mass distribution has been disturbed by the transient phase

τ_D = the time from mass flow initiation until current initiation

In terms of these, the requirements of the gas injection system can then be summarized:

$\tau_R < \tau_M$ so that during τ_R the pressure distribution in the vacuum tank does not increase enough to compromise the space environment requirement

$(\tau_M - \tau_A) > \tau_l$ so that after the arc chamber pressure has reached its steady value, there is a constant mass flow rate for the duration of the current pulse

$(\tau_R + \tau_A) < \tau_D$ so that the current pulse only occurs after the steady state arc chamber pressure has been reached. However, it is best to keep τ_D close to its lowest acceptable value in order to maintain the background pressure as low as possible.

Thus, if these several time constants are of commensurate magnitudes, there remains an interval (τ_Q) during which reasonable simulation of steady operation should prevail.

With these general requirements stipulated, the following chapter will describe the development of the experimental apparatus necessary for proper quasi-steady operation.

CHAPTER 5

SYSTEM DESIGN

With the motivation and general requirements for a quasi-steady accelerator established, the following chapter will describe the development of new techniques and the extension of familiar ones to meet these requirements. Chapter subdivision is based on the three principle elements which contribute to the final configuration: current pulse-forming network, mass injection system, and accelerator geometry.

I. CURRENT PULSE-FORMING NETWORK

The power supply used throughout the experimental program is the same bank of $40 \times 3.2 \mu\text{farad}$ capacitors described previously. This bank, which is physically arranged in four lines of ten each, is used as a transmission line rather than a lumped capacitor supply in order that the resulting current waveform be protracted and flat. Thus, for an equal station-to-station inductance between each capacitor, three distinct pulse amplitudes and lengths are provided depending on whether the four lines are connected in parallel, series-parallel, or series combinations. For the initial set of inductors used with

this capacitor bank, nominally 0.2 μ Henry each, the available currents are 138 kA, 78 kA, and 42 kA. However, in order that the lowest current from the capacitor bank overlap the highest operating range of the steady state accelerator, an alternate set of inductors are employed. With these units, nominally 18 μ Henry each, the current range is extended down to values of 17.5 kA, 8.7 kA, and 4.4 kA. Hence, the complete driving current waveform capability and associated flattop current pulse length τ_l are as shown in Fig. 5-1. The current rise times τ_r are primarily due to the connection inductance between capacitor bank and accelerator, and since this value is adjusted to produce the fastest rise time without overshoot, it in turn reflects the inter-stage inductance. Thus, each of the three higher currents has a 2 μ sec rise time while each of the three lower currents has a 15 μ sec rise time.

A typical current waveform delivered by the capacitor bank to the accelerator is shown in Fig. 5-2a. This signal is the integrated output of a Rogowski coil [65] placed around the insulator between anode and cathode. Since the characteristic output of a Rogowski coil is a voltage proportional to the time rate of change of magnetic flux threading its coils, it is thus proportional to the time derivative of the current. Integration to display the total current is performed passively with an RC integrator at the oscilloscope, the integrator time constant producing the slight signal decay

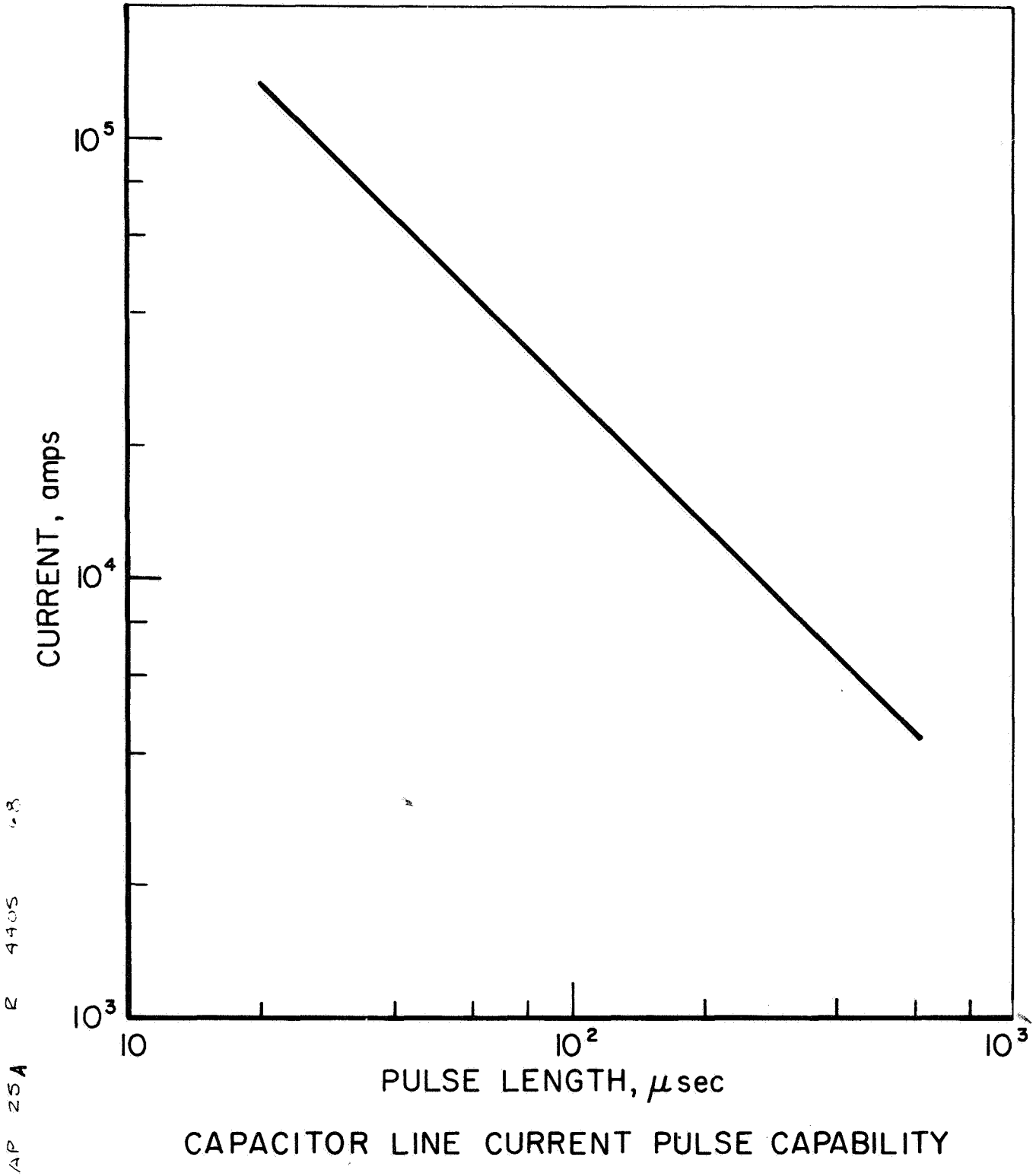
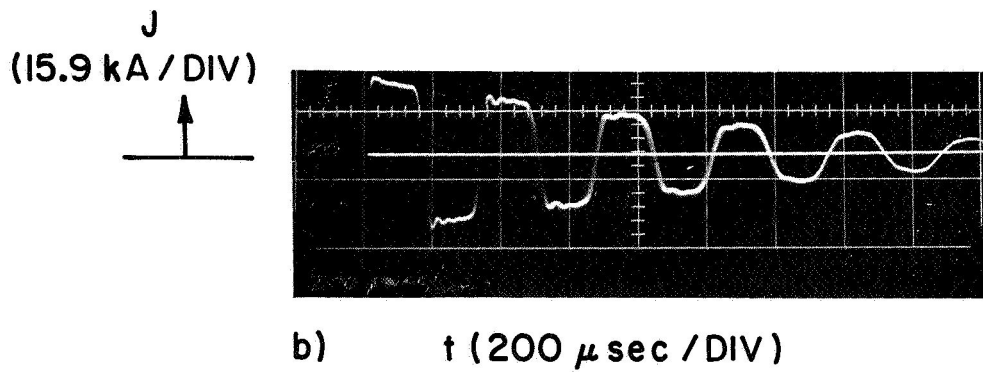
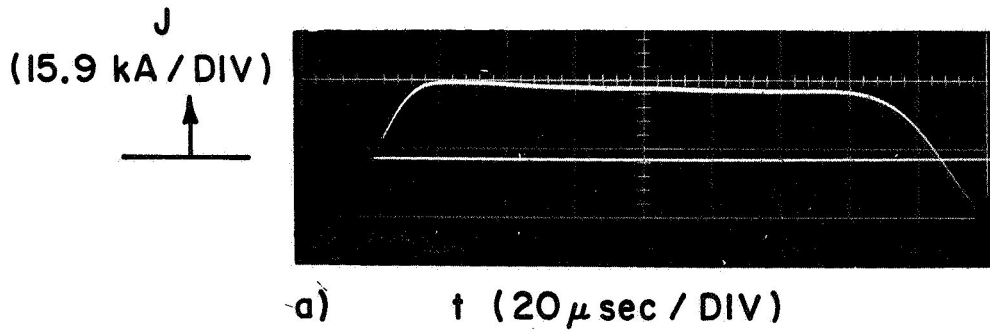


FIGURE 5-1



17.5 kA CURRENT PULSE ON TWO DIFFERENT
TIME SCALES

observed in Fig. 5-2a. In all cases, this time constant is adjusted to be ten times longer than the integration time of interest.

In Fig. 5-2b, this same 17.5 kA pulse is shown on a much longer time scale. The ringdown behavior observed in this figure is the characteristic pattern when the source impedance is much higher than the load impedance. Although only the first half-cycle of the current waveform is of interest in this experiment, this overall ringdown pattern reflects the poor energy transfer from bank to discharge typical of such an impedance mismatch. For the case shown, the load impedance is approximately 0.01Ω and the source impedance is 0.57Ω , so that the discharge represents nearly a short circuit to the power supply. In this situation, the pulse line performs as a fixed current source, independent of the discharge development; i.e., the mismatch provides the advantage of allowing a prescribed flat-top current pulse to be generated without the complication of the discharge dynamics distorting this current waveform. If the source and load impedances were comparable, the resulting nonlinear interaction between the power source and discharge dynamics would necessitate extensive circuit complication in order to realize a desired current waveform. This latter topic, including the effect of various source-to-load impedance ratios, has been studied in detail by other experimenters [72,73].

II. MASS INJECTION SYSTEM

With stabilization of the current conduction pattern on an appropriately short time scale clearly demonstrated for both ambient prefill and injected gas modes of operation, the principle problem remaining is the design of a gas handling system to satisfy the previously enumerated requirements on mass flow and time scale.

A. Early Systems

The results of fast ionization gauge measurements with the early shock tube injector shown in Fig. 3-6 can be used to assign limiting values to some of the characteristic times. These measurements indicate that the cold gas pressure profile propagates both radially and axially at the approximate rate of 6 in./msec.¹ In order that the environmental tank wall does not interfere with the natural development of the exhaust plume, the first half-cycle of the bank ringdown should be completed before the gas front can propagate to the wall. For the large plexiglas tank,

¹The millisecond time scale of this and other gasdynamic processes involved in the accelerator is in sharp contrast to the microsecond time scale characteristic of the plasma-dynamic events. This distinction will be shown to be especially important in connection with the synchronization of discharge current and mass injection pulses.

this limiting time is 3 msec. Since the longest available flat-top current pulse at present is approximately 600 μ sec, it follows that the longest acceptable delay time between gas injection and current initiation, τ_D , is 2.4 msec. From the definitions of the various delay times, this implies that the sum of the mass flow rise time, τ_R , and the subsequent chamber pressure stabilizing time, τ_A , be at most 2.4 msec. If the sum of τ_R and τ_A can be made less than 2.4 msec, then τ_D should be decreased also and not kept at its maximum allowable value. In this way, the minimum amount of neutral gas will be admitted to the tank before triggering the capacitor bank.

The shortcomings of electromagnetic valves in fulfilling the above requirements have already been discussed. In particular, long rise time and steadily decaying reservoir pressure render these unacceptable for a long-pulse mass injector.

The most effective means of satisfying the requirements for abrupt initiation of a constant mass flow rate has been shown to be a shock wave. Specifically, it is possible to utilize the pressure reservoir behind the head-on reflection of a shock wave from the end wall of a shock tube to drive gas through injection ports in the end wall at some constant rate [74]. The duration of this constant mass flow rate is usually limited by the arrival at the end wall of the wave resulting from the interaction of the

reflected shock with the contact surface. It should be noted, however, that the constant mass flow time characteristic of the continuum gas flow rapidly decreases if the initial pressure in the driven section is continuously lowered due to the formation of a highly diffuse initial shock wave. Figure 5-3 shows the x-t diagram for an ideal, continuum gas in a one-dimensional shock tube. The driver and driven gas are assumed to be the same and initially at equal temperatures. The figure shows the conventional division of gasdynamic regions by number, and subsequent numerical subscripts refer to these flow regimes. Region 5 is the reservoir of high pressure, high temperature gas, processed by both the incident and reflected shock waves, which can be used to provide an inflow to the discharge chamber.

It should be recalled, however, that neutral density measurements performed on the gas pulse produced by the early shock tube configuration revealed no steady pressure phase occurring in the electrode region. Instead, the profile rose steadily through the pressure range of interest. In part, this effect can be attributed to the diffuse wave structure associated with the low initial pressure in the driven section, the latter allowing mean free paths larger than the tube dimensions. In addition, the long, small diameter connecting lines from the shock tube to the arc chamber introduced a strong viscous effect which attenuated and

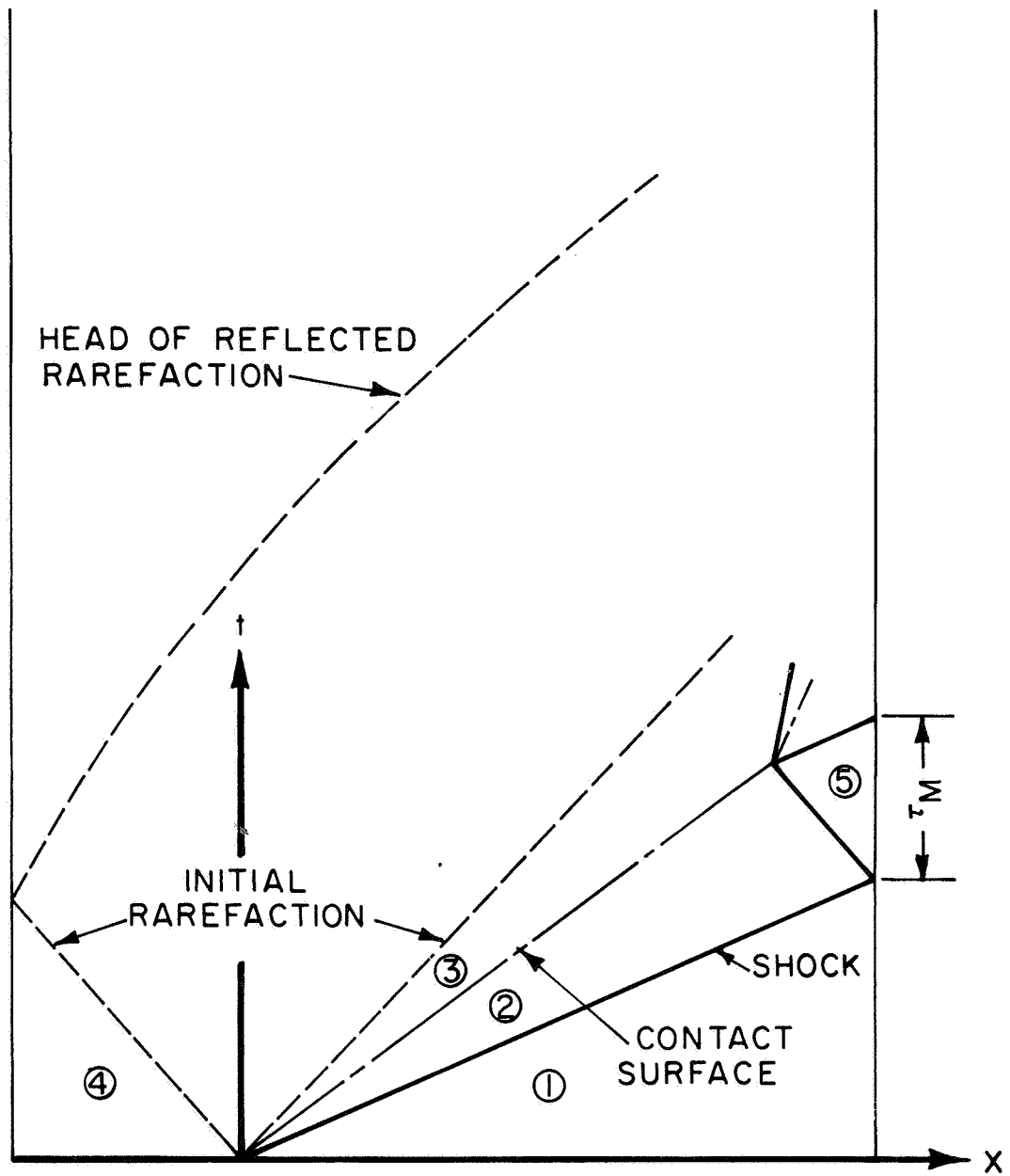


FIGURE 5-3

diffused any distinct propagating pressure profile. The combined effect of these two factors was the observed monotonically increasing pressure history.

B. System Modification

Two possibilities were considered for modifying the initial shock tube configuration to achieve the desired mass injection characteristics. The first of these makes use of a shock tube whose initial driven section pressure p , is maintained at a continuum level, about 1 torr. In order to do this without setting the same pressure throughout the entire system, the injection holes between the shock tube and the discharge chamber must be kept small. The speed of the 6-in. diffusion pump would then be sufficient to maintain a simulated space environment in the discharge chamber and exhaust tank. This technique has the advantages of a short mass flow rise time since the shock wave will be thin and well defined, and is simpler to implement technically because it does not require an external switch in the discharge circuit. However, it has the disadvantages that the extremely low back pressure capability of the facility will be sacrificed due to the leakage flow, and that it cannot provide the large mass flow levels desired for quasi-steady operation at high currents because the injection ports must be kept very small.

The alternate approach is to pump out completely the

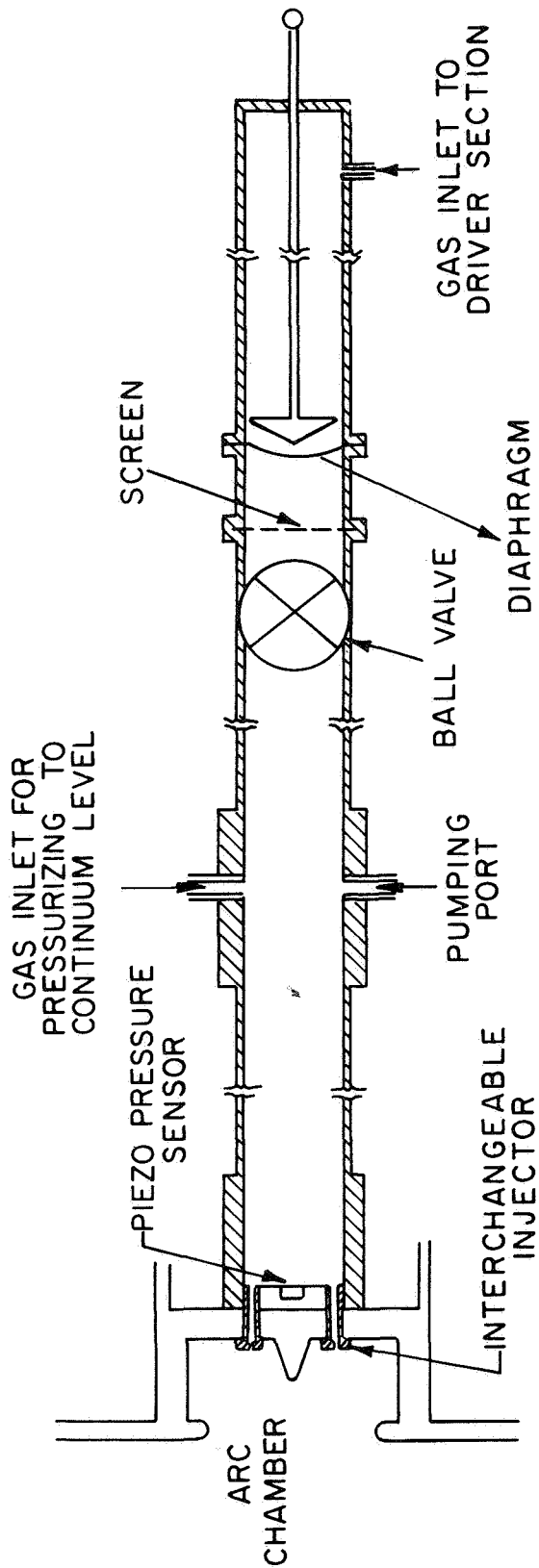
driven section as was done before and allow the pressure pulse to propagate into an ambient vacuum. Such a system will have the advantage of an improved space simulation due to the low back pressure, and because the injection hole diameter is not constrained to be small by leakage flow considerations, a broader range of mass flow rate is accessible. The disadvantages are longer mass flow rise time and the consequent need for a separate switch to delay the discharge until the flow reaches a steady level. Addition of a switch to the discharge circuit considerably complicates the design and operation of the facility because of the requirement for precise mass and current pulse synchronization.

Because of the technical simplification of avoiding a switch, and with the hope that the gasdynamic disadvantages would not be overriding, the continuum shock tube approach was selected for the first attempt. The tube consisted of a 2.37-in. diameter by 7.5-ft long plexiglas driven section and a 2.37-in. diameter by 2.0-ft long aluminum driver section. The diameter was selected such that the anticipated flow rates would not deplete the pressure in the reservoir of processed gas by more than 2 percent. The length of the driven section was chosen to provide a constant mass flow rate for at least 1 msec, based on ideal shock tube calculations. The length of the driver section is unimportant in this application since the rarefaction

propagates too slowly to participate in establishing the reservoir conditions. The driven section end cap contained six 0.31-in. diameter holes equally spaced on a 2-in. circle. By mounting the shock tube directly behind and coaxial with the cathode, the six connection lines between these holes and the 0.030-in. diameter injection orifices at the discharge chamber could be reduced to 0.75-in. lengths. Thus, any constant reservoir conditions resulting from this operation could be transmitted to the discharge chamber with negligible distortion.

With a 35 psia driver pressure, the diaphragm material found best was a 3-mil soft-tempered aluminum foil. This foil was tested to withstand a maximum pressure differential of 38 psi. Thus, when the driver was pressurized to 35 psia and the foil mechanically ruptured, a repeatable, clean petalling of the diaphragm was produced. Although soft-tempered foils normally did not shatter, a coarse mesh screen was installed 4 in. downstream of the diaphragm to prevent accidental plugging of the injection orifices. A 2.25-in. diameter ball valve was also installed immediately downstream of the screen to allow diaphragm changes without venting the large vacuum tank. A schematic of the complete shock tube assembly is shown in Fig. 5-4.

Extensive testing with this system showed that it was inadequate for two reasons. First, the discharge chamber pressure during the constant mass flow phase of the injected



SCHEMATIC DIAGRAM OF "CONTINUUM" SHOCK TUBE MASS INJECTION SYSTEM

FIGURE 5-4

pulse was too low for self-triggering to occur, i.e., when self-triggering occurred ($\tau_D \approx 2$ msec), the constant mass flow plateau of the injected mass pulse had already passed ($\tau_R \approx 2$ μ sec and $\tau_M \approx 500$ μ sec). If p_Y and the diameter of the injection holes were increased to raise the reservoir and chamber pressures and thereby decrease the delay time, the back pressure also increased due to the leakage flow, further compromising the space simulation. Second, even this delay time was found to be irreproducible to ± 1 msec, whereas the tolerable error based on known values of τ_M and τ_I was ± 0.1 msec. This irreproducibility was felt to be due to the sensitive dependence of the self-triggering discharge initiation process on the Paschen breakdown pressure for this particular electrode geometry. The compounding of these two additional problems with the anticipated disadvantages of low mass flow rates and increased back pressures completely precluded further utility of this system.

One useful result derived from this first shock tube configuration was the establishment of the characteristic time for the discharge chamber pressure to adjust to a new flow rate in response to a change in reservoir pressure. Using the same ionization gauge, placed at the anode orifice, τ_A was found to be 300 μ sec, a value applicable to the final gas injection system since the chamber geometry remained the same.

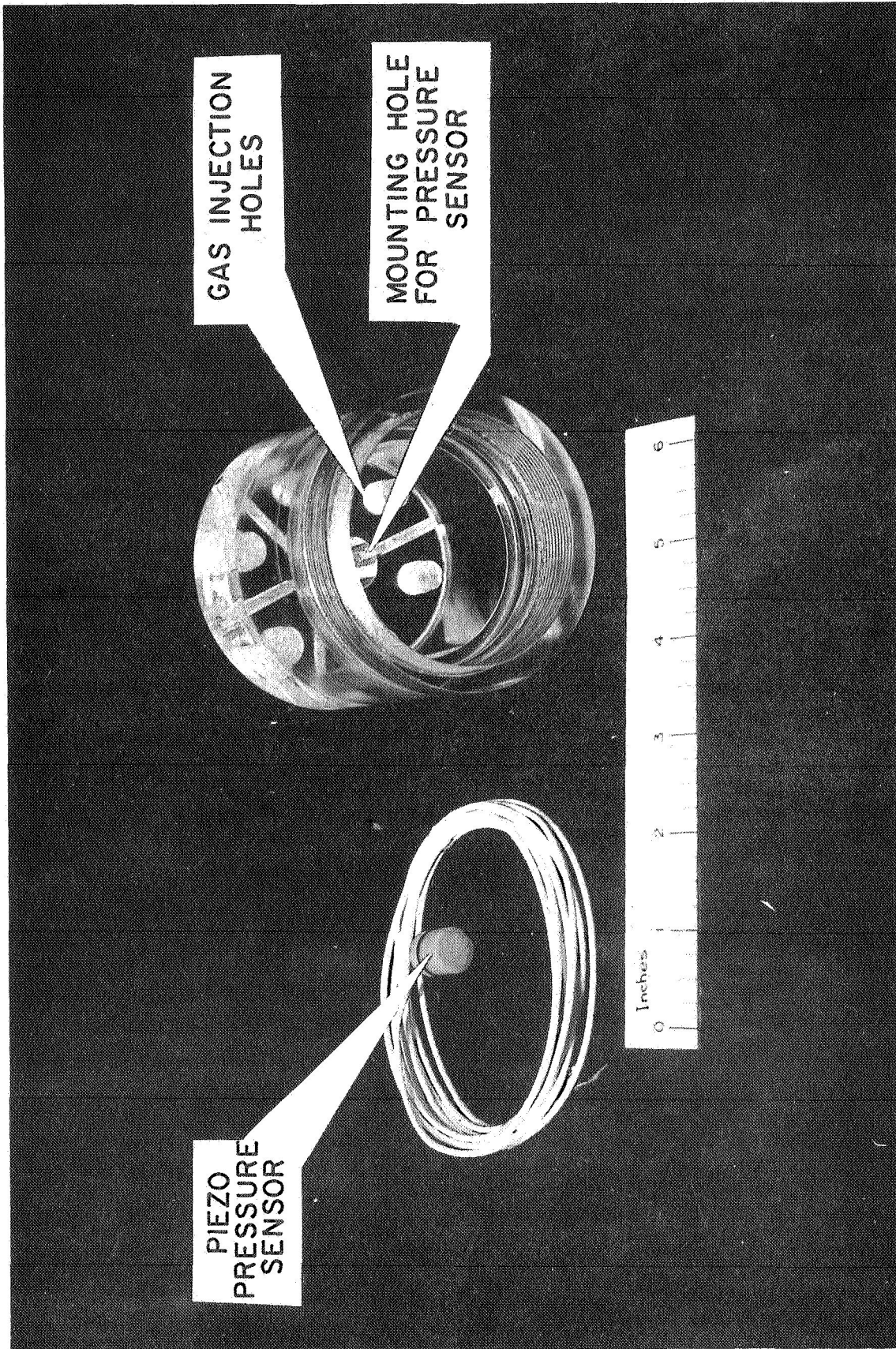
C. Final Configuration

With the "continuum" mode of shock tube injection shown to possess delay time problems as well as a fundamental inability to satisfy the mass flow requirements, the somewhat more cumbersome, but basically more versatile switch triggered mode of the second shock tube class discussed above was undertaken. In this case, the switch is necessary because the larger mass flow rates from this system produce chamber pressures well above the breakdown limit before a steady flow rate can be reached. Since the use of such a switch in previous experiments has provided a dependable and reproducible operation, its proper implementation should also eliminate the delay time irreproducibility found in the self-triggered mode.

The shock tube used for this mass injection configuration was the same basic unit used for the continuum system (see Fig. 5-4), although the initial driven section pressure was four orders of magnitude lower. The only exceptions were the opening of the injection holes to pass a larger mass flow rate and the addition of the external switch. Because of space limitations imposed by the large diameter shock tube mounted directly behind the cathode, the switch was located external to the accelerator in series with the hot conductor from the capacitor bank. Both the switch and its function as the synchronizing unit between current and mass pulses are discussed in more detail later in this chapter.

The performance of this system, as well as the previous system, was evaluated by using an insulated piezocrystal pressure sensor mounted flush with the end wall of the shock tube driven section. This piezocrystal probe construction is based on the design innovations incorporated in Ref. 75 with dimensions of the PZT-5 sensing element of 0.25-in. diameter by 0.040-in. thickness. The overall probe assembly, of dimensions 0.5-in. diameter by 0.5-in. long, is shown in Fig. 5-5 along with the shock tube driven section end cap in which it is mounted. Using established relations for the output of a piezocrystal [75], the calibration factor for the probe and associated coaxial cable is found to be 2.0 volts/atm with a rise time of approximately 1 μ sec. Because of the input resistance of the oscilloscope ($1\text{ M}\Omega$), the probe has an RC decay time constant of 600 μ sec. In order to observe sustained pressure histories, this time constant was increased to several tens of milliseconds by connecting a large resistor in series with the pressure sensing circuit.

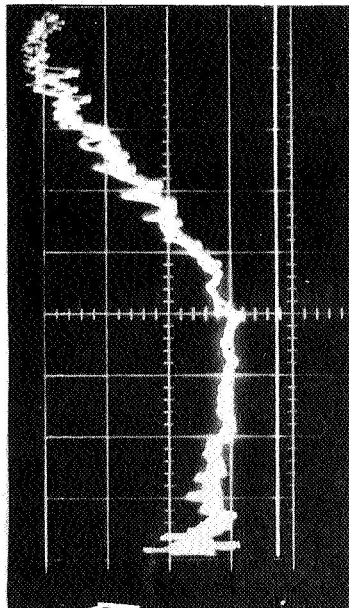
For very low initial pressures, the incident shock becomes very diffuse, and the early pressure history on the end wall has no constant phase like the "continuum" case. It is thus necessary to make use of an entirely different portion of the pressure response curve from that which was used in the first system. To illustrate the change, Fig. 5-6a shows a typical triple overlay of the piezo probe response to the pressure on the shock tube end wall for the "continuum" mass injection system with $p_1 = 1$ torr and a diameter of the



PIEZO PRESSURE SENSOR WITH PLEXIGLAS SHOCK TUBE
END CAP

FIGURE 5 - 5

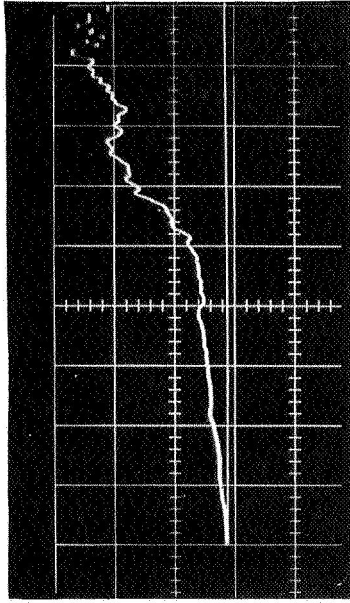
CONTINUUM SHOCK TUBE
 $P_i = 1 \text{ torr}$



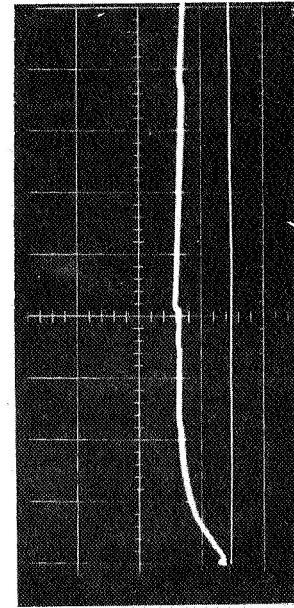
P
(0.03 atm / DIV)

a) t (100 μ sec / DIV)

VACUUM SHOCK TUBE
 $P_i \approx 10^{-4} \text{ torr}$

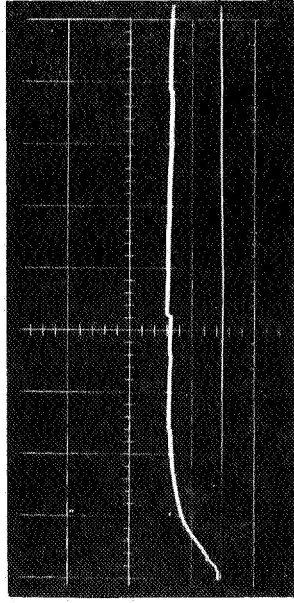


c) t (100 μ sec / DIV)



P
(3.0 atm / DIV)

b) t (5 msec / DIV)

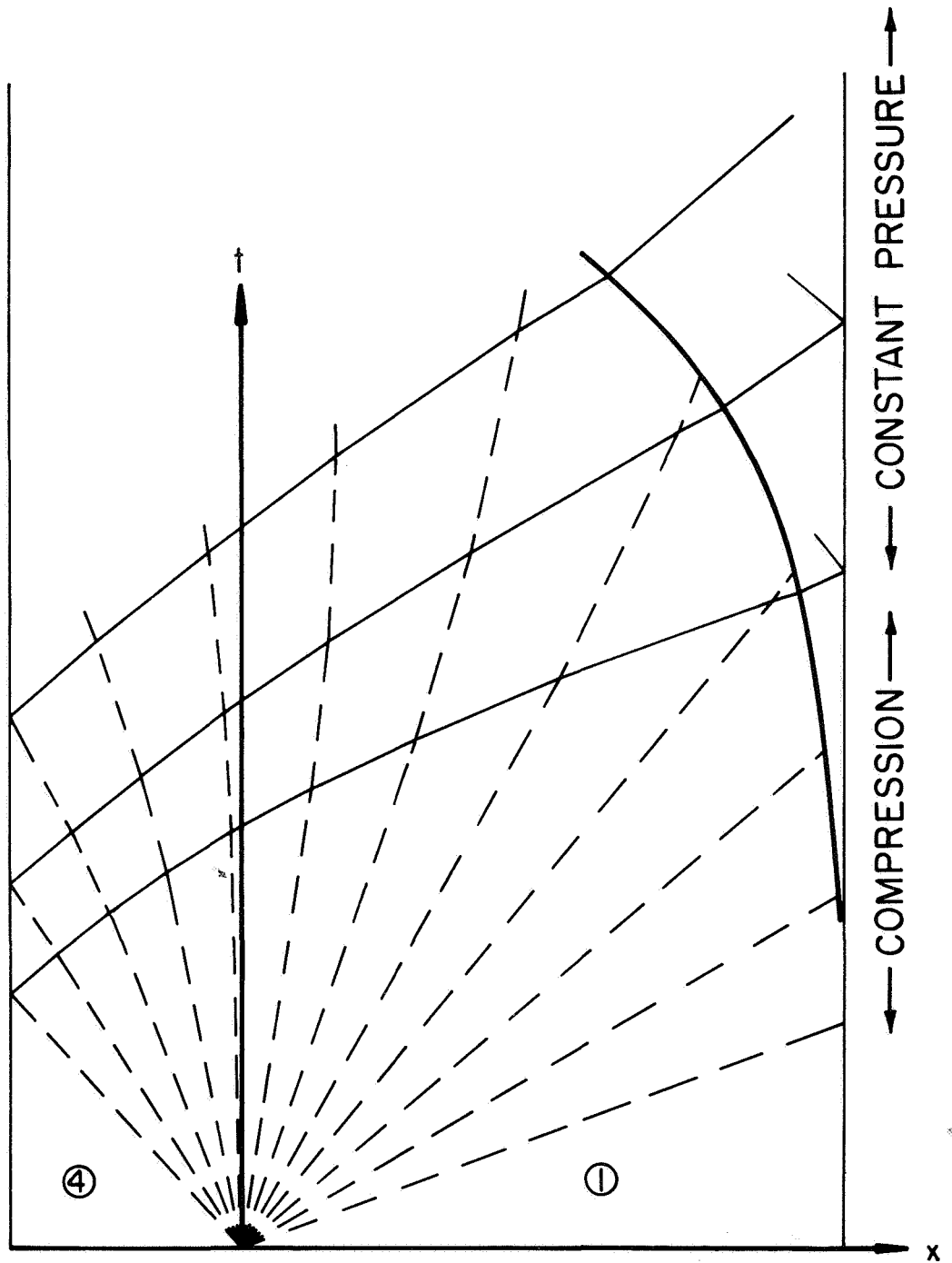


d) t (5 msec / DIV)

PIEZOELECTRIC PRESSURE RECORDS AT END OF SHOCK TUBE

injection holes of 0.030 inches. It is seen that there is a rapid rise ($\tau_R \approx 2 \mu\text{sec}$) to a pressure plateau which lasts for approximately 500 μsec . The magnitude of this reservoir pressure plateau is 20-40 torr, depending on the value of p_1 . Figure 5-6b shows the piezocrystal response for the same shock tube conditions, but on a greatly compressed time scale (series resistance = 80 $M\Omega$). Note that the total time depicted in Fig. 5-6a now occupies only 2 mm (one small division) on this photograph and that the pressure level after 10 msec is nearly constant at a value more than an order of magnitude greater than the earlier plateau shown in Fig. 5-6a. The initial shock wave bounces back and forth in the tube, with subsequent reflections off the driven section end wall registered by the piezo gauge as discrete pressure jumps at 21 msec and 39 msec as shown in Fig. 5-6b.

Referring to Fig. 5-3, it is apparent that the gradual compression observed in Fig. 5-6b after 1 msec is due to the arrival of the tail of the initial rarefaction which, in the laboratory frame, convects downstream for a sufficiently large initial pressure ratio across the diaphragm. When the reflection of the rarefaction head off the driver end wall reaches the driven section end wall, calculated to occur at approximately 7.4 msec, its superposition with the initial rarefaction tail contribution produces a region of essentially constant reservoir pressure. This effect is shown more clearly in Fig. 5-7 which displays a similar x-t diagram for the case of p_1 approaching zero. Note that because of the supersonic velocity of the gas arriving at the driven section end of the tube, no waves are reflected until a sufficiently strong



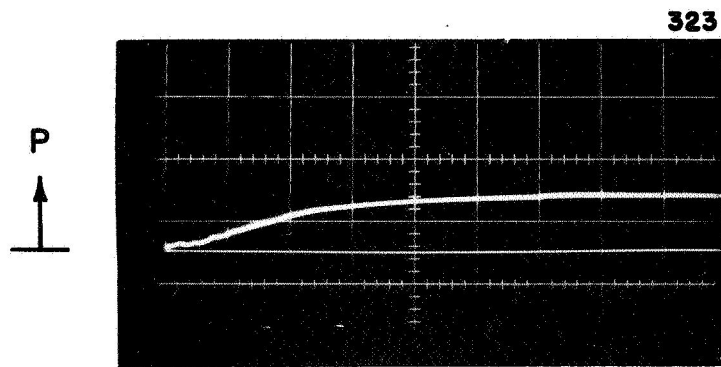
SHOCK TUBE $X-t$ DIAGRAM FOR $P_1 \rightarrow 0$

shock wave is assembled. Figures 5-3 and 5-7 show that while the early pressure history at the driven section end wall ($t \lesssim 1$ msec) is governed by the initial shock wave and its various interactions with the end wall and contact surface, the later pressure history ($t \gtrsim 2$ msec) is governed by the initial and reflected rarefaction waves.

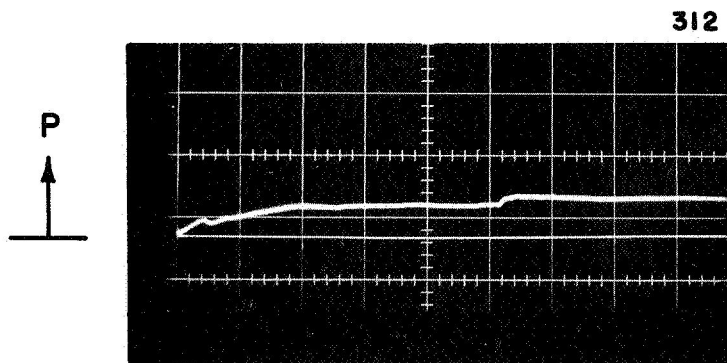
Turning now to the second shock tube scheme ($p_1 \approx 0$), it is reasonable to expect that for very low initial pressures in the driven section (where the mean free path exceeds tube dimensions), the initial pressure history on the endwall will be substantially different since the incident "shock wave" will be quite diffuse. The later portions of the long time profile, however, should appear essentially the same. Figure 5-6c shows the piezo gauge response for the same tube geometry as described for the "continuum" injector, but with p_1 now lowered to 10^{-4} torr and the diameter of the injection holes increased from 0.030 in. to 0.063 inches. Note that no serviceable uniform phase such as seen in Fig. 5-6a is available here. However, on the longer time base (Fig. 5-6d) it is apparent that the portion of the response after the first millisecond is essentially identical to Fig. 5-6b. Thus, by evacuating the driven section to a low pressure comparable to that in the environmental tank, the injection holes can be opened up to pass large mass flow rates and an adequately uniform high pressure reservoir can be produced late in the shock tube flow.

The rise time to the pressure plateau in the previous figure was seen to be 10 msec, but on the basis of the cold gas profile propagation speed, the maximum tolerable value has been shown to be $2.4 \text{ msec} - \tau_A = 2.1 \text{ msec}$. Since the on-

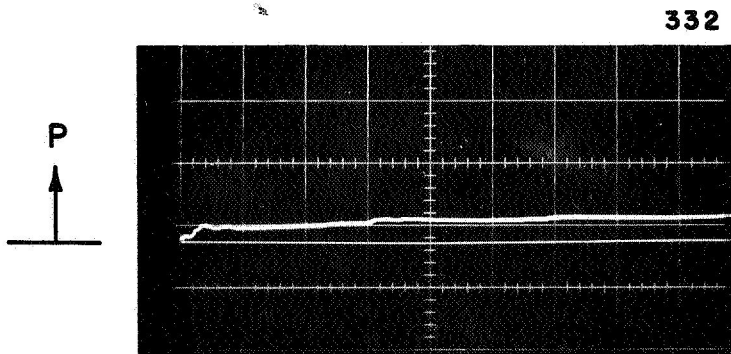
set of this plateau is due to the reflected rarefaction arriving at the downstream end of the shock tube, shortening the driven and driver sections should reduce the prohibitively long τ_R value. Figure 5-8 shows the effects of such changes. In Fig. 5-8a, the piezocrystal response for this second shock tube configuration is shown (driven section length $\equiv L_1 = 7.5$ ft., driver section length $\equiv L_4 = 2.0$ ft., and initial driven section pressure $\equiv p_1 \approx 10^{-4}$ torr). Note that this is just Fig. 5-6d seen on an expanded time scale. Figure 5-8b shows the effect of shortening the driven section from 7.5 ft. to 2.5 ft. while retaining the original driver section. The rise time to a pressure plateau has decreased from 10 msec down to 4 msec at the expense of decreasing the plateau level by approximately 50 percent. It is reasonable to expect that shorter driven sections would produce further decreases in the mass flow rise time. However, the 2.5 ft. length is the minimum length which allows installation directly behind the cathode with the large vacuum tank. On the same time and voltage scales, Fig. 5-8c shows the effect of retaining the 2.5 ft. shortened driven section while decreasing the driver section length from 2.0 ft. to 0.5 ft. As expected, the rise time to a plateau has been further reduced accompanied by an additional plateau magnitude reduction. Figure 5-9a shows this last trace on amplified voltage and time scales and in a negative direction. It is apparent that the reflected rarefaction arrives after approximately 1 msec with the plateau then being constant to within 10 percent for at least an additional 3 msec.



a) $L_1 = 7.5 \text{ ft}; L_4 = 2.0 \text{ ft}$



b) $L_1 = 2.5 \text{ ft}; L_4 = 2.0 \text{ ft}$

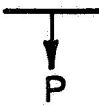


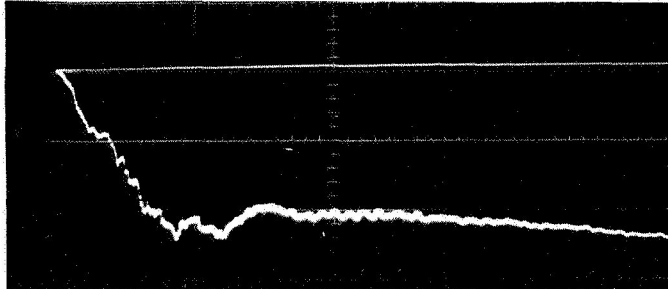
c) $L_1 = 2.5 \text{ ft}; L_4 = 0.5 \text{ ft}$

EFFECTS OF DRIVEN AND DRIVER SECTION LENGTHS
ON PRESSURE HISTORY AT END OF SHOCK TUBE

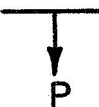
$P_1 \approx 10^{-4} \text{ torr}; 2 \text{ msec} / \text{DIV}$

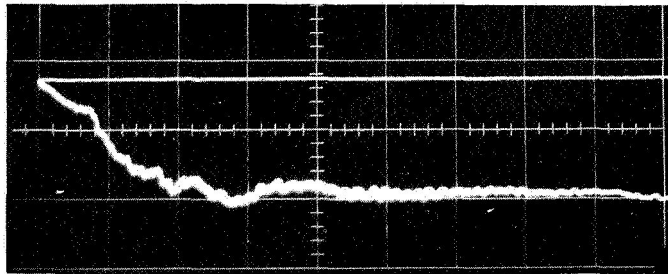
FIGURE 5-8


 (0.3 atm / DIV)



a) $D_4 = 2.37 \text{ in.}; 500 \mu\text{sec}/\text{DIV}$


 (0.6 atm / DIV)



b) $D = 4.75 \text{ in.}; 500 \mu\text{sec} / \text{DIV}$

EFFECT OF DRIVER SECTION DIAMETER
ON PRESSURE HISTORY AT END OF SHOCK TUBE

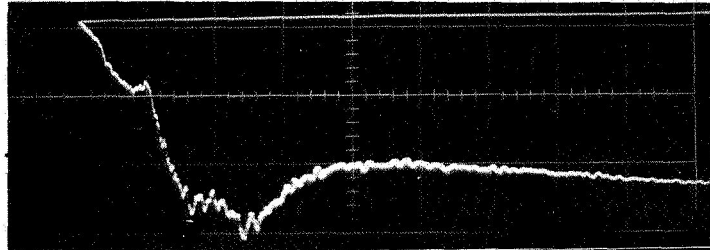
$$L_1 = 2.5 \text{ ft}; L_4 = 0.5 \text{ ft}; P_1 \approx 10^{-4} \text{ torr}$$

FIGURE 5-9

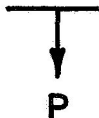
The loss of plateau pressure caused by shortening the driven and driver section lengths can be offset by increasing the driver diameter. Figure 5-9b shows the effect of doubling this diameter but keeping the length the same in order not to change the arrival time of the reflected rarefaction. Note that the plateau is approximately 50 percent greater with this increased diameter but the mass flow rise time does not change. Further driver section diameter increases were not attempted due to stress limitations in the plexiglas driven section.

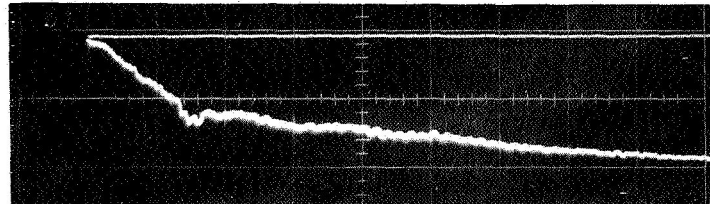
A secondary problem of this mode of shock tube injection is a slight overshoot in the reservoir pressure as shown in Fig. 5-10a. To eliminate this overshoot, a small copper disc was mounted on the plunger used to rupture the diaphragm. The function of this disc is to provide a small reflected rarefaction which arrives at the driven section end wall slightly before the principle reflected rarefaction arrives from the driver end wall. Hence, varying the size and location of the disc on the plunger provides a sensitive adjustment mechanism by which the knee of the reservoir pressure profile can be tailored. Figure 5-10b shows the effect of too large a disc (1.5-in. diameter) too close to the initial diaphragm location (1.5 in. back); locations too far from the diaphragm do not remove the overshoot. The profile for a 1-in. disc mounted 3 in. behind the diaphragm is shown in Fig. 5-10c. This is the profile used during all subsequent discharge data acquisition. A schematic of the final mass injection system is shown in Fig. 5-11.


 P
 (0.3 atm / DIV)



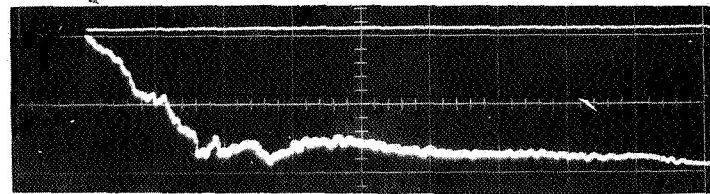
a) NO DISC $D_4 = 2.37$ in


 P
 (0.6 atm / DIV)



b) 1.5 in. DIA. DISC, 1.5 in. BACK
 $D_4 = 4.75$ in.


 P
 (0.6 atm / DIV)

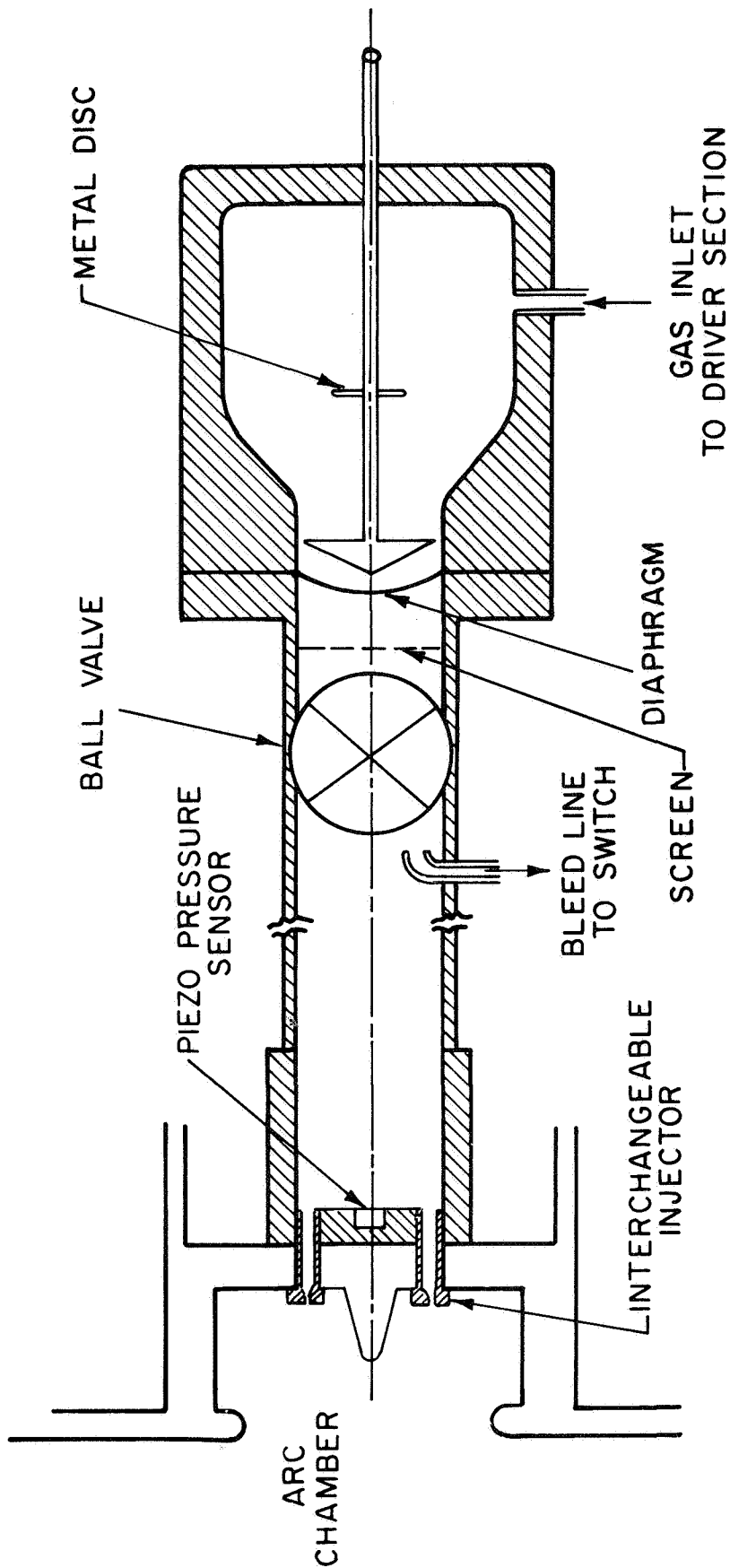


c) 1.0 in. DIA. DISC, 3.0 in. BACK
 $D_4 = 4.75$ in.

EFFECT OF VARIOUS DIAPHRAGM PLUNGER DISCS ON
 PRESSURE HISTORY AT END OF SHOCK TUBE

$L_1 = 2.5$ ft; $L_4 = 0.5$ ft; $500 \mu\text{sec} / \text{DIV}$

FIGURE 5-10



SCHEMATIC OF FINAL MASS INJECTION SYSTEM

FIGURE 5 - II

The calibrated piezocrystal yields the pressure level of the plateau which, when combined with the appropriate discharge coefficient and reservoir temperature, permits calculation of the mass flow rate into the arc chamber for a given injector hole size. The discharge coefficients were taken from Ref. [76] and reservoir temperatures were based on an isentropic expansion from the driver pressure to the measured reservoir value. In accordance with the previously measured value of the discharge chamber pressure adjustment time, τ_A , 300 μ sec after this pressure plateau has been reached, the mass flow rate out of the discharge chamber will reach this same calculated value. Figure 5-12 shows the achievable mass flow rates for various injector sizes with pressure in the driver section as a parameter. Comparing this with Fig. 4-1, it is evident that from gasdynamic considerations, the present system is capable of supplying the appropriate mass flow rate for MPD simulation over the current range from 60 kA down to less than 1 kA, which well overlaps the steady state MPD arc domain. In addition, this mass injection system provides steady flow rates for times considerably longer than the longest current pulse available with the present capacitor bank and inductors. As such, it will remain serviceable when the simulation program is extended to the longer pulses which eventually will be required for investigation and evaluation of the long pulse mode of operation as an optimum pulsed plasma thruster technique.

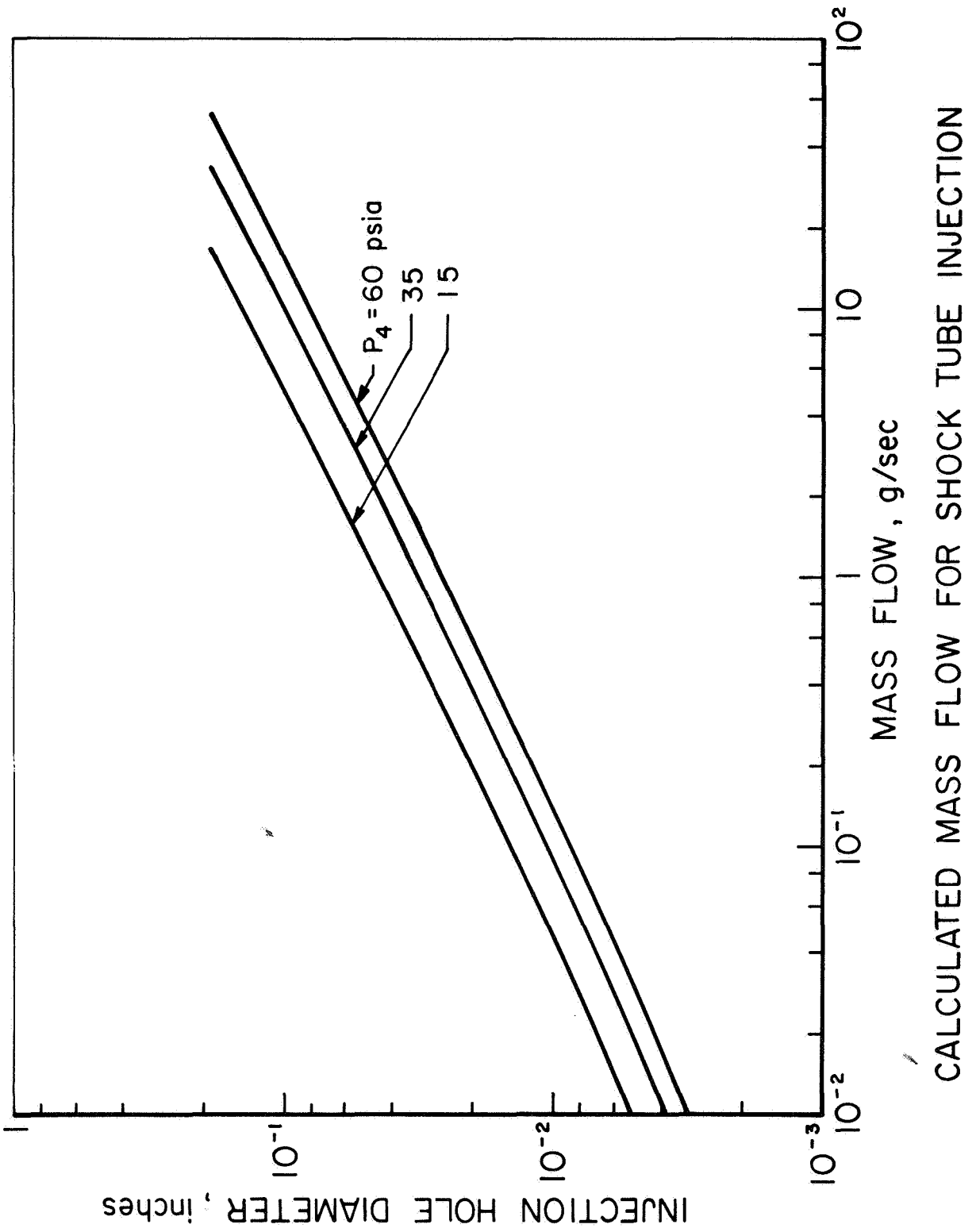
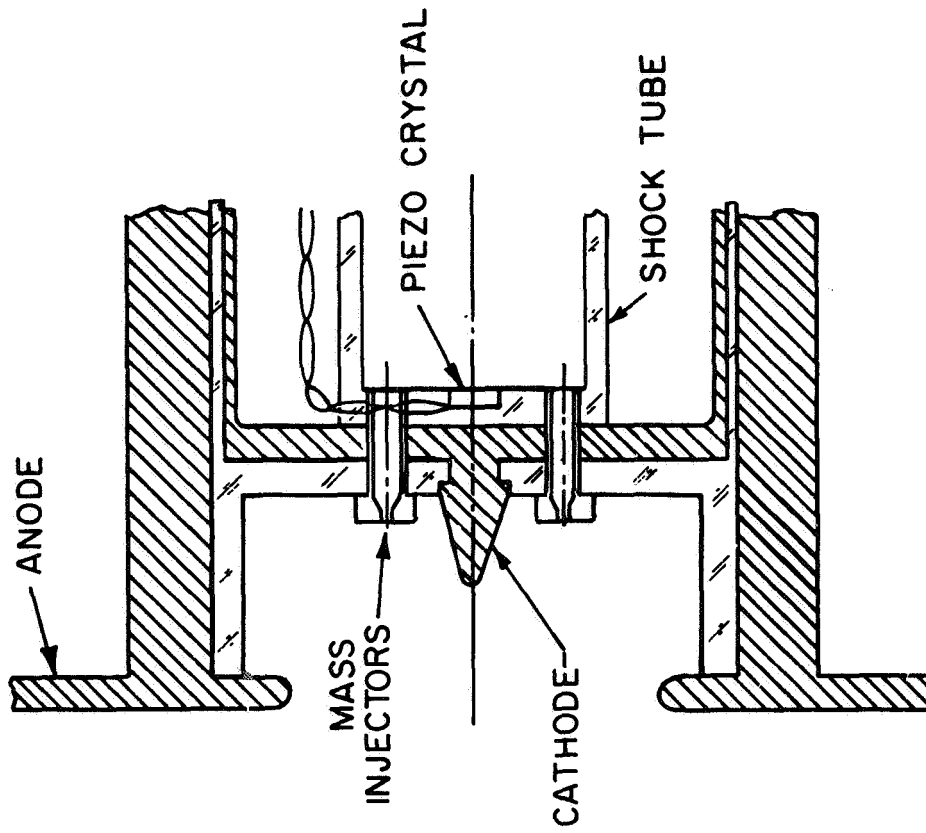


FIGURE 5 - 12

III. GEOMETRY

This new mass injection system was first tested with the flat cathode configuration used for the early exhaust experiments, described in Chap. 3, Sec. IV, with the difference that gas was injected through six ports in the cathode instead of through two ports in the chamber side walls. This difference in gas injection geometry could be significant since the injected mass is constrained to pass through only that fraction of the total current which terminates on the cathode at a radius less than the injection hole radius. Thus, the determination of the current distribution on the cathode provides some measure of the effectiveness with which the given geometry is accelerating the supplied mass. Magnetic probes showed that only about 5 percent of the current was participating in accelerating the injected mass with this configuration; the rest reached the cathode at radii exterior to the injection ports. In an attempt to improve this, a 0.75-in. diameter by 1.1-in. long, 2 percent thoriaated tungsten cone was affixed to the center of the cathode plate, but this was found to increase the participating current fraction to only 10 percent.

To force the desired discharge localization to cathode center, the aluminum cathode disc was covered by a Plexiglas disc, on which the cathode cone was mounted. Details of this configuration are sketched in Fig. 5-13, which also shows the shock tube-discharge chamber interface as well as the interchangeable mass injectors. A photograph of these components



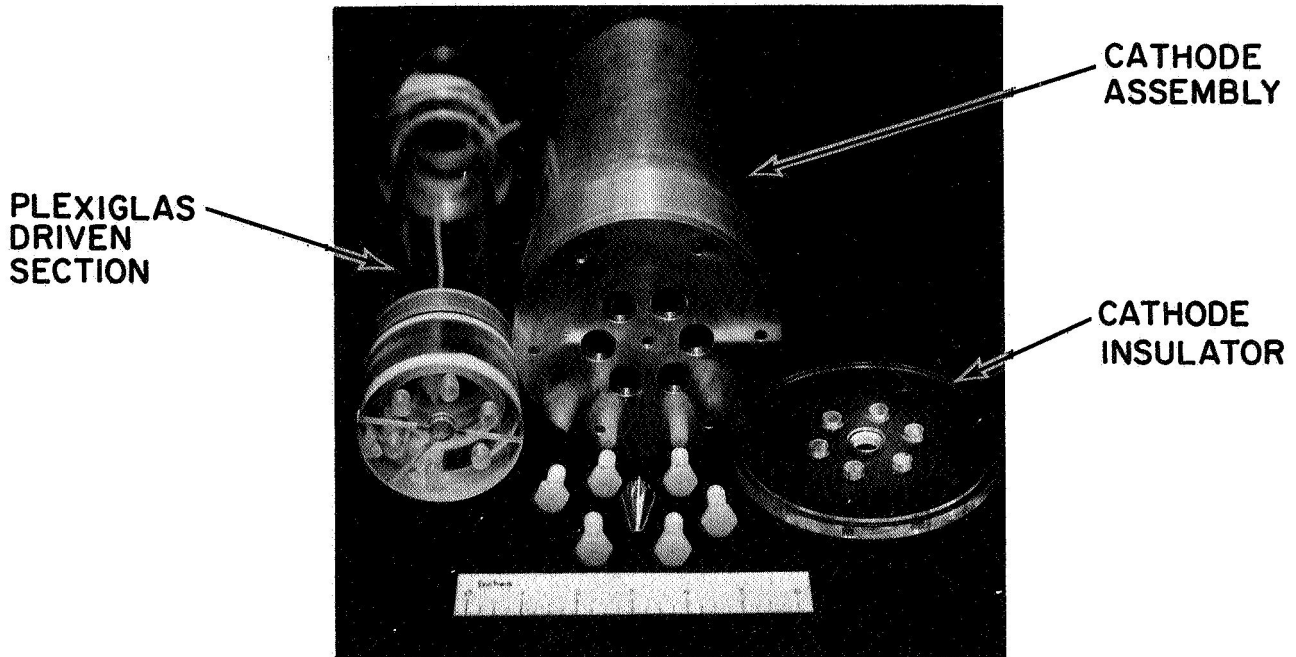
CROSS SECTION OF ACCELERATOR

FIGURE 5-13

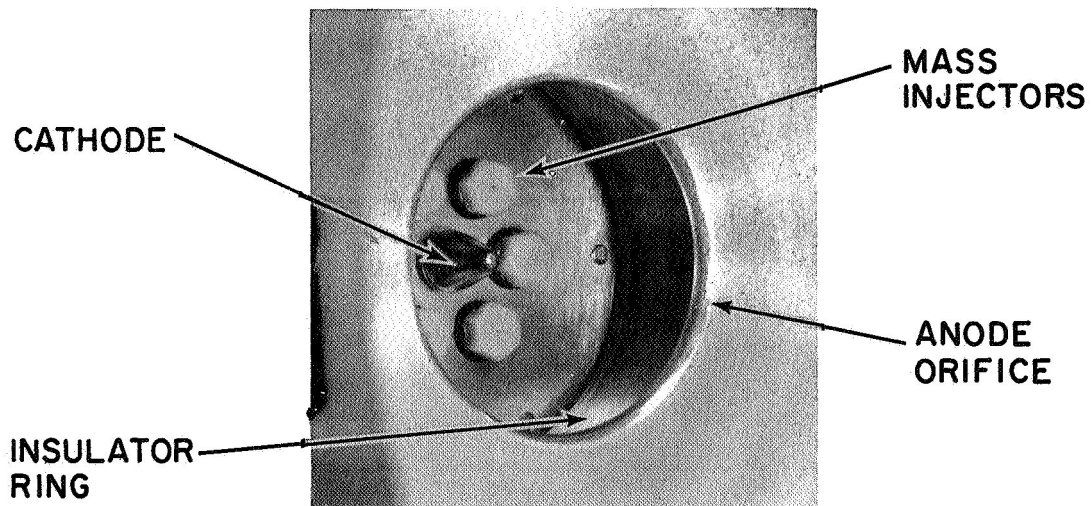
which comprise the cathode and mass injection assemblies are shown in Fig. 5-14a. The assembled discharge chamber, including the glass insulator ring and part of the anode face plate, are shown in the perspective view in Fig. 5-14b.

The size of the anode orifice can be established by various scaling arguments applied to pulsed and steady state accelerators. Since high thrust per unit exhaust area has been cited as an interesting feature of the steady state MPD arcjet, it is reasonable to require that the corresponding quasi-steady accelerator have a comparable value. For a purely electromagnetic thrust mode, the thrust scales with the square of the current, as has been stated previously. Thus, scaling thrust per unit exhaust area is the same as scaling the parameter J/D_a , where D_a is the diameter of the anode orifice. Since steady state operation is limited to operation below approximately 3000 A, and since the available quasi-steady mass flow rates limit pulsed operation to currents less than 60,000 A for an interesting range of specific impulse values, then to first order, the orifice diameter of the pulsed accelerator should be approximately 10 times that of the steady state device. For typical steady state configurations [77,42], this implies an orifice diameter of 5 in. or less in order to achieve at least a comparable thrust per unit exhaust area. By this scaling parameter, it appears that the 4-in. orifice employed in the early plasma exhaust experiments is suitable.

Alternatively, the size of the chamber orifice can also



a) EXPLODED VIEW



b) PERSPECTIVE VIEW OF ASSEMBLED CHAMBER

PHOTOGRAPHS OF SHOCK TUBE-CATHODE INTERFACE COMPONENTS

FIGURE 5-14

be prescribed by requiring the orifice mass flux in the steady and pulsed configurations to be similar. For the same steady state devices referenced above, the average orifice mass flux covers the range from $0.16 \text{ kg/m}^2\text{sec}$ to $1.95 \text{ kg/m}^2\text{sec}$. As shown in Fig. 4-1, the requirement of producing an interesting range of specific impulse values for the available current range of 4 to 140 kA implies the necessary mass throughput. (It should again be noted that these calculations are based on a prescribed value of the anode-to-cathode radius ratio. Since the cathode attachment radius is not necessarily equal to its geometric radius, the radius ratio value used in the calculations must be verified after the current conduction patterns have been measured. As stated previously, however, the calculations are not sensitive to this ratio due to the logarithmic dependence.) Again using the 4-in. orifice with the mass flow rates produced by the quasi-steady injection system indicates an average orifice mass flux of $0.10 \text{ kg/m}^2\text{sec}$ to $4.31 \text{ kg/m}^2\text{sec}$, a range which encompasses the corresponding steady state values. Thus, the 4-in. orifice also appears satisfactory when the average orifice mass flux is considered to be the scaling parameter.

Perhaps the most meaningful scaling, however, is provided by the magnetic interaction parameter, β , which is the ratio of the electromagnetic body force to the gasdynamic inertia. Of the various forms of this parameter which might be used [43], the most appropriate for this accelerator takes the form

$$\beta = \frac{\int (B^2/2\mu) dA}{\int (\rho u^2) dA} \quad \text{where the magnetic field, } B, \text{ the density, } \rho, \text{ and the velocity, } u, \text{ are local values.}$$

For an axisymmetric current distribution, the numerator takes the form

$$\frac{\mu J^2}{4\pi} \int_{r_c}^{r_a} \frac{dr}{r} = \frac{\mu J^2}{4\pi} \ln \frac{r_a}{r_c}, \quad \text{and the denominator reduces to}$$

$\dot{m} I_{sp} g$ for a fixed exhaust velocity $u = I_{sp} g$. It follows that a fixed value of the interaction parameter implies

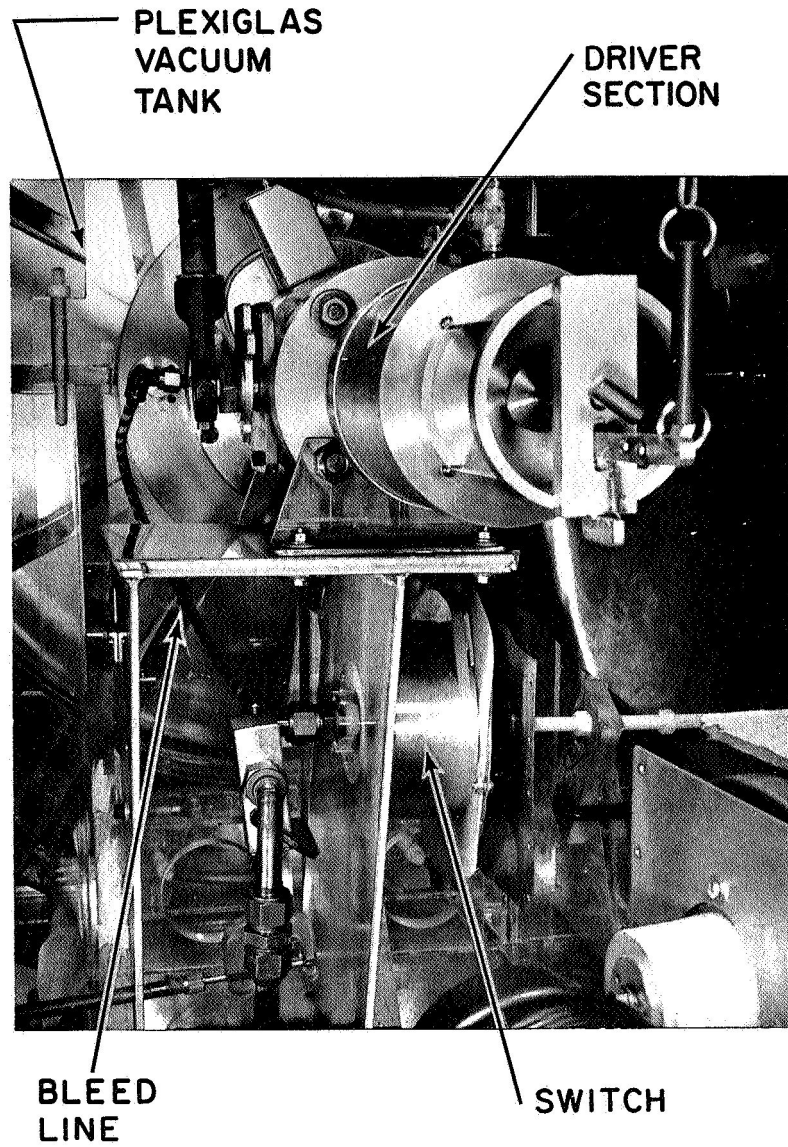
$$J^2 \ln \frac{r_a}{r_c} \propto \dot{m} I_{sp} g = T$$

Thus, for a fixed specific impulse, each of the scaling parameters invoked (thrust density and therefore power density, mass flux density, and the magnetic interaction parameter) reduces to a scaling of $\frac{J^2}{A} \ln \frac{r_a}{r_c}$. For approximately the same ratio of anode-to-cathode radii, the insensitive logarithmic term is not influential, and the absolute value of these radii should be scaled with the current. As already shown, this suggests that an anode orifice diameter of 4 in. is suitable for the extended current range available. Other than affixing this absolute dimension and the cathode modifications discussed earlier, no further effort was made to optimize the chamber geometry or electrode sizes, the anode retaining its 34-in. anode face diameter to allow free development of the exhaust plume.

The gas-triggered discharge switch necessary to delay the discharge initiation until the appropriate mass distribution is reached is identical to the 2-in. high by 5-in. diameter design shown in Figs. 3-3 and 3-6. However, space limitations behind the arc chamber caused by the large shock tube and small injector lengths have dictated that the switch not be coaxial with the discharge chamber but instead be mounted in series with the hot lead from the capacitor bank.

Synchronization of the current pulse with the mass pulse is accomplished by bleeding a small amount of gas from the shock tube into the switch through a 0.37-in. diameter nylon tube. The shock tube entrance to this line is in the form of a small scoop (0.37-in. diameter) protruding into the tube as shown in Fig. 5-11. Piezo measurements have shown no detectable change in the pressure history at the driven section end wall because of this small bleed flow. Figure 5-15 shows a photograph of the switch, shock tube, and bleed line arrangement at the back of the pulsed arc facility.

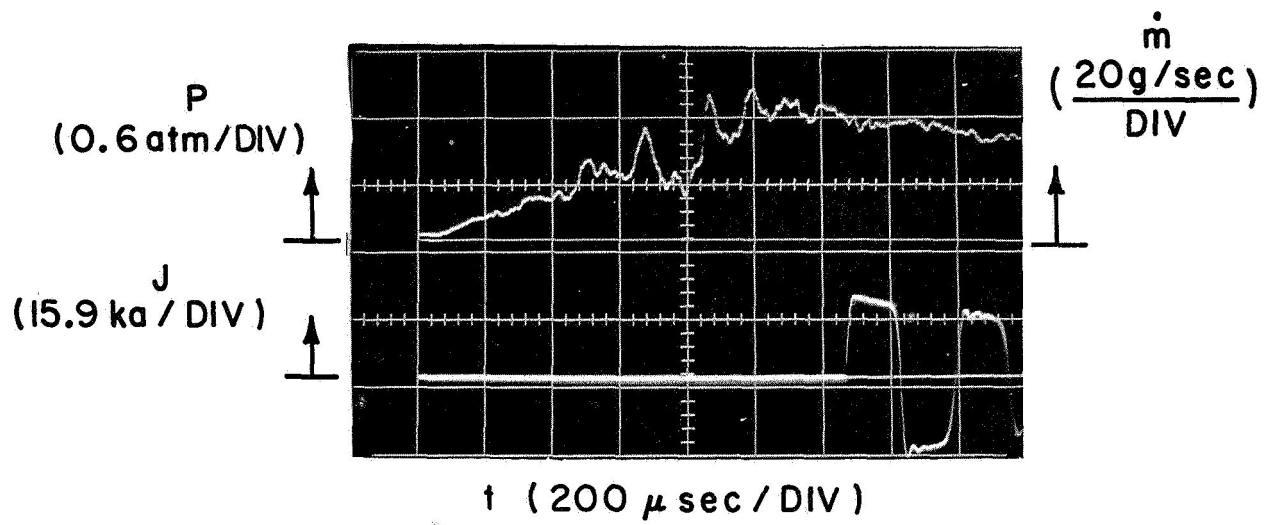
Recalling that the mass flow rise time to a steady value is 1 msec, as shown in Fig. 5-9, and that an additional 300 μ sec is necessary to allow the chamber pressure to adjust to this mass flow rate, then the required delay time, τ_D , is approximately 1.3 msec. By systematically varying the length of the bleed line from the shock tube to the switch, the desired delay time can be achieved. Figure 5-16 displays the reservoir pressure and total current to the chamber when the



PHOTOGRAPH OF MASS INJECTION SYSTEM AND GAS-TRIGGERED
SWITCH AT BACK OF FACILITY

AP 25 P-276 69

FIGURE 5-15



CURRENT PULSE SYNCHRONIZED TO INJECTED MASS PULSE

appropriate length is reached. (A second piezocrystal pressure probe with a specially protective insulation has been used in the shock tube when the capacitor bank is fired to prevent the probe circuit from participating in the discharge. The resulting stress oscillations in the probe body due to this insulation distort somewhat the pressure record as seen in the upper trace in this figure. However, the function of this crystal is only to give a time reference on the oscilloscope from which the delay time until discharge initiation can be accurately measured. The true pressure history on this and all shots is that shown in Fig. 5-9b.) It is seen from Fig. 5-16 that approximately 1.3 msec after the pressure wave reaches the end of the shock tube, current initiation occurs, the ringdown waveform reflecting the impedance mismatch discussed earlier. Thus, during the first half-cycle of the current waveform, both current and mass flow rate are steady in a discharge chamber geometry closely resembling the steady state MPD arc configurations, and the initial goals of developing a quasi-steady accelerator have been met.

CHAPTER 6

RESULTS I: TERMINAL MEASUREMENTS

I. INTRODUCTION

With the properly synchronized application of quasi-steady gas and current pulses assured, certain of the operating characteristics of the accelerator can now be studied. These can be broadly divided into terminal characteristics, e.g. current, mass flow rate, voltage, thrust, and specific impulse, and interior properties, such as current density distribution, chamber pressure, electric field pattern, etc. This chapter discusses terminal measurements; Chap. 7 deals with the interior diagnostics.

Of the terminal properties listed above, current and mass flow rate are controlled inputs. Measurement of thrust and specific impulse require extreme care and sophistication [79] and are not attempted in the scope of this thesis. The remaining terminal property, the discharge voltage, can be particularly instructive, however. The identification and magnitude of its various components, such as the $\vec{u} \times \vec{B}$ or "back EMF" acceleration term, and the resistive contribution, about which little is known for currents greater than 10^4 A, should indicate the efficiency of the electromagnetic acceleration throughout the operating range. In addition, the

functional dependence of voltage on current and mass flow rate should allow some discrimination among the several theoretical models of the acceleration process.

II. VOLTAGE DATA

In order to investigate the arc operation over a wide range of operating conditions, voltage measurements were recorded for flattop currents from 4.4 to 138 kA and for mass flow rates from 1.2 to 36.0 g/sec. Figure 6-1 shows the location of each data point on the map of required mass flow rate for a particular current and exhaust velocity as previously displayed in Fig. 4-1. These data were acquired by attaching a suitably compensated Tektronix P6013A voltage probe directly across the chamber electrodes. The signatures were displayed on a Tektronix Type 555 oscilloscope which was enclosed in a screen room at the downstream end of the vacuum tank away from the capacitor bank in order to minimize electromagnetic noise. To maintain the screen room ground at the same potential as the accelerator ground during the discharge, a 3-ft. wide by 15-ft. long copper ground plane connected the screen room to the anode ground. The voltage probe lead closely followed the ground plane to eliminate inductive pickup in the probe circuit. A complete schematic of the accelerator electrical circuit and the probe circuit is shown in Fig. 6-2. Note that a ballast resistor, R_B , is used to keep the cathode at ground potential while the switch is being

AP 43 X 7701-63

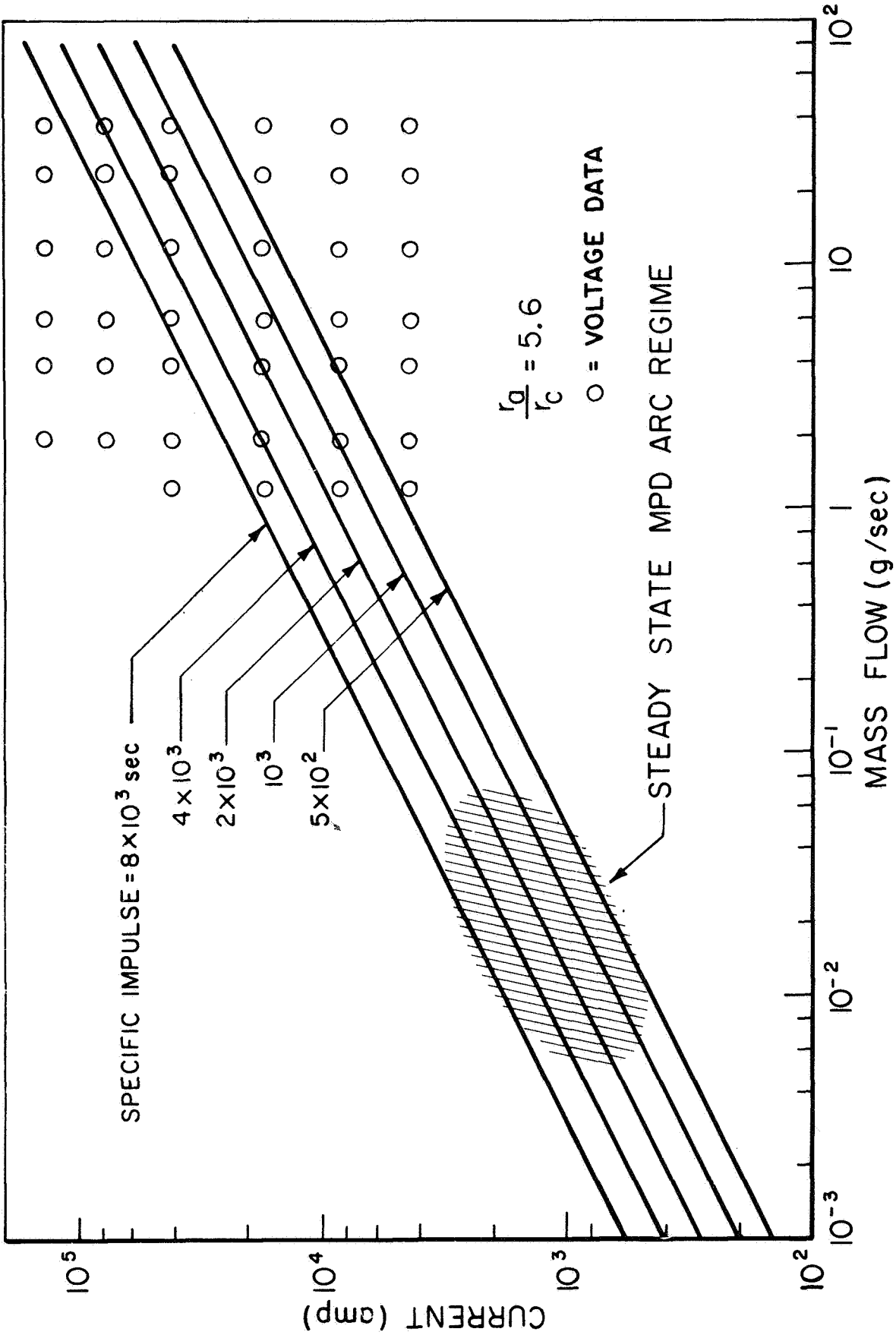
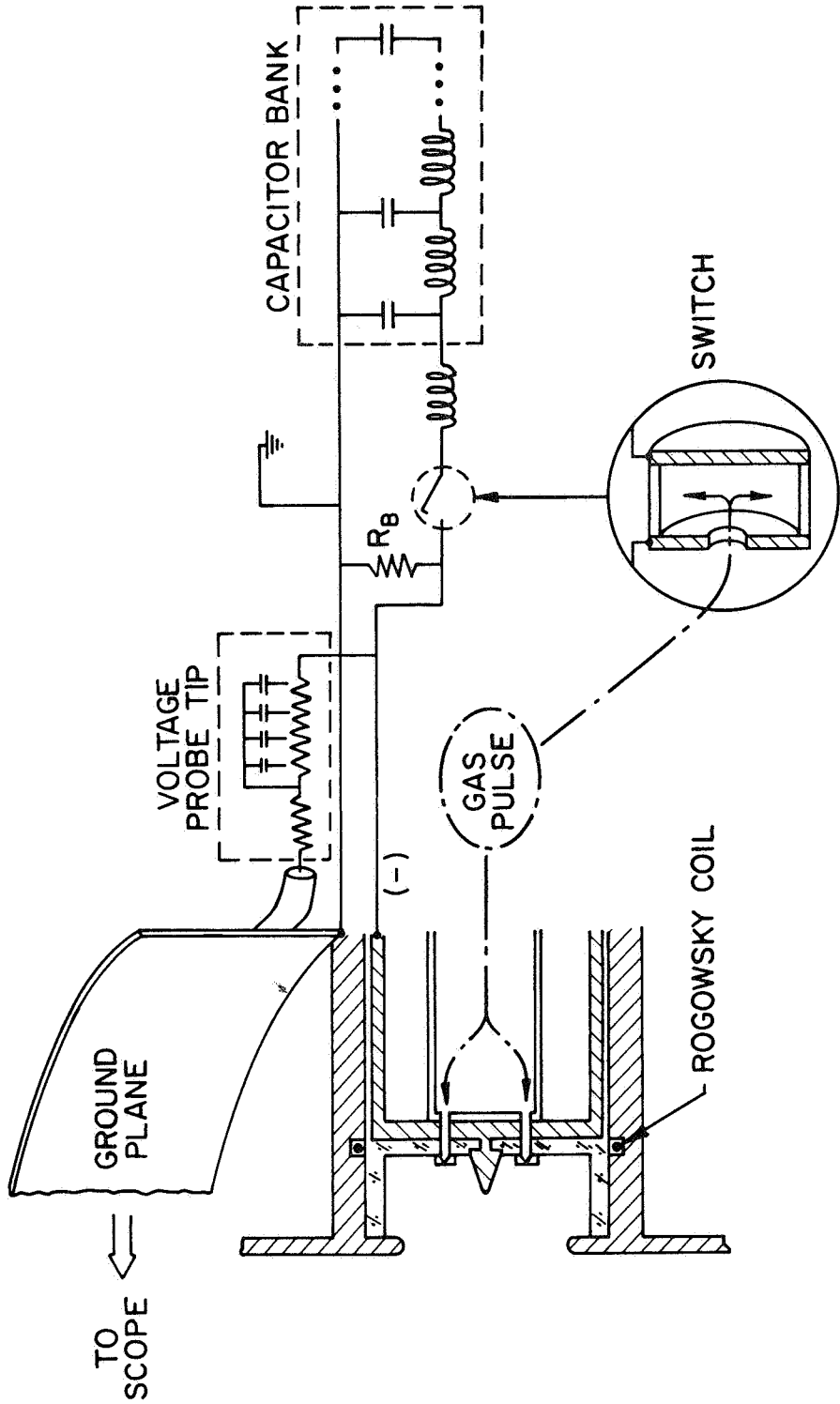


FIGURE 6-1

OPERATING CONDITIONS FOR TERMINAL VOLTAGE MEASUREMENTS



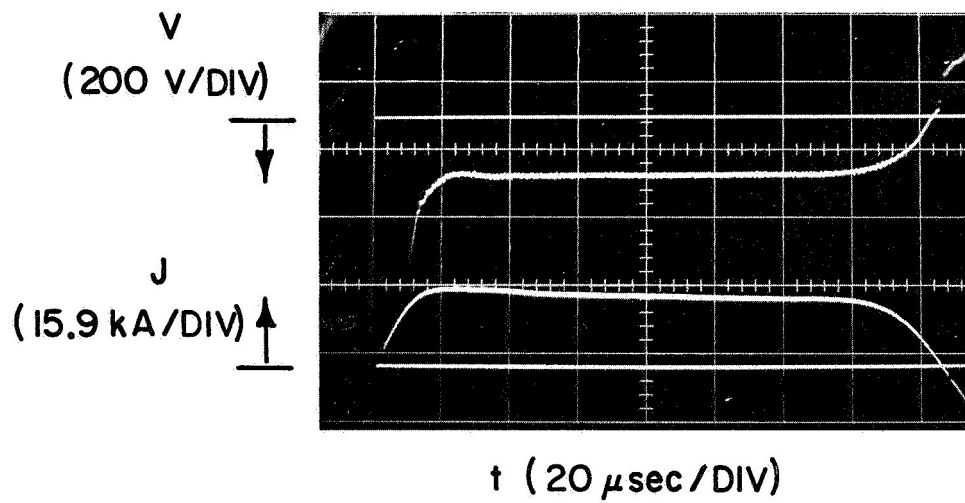
ACCELERATOR ELECTRICAL SCHEMATIC

FIGURE 6-2

charged to 10 kV. This resistor is sufficiently large-- 1000 Ω compared to the 0.01 Ω discharge impedance--so that virtually all of the current flows through the plasma after switch triggering.

The desired current waveforms were provided by the appropriate combination of interunit inductances and series-parallel connections within the capacitor bank. The mass flow rate was established by a given driver pressure and injection hole diameter. Fine scale variation of the mass flow rate was achieved by varying the shock tube driver pressure to avoid time consuming injector changes. Thus, the mass flow rate was varied over the quoted range by using only three different injector sets, of diameters 0.0355 in., 0.0625 in., and 0.152 in., and the three driver pressures shown in Fig. 5-12. Verification of this technique will be shown with the presented data.

Figure 6-3 displays a typical current and voltage history for the first half-cycle of a discharge properly synchronized to the mass pulse. The current level is 17.5 kA and the mass flow rate is 3.8 g/sec. The slight droop in the current is due to the time constant of the integrating circuit; larger time constants yield perfectly flat profiles, but have less sensitivity. The voltage, which is negative since it is the cathode potential relative to the anode ground, is seen to have a large spike initially, corresponding to the application of the full 10 kV bank voltage to the chamber by the switch.

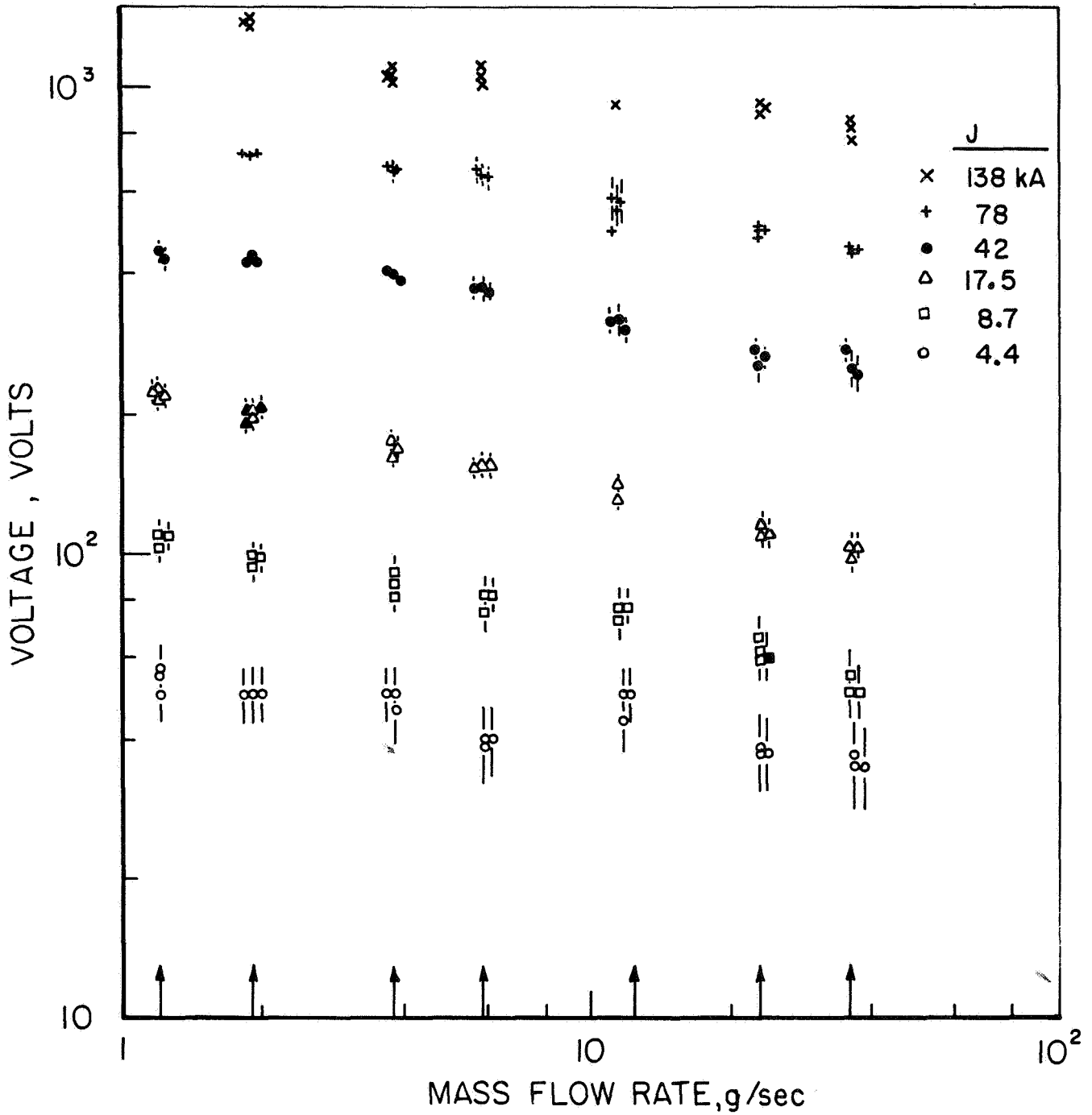


TYPICAL ACCELERATOR VOLTAGE - CURRENT HISTORY

The spike is rapidly followed by a sharp drop to a value of 180 volts which remains constant for the duration of the pulse. This drop is interpreted as signifying the attainment of thermionic emission by the cathode, since any other mechanism would require substantially higher voltages to support this current density.

Steady voltage traces of this sort are observed over almost the entire range of current and mass flow rate. Although some operating conditions produce more irregular early histories (for reasons shown later), they too eventually reach a plateau. Voltages quoted or plotted throughout this chapter are these plateau values.

In Fig. 6-4, the measured plateau voltages are presented as a function of mass flow rate for the six different current levels. The injected mass flow rates, accurate to approximately 10 percent, are shown at the bottom of this figure as small arrows. When many data points are closely grouped at a given operating condition, they are spread out for clarity. At the higher current levels, the low interstation inductance and the particular bank configuration (parallel, series-parallel, or series) combine to give a reproducible ripple in the current of approximately 10 percent about the nominal value. Since this generates a time dependent voltage, the data is reduced by only reading the voltage and current at those times for which $\dot{J} = 0$. This technique eliminates an inductive component of the voltage, $L\dot{J}$, which is spurious to this measurement.

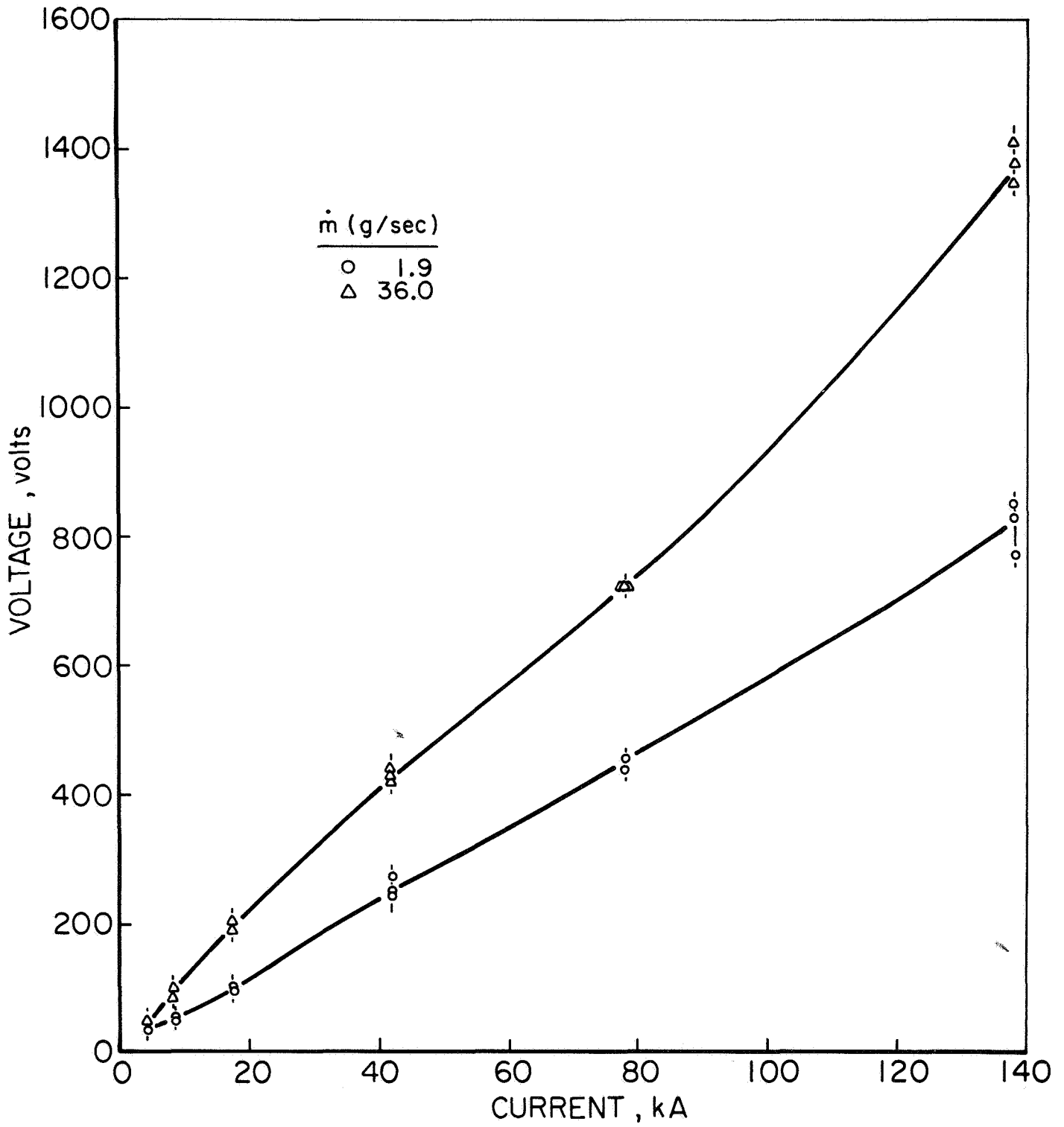


SUMMARY OF VOLTAGE MEASUREMENTS

FIGURE 6-4

These data points then yield an average arc impedance which is multiplied by the nominal current to produce the voltage recorded in Fig. 6-4. At the low current levels, which display no variation in the flattop current, the principle error is a reading error. The resulting uncertainty of each data point is indicated by a small vertical line, if this exceeds the symbol size. These data clearly display the increase in voltage with current and decrease with mass flow rate anticipated from the electromagnetic thrust model. This effect is shown more clearly in a cross plot of the data for the extreme mass flow conditions, as shown in Fig. 6-5. These voltage-current characteristics illustrate a pattern observed for all voltage data, namely, the slope of the particular characteristic is dependent upon the operating regime. Note that at the highest value of the magnetic interaction parameter, β , (high current and low mass flow rate) the slope of the characteristic becomes increasingly positive at higher currents consistent with the presence of the self-field thrust mechanism.

Returning to Fig. 6-4, two checks on the reliability of the data are displayed therein. In the first of these, the characteristic impedance of the capacitor bank is shown to have no effect on the voltage data, since the same current level supplied with two different bank configurations yield indistinguishable voltages. In the usual configuration (the open data point), the voltage for a current of 8.7 kA and a mass flow rate of 23.0 g/sec was measured with the capacitor bank



VOLTAGE - CURRENT CHARACTERISTICS

FIGURE 6-5

arranged to provide 8.7 kA when charged to an initial voltage of 10 kV. In the check, the bank was altered to provide 17.5 kA when charged to 10 kV, a reduction in the effective bank impedance by a factor of two, but was in fact only charged to 5 kV, thereby providing a current of 8.7 kA. The shaded data point at these conditions shows that the terminal voltage is not dependent on the bank impedance--only on the current which it supplies.

The second check concerned the method of supplying various mass flow rates. It has been previously mentioned that in order to avoid time-consuming injector changes, different mass flow rates were obtained by varying the driver pressure with the same injection hole size. Thus, the three highest mass flow rates (11.5, 23.0, and 36.0 g/sec) were obtained with a common set of injectors (0.152-in. diameter) but with driver pressures of 15, 35, and 60 psia, respectively. Similarly, mass flow rates of 1.9, 3.8, and 5.9 g/sec were obtained with the same driver pressures but a smaller set of injectors (0.0625-in. diameter). The lowest mass flow rate, 1.2 g/sec, was provided by an injector set of 0.0355-in. diameter and a driver pressure of 35 psia. Increasing this pressure to 60 psia with the same injectors then provides a mass flow rate of 1.9 g/sec, which should be the same as produced by the 0.0625-in. diameter injectors with a 15 psia driver pressure. The shaded voltage data point at 17.5 kA and 1.9 g/sec resulted from the high pressure, small injector combination while the open point was achieved with the low pressure, large injector

configuration. The good agreement between these two voltage measurements verifies the reliability of this technique, and supports the orifice mass flow calculations.

III. DISCUSSION

There are many ways in which raw terminal voltage data such as shown here can be analyzed. In the following discussion, one example technique based on a comparison of the measured values with analytical values constructed from the various contributing components is outlined. Naturally, the extent to which such an analysis can be considered quantitative is directly dependent upon the accuracy with which the original data is known. This particular method has been selected because it illustrates some interesting qualitative conclusions regarding various regimes of arc operation.

Precise correlation between measured and analytically constructed voltages is complicated by the various power loss mechanisms acting in the discharge. Specifically, the measured voltage must reflect not only the electromagnetic acceleration process, but also the energy transfer to the electrode surfaces and the electrothermal deposition of energy into the gas stream. Thus, a power balance can be written as

$$VJ = V_b J + V_a J + V_c J + V_t J \quad (6-1)$$

where VJ = total electrical input power
 $V_b J$ = electromagnetic thrust power
 $V_a J$ = power delivered to anode heating

$V_c J$ = power delivered to cathode heating

$V_t J$ = electrothermal power to gas

The electromagnetic component of the total voltage, V_b , reflects the acceleration of the mass flow through the discharge electric and magnetic field distributions by the $\vec{j} \times \vec{B}$ body force. The associated thrust power can be given by the integral of $\vec{j} \times \vec{B} \cdot \vec{u}$ over the entire discharge volume, or, in terms of terminal properties,

$$V_b J = \frac{T_b^2}{2\dot{m}} \quad (6-2)$$

from which

$$V_b = \frac{\mu^2 J^3}{32\pi^2 \dot{m}} \left[\ln \left(\frac{r_a}{r_c} \right) + \frac{3}{4} \right]^2 \quad (6-3)$$

by virtue of the familiar self-field electromagnetic thrust expression discussed earlier [Eq. (2-1)].

Values of the anode and cathode fall voltages, V_a and V_c , and their dependence on current and mass flow rate are not well known. However, certain electrical probe studies of similar discharges in this laboratory [80] show that the cathode fall voltage is of the order of the work function of tungsten, about 5 volts, and the anode fall voltage is in the vicinity of 15 volts for currents up to 300 kA. The dependence of these values on current and mass flow rate, although not carefully studied, appears to be weak. These measurements are consistent with the extension of the voltage-current char-

acteristic at fixed mass flow (Fig. 6-4) to zero current which yield a total fall voltage of 10 to 30 volts. In addition, measurements on a steady state self-field MPD accelerator have shown an anode fall voltage of 15-18 volts and a cathode fall voltage of about 3 volts over a large, but lower range of current and mass flow rate [81]. Thus, for purposes of analytically approximating the total voltage, it will be assumed that the sum of V_a and V_c is fixed at 20 volts, independent of mass flow rate and current. Such an assumption will not greatly influence analyses based on voltage measurements at the higher currents since this component represents only approximately two percent of the total voltage drop at those conditions. However, as the current is decreased, this component becomes proportionally larger reaching 10 percent of the terminal value for a current of 17.5 kA and a maximum of 50 percent of it at the extreme conditions of 4.4 kA current and 36.0 g/sec mass flow rate.

The electrothermal voltage component, which is present in any arc discharge, corresponds to the deposition of energy into the gas stream via Joule heating, j^2/σ per unit volume (where σ is the local electrical conductivity) part of which provides the requisite ionization of the gas. In an electromagnetic accelerator, this resistive component is also related to the inherent mismatch of the applied field E with the back EMF generated by the accelerated gas, uB , a mismatch which arises from the need for simultaneous satisfaction of Maxwell's relations on the field properties and the plasmadynamic momentum equation [82]. This dissipation accounts for the local differ-

ence between the total electrical input, $\vec{J} \cdot \vec{E}$, and the useful work, given by the scalar product of the body force $\vec{j} \times \vec{B}$ and the velocity \vec{u} . The "dynamic inefficiency" inherent in this mismatch is much like the inefficiency discussed earlier in relation with the accumulation of mass by a snowplowing current sheet in a pulsed plasma accelerator. The power thus dissipated encompasses the ionization of the flow, and all internal excitation, random thermal, and radiation processes which accompany it. A portion of this, most probably just that amount in random thermal modes, can be recovered by an expansion to produce a useful thrust component, T_t , but the remainder constitutes a frozen flow loss, i.e.,

$$V_t J = \frac{T_t^2}{2\dot{m}} + \text{frozen flow loss} \quad (6-4)$$

This division of electrothermal input power is immaterial insofar as its contribution to the terminal voltage is concerned, but the total thrust, as would be measured on a thrust stand, would reflect it, i.e.,

$$T = T_b + T_t + T_{cf} - T_l \quad (6-5)$$

where T_{cf} = cold flow thrust

T_l = thrust losses due to a nonuniform velocity profile, viscous drag on the nozzle wall, and divergence of the accelerated gas

Since only T_b can be readily evaluated, we will employ an efficiency defined as

$$\eta = \frac{\text{electromagnetic thrust power}}{\text{electrical input power}} = \frac{V_b}{V} \quad (6-6)$$

which will be conservative by the amount with which T_t exceeds T_f .

Since the dependence of the resistive component of the voltage on mass flow rate and current is unknown, it is instructive to compare the measured terminal voltage with the analytically constructed voltage, exclusive of this component. Figure 6-6 shows an example of this comparison for a fixed current of 17.5 kA. The measured values, V , are shown by the data points and the dashed average line through them; the calculated voltage, composed of the acceleration component V_b as calculated from (6-3) and a fixed total electrode fall voltage of 20 volts, is shown by the curve marked $V_b + 20$. The difference between these curves should then be V_t , as shown on the same figure. As the mass flow rate is decreased from the higher values, the efficiency, as previously defined, increases since V_b increases faster than V . Eventually a point is reached where the curves cross, yielding the untenable results of an analytical voltage greater than the measured value, indicating an efficiency greater than one and a thermal component which is negative.

The problem of low mass flow operation in a steady state MPD arc is a familiar one, discussed previously in Chap. 2. Briefly, this regime has been shown to involve entrainment and reacceleration of the ambient gas, aided by extension of the current conduction region out into the exhaust plume [32]. Other experiments have demonstrated the additional problem of erosion of electrode material in this operating regime [33]. Spectroscopic measurements on a long pulse

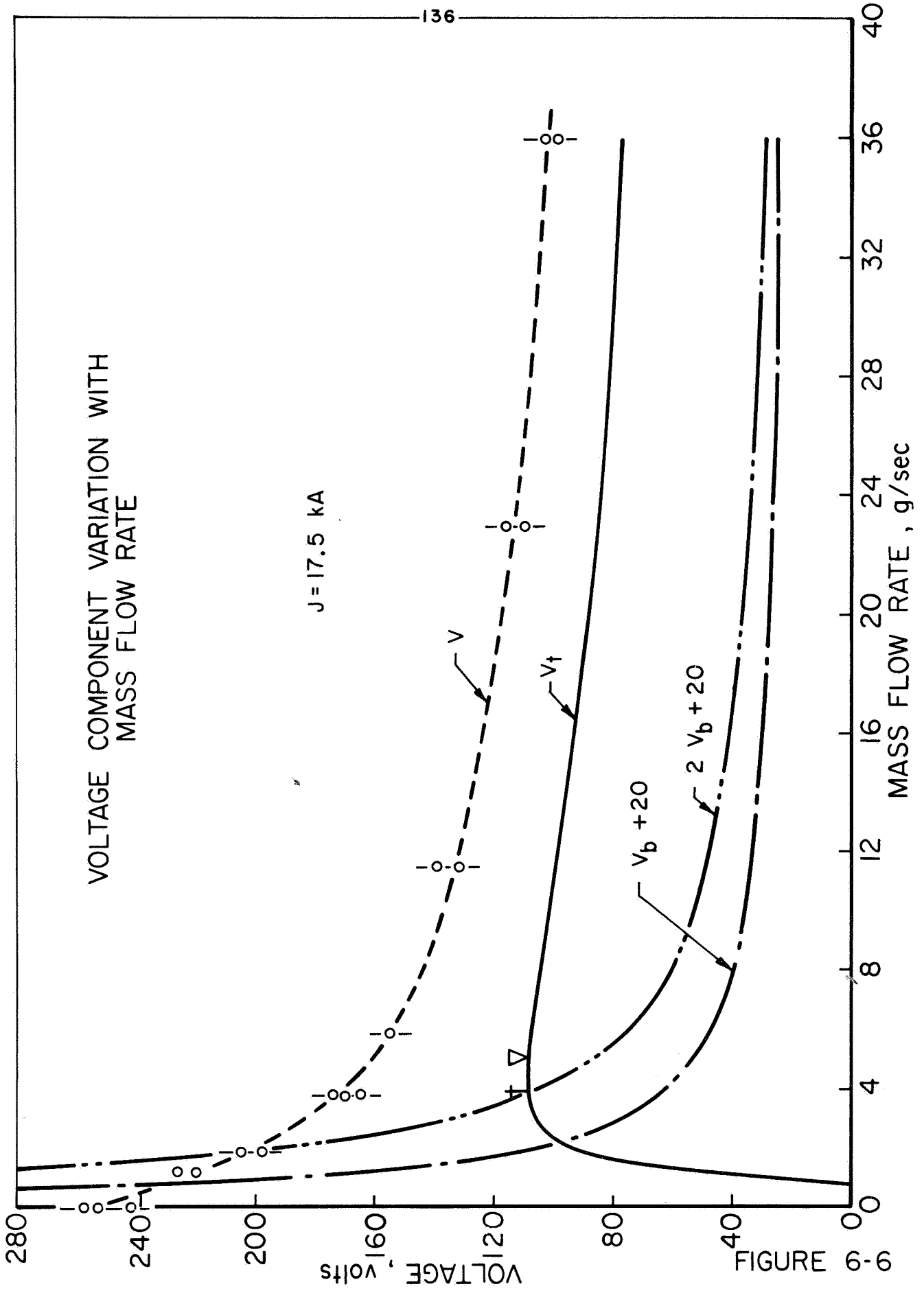
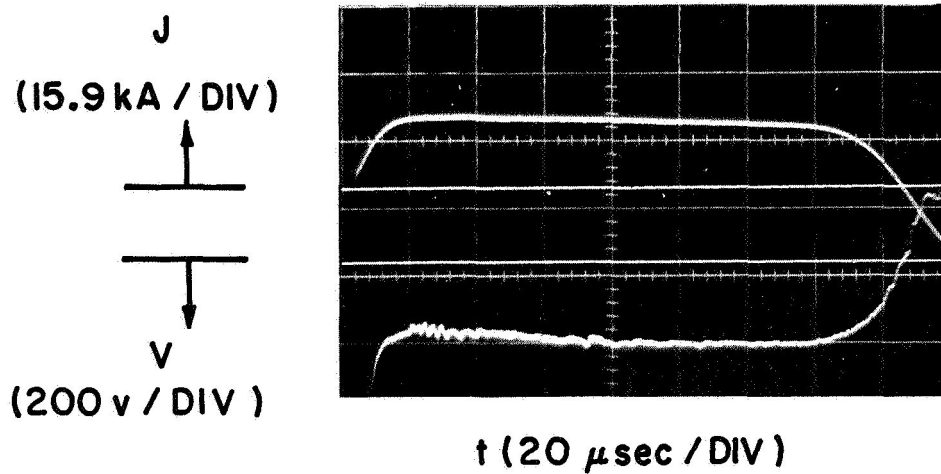


FIGURE 6-9

parallel-plate accelerator in this laboratory have also shown that as the supplied mass flow rate is decreased, the presence of electrode and insulator materials in the exhaust increases [67]. In fact, the data point for zero mass flow rate in Fig. 6-6 offers an excellent example of this extraneous mass process in the present accelerator. The voltage is measured at this condition by completely blocking the mass injectors into the chamber, prefilling the chamber and tank to a pressure greater than the Paschen limit at 10 kV, say 10^{-1} torr, and triggering the switch by an externally supplied puff of gas. The resulting voltage signature across the arc chamber is shown in Fig. 6-7. The voltage rises during the first 80 μ sec, consistent with the depletion of mass within the arc chamber, eventually reaching a sufficiently high plateau where the discharge sustains itself on vaporized electrode and insulator material. Comparison of this signature with that shown in Fig. 6-3 reveals that the zero injected mass case is less steady, indicative of the increased difficulty experienced by the arc in providing current carriers.

To correct for this spurious mass, data points which involve entrainment or erosion effects should be moved to the right in Fig. 6-6 but the extent of this correction is, of course, unknown. (The experimental determination of mass lost from the insulators and electrodes of a pulsed plasma accelerator is complicated by two effects: First, the rate of loss of absorbed mass is a sensitive function of the material outgassing properties and the number of shots. In addition, dif-



VOLTAGE SIGNATURE FOR ZERO INJECTED
MASS FLOW

$$P_{\text{amb}} = 10^{-1} \text{ torr}, J = 17.5 \text{ kA}$$

FIGURE 6-7

ferential weight measurements after a series of shots is difficult in that the absorbed mass can be greater than both the eroded or ablated mass and the injected neutral mass [83].

Second, there is an uncertainty surrounding the time dependence of mass lost during any given pulse. Consequently, to properly deduce the rate of total mass ingestion during the quasi-steady phase requires a carefully controlled experiment beyond the scope of this thesis.) The next paragraph deals with correction of the theoretical voltage by an amount consistent with an estimate of the thermal component which improves the agreement with measured voltages at high mass flow rates. In the "starvation" region, however, this same correction worsens the discrepancy and shifts the cross-over point toward higher values of \dot{m} . A starvation mass flow, \dot{m}_s , may be defined as a function of discharge current, below which mass ingestion effects distort appraisal of arc operation. These values of \dot{m}_s surely lie somewhere above the cross-over point, perhaps where the difference curve V_t reverses its slope (\dagger) or curvature (∇ , Fig. 6-6). In any event, it now appears that the upper left region in Fig. 6-1 is inaccessible to ideal accelerator operation.

The mass flow dependence of the resistive voltage component is basically unknown, but it is interesting to postulate an equipartition of input power between it and the acceleration term, exclusive of the fall voltages. Such an equipartition arises in theoretical treatments of one-dimensional, external field accelerators; slightly more favorably division can be derived for ideal one-dimensional self-field accelerators [82].

In addition, a similar approach has been empirically profitable for correlating steady state external field results, the so-called critical velocity model [17]. The analytical voltage curve resulting from this equipartition assumption is shown in Fig. 6-6, labelled $2V_b + 20$. As mentioned, this calculated voltage increases the questionable operation region at the lower mass flow rates while decreasing only slightly the disagreement to the right of the intersection point.

Terminal voltage measurements in steady state MPD accelerators display the same insensitivity to mass flow rate, and thus the same type of disparity with theoretical voltage estimates in the high mass flow regime. The disagreement between high mass flow, steady state theoretical and measured voltages is commonly explained in terms of slippage between the ion and neutral species in the acceleration region. This argument is supported by species velocity measurements in the exhaust of external field accelerators which show the ion velocity an order of magnitude greater than the neutral atom velocity [48], and by ion-neutral mean free path calculations. Thus, only a fraction of the supplied mass flow may actually be accelerated, and data points to the right of the intersection of the theoretical and experimental voltage lines should be moved to a lower mass flow rate appropriate to the actual mass flow accelerated.

For the quasi-steady measurements presented here, this slippage hypothesis is less acceptable because of the substantially larger number of collisions in the acceleration zone.

The mean free path for ion-neutral momentum transfer collisions can be calculated from

$$\lambda = \frac{1}{n_o Q_{io}} = \frac{MV_{io} A}{\dot{m} Q_{io}} \quad (6-7)$$

where n_o = neutral number density

M = particle mass

V_{io} = relative velocity between ion and neutral

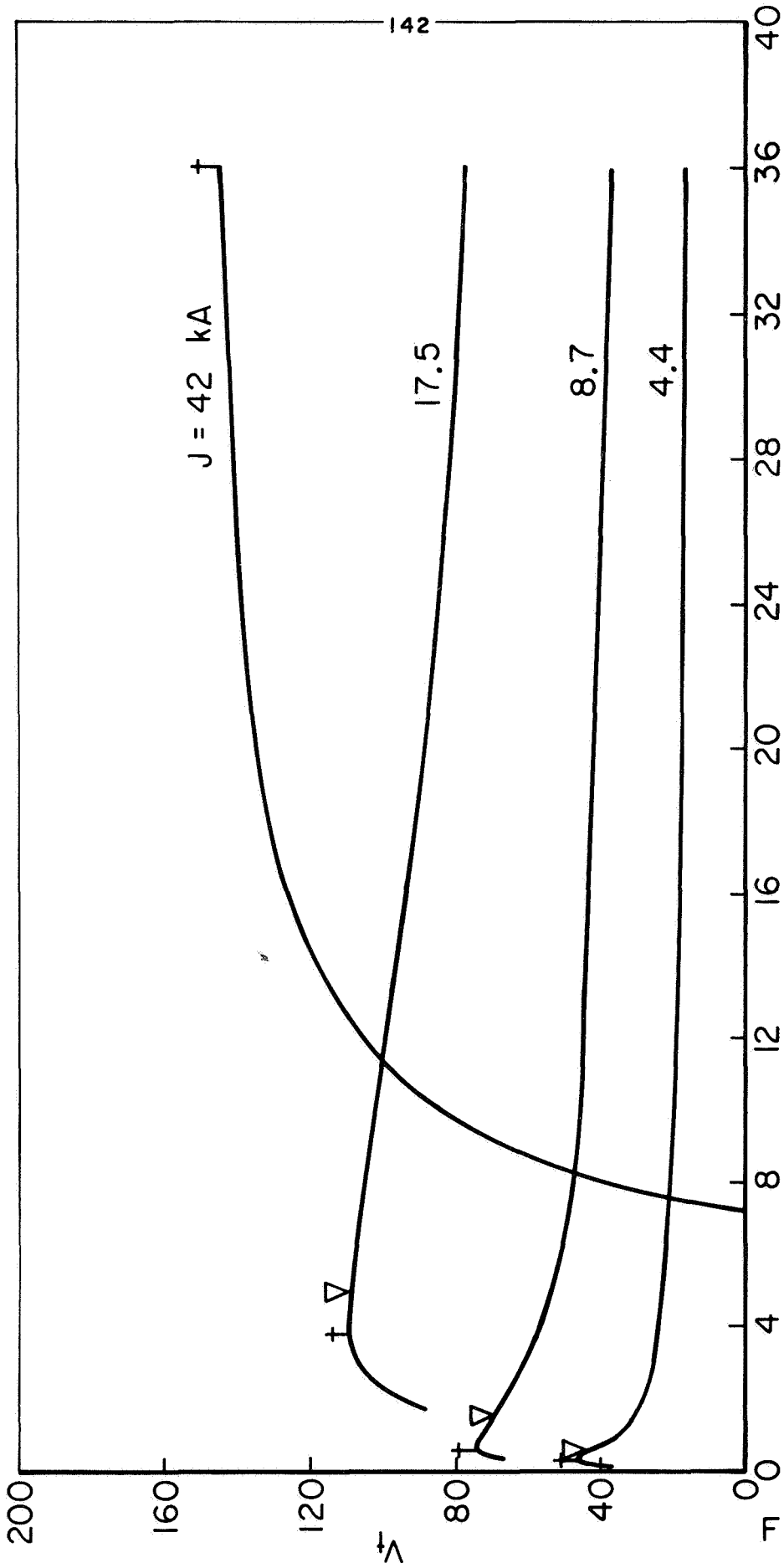
A = cross-sectional area of acceleration zone

Q_{io} = pertinent ion-neutral cross section—in this case, the charge exchange cross section

Since a conservative estimate of the species coupling is desired, i.e., the maximum mean free path, then the maximum velocity should be incorporated. As seen from the electromagnetic thrust relation

$$\frac{\mu J^2}{4\pi} \left[\ln \left(\frac{r_a}{r_c} \right) + \frac{3}{4} \right] = \dot{m} v \quad (6-8)$$

increasing the current for a given mass flow rate increases the velocity of the accelerated mass. However, the extremely high velocities predicted by high currents are obviously subject to the ingestion-erosion considerations discussed earlier (Fig. 6-1). Thus, for any given mass flow rate, there is a maximum current and velocity consistent with proper arc operation. This limiting velocity can be estimated from the \dot{m}_s limits marked on the various V_t curves plotted in Fig. 6-8. A cross plot of these mass flow rates against the current, as shown in Fig. 6-9, indicates that a current squared dependence is suitable for determining the approximate maximum velocity conditions. The



MASS FLOW RATE, g/sec

DERIVED RESISTIVE VOLTAGE COMPONENTS

FIGURE 6 - 8

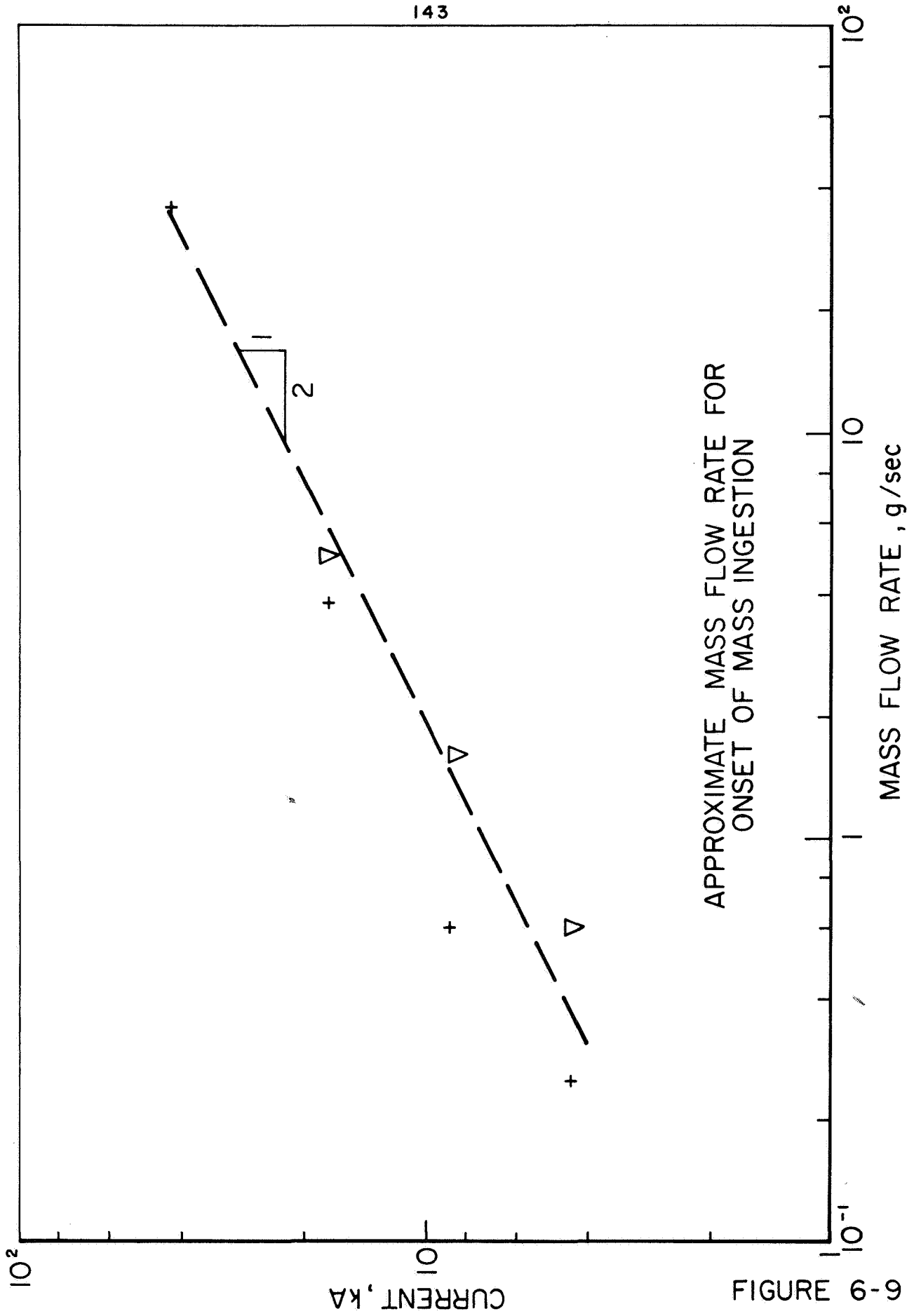


FIGURE 6-9

equation for the dashed average line through these data is

$$\dot{m}_{\min} = \dot{m}_s \approx 1.90(10^{-8})J^2 \quad (6-9)$$

or

$$J_{\max}^2 \approx 5.25(10^7)\dot{m} \quad (6-10)$$

for \dot{m} in g/sec and J in amps. For this maximum velocity, the number density therefore becomes

$$n_{o,\min} \approx (1.3)10^{14} \dot{m}$$

for \dot{m} in g/sec and n in cm^{-3} . For $A = 81 \text{ cm}^2$ (the full anode orifice area) and $Q \approx 2.8(10^{-15})$, in accord with the $1.4(10^4)$ m/sec velocity resulting from Fig. 6-9 [43], the resulting range of λ is 2.3 cm for the lowest mass flow rate and 0.07 cm for the highest. The significant quantity is the ratio of the length of the acceleration region, l_a , to this mean free path. Taking $l_a \approx 6 \text{ cm}$ (as will be shown in Chap. 7), the minimum value of this ratio lies in the range

$$2.6 < \left(\frac{l_a}{\lambda} \right)_{\text{quasi-steady}} < 79$$

which, in view of the efficiency of equal mass collisions, seems to deny any significant degree of ion slip. Note especially that at the highest mass flow rates where the voltage observations and analyses diverge most, the coupling is most effective.

This may be compared with a similar calculation for the steady state accelerators using the results of recent species velocity measurements [48,84]. Using a radius of 1 cm, a measured velocity of $1.5(10^4)$ m/sec, and an effective acceleration

length of 1 cm, this ratio lies in the range

$$0.15 < \left(\frac{l}{\lambda} \right)_{\text{steady state}} < 0.9 \quad [\text{Ref. 48}]$$

$$0.15 < \left(\frac{l}{\lambda} \right)_{\text{steady state}} < 0.3 \quad [\text{Ref. 84}]$$

Thus, ion-neutral slip may be marginally tenable in this domain.

Note that it is the size of the acceleration region which distinguishes the two classes of accelerator, rather than the mean free paths, which are about the same for the two cases. The latter result from similar ion-neutral cross sections and equivalent \dot{m}/A values which follow from the original dimensional scaling of the quasi-steady experiment. The observed larger acceleration zone and the resulting improved ion-neutral species coupling must thus be regarded as a distinct advantage of the high-current accelerator.

Rather than discuss further empirical modifications to the theoretical voltage in accordance with other assumptions concerning the resistive component mass dependence, this component can be plotted directly from $V_t = V - (V_b + 20)$ as shown in Figs. 6-6 and 6-8. In each case, V_t reaches a constant asymptote, \hat{V}_t , at high mass flow rate implying no further thermal input regardless of the increase in mass flux. Unfortunately, V_t cannot be plotted for the high currents without extrapolating the data to very large mass flow rates. For those currents where the asymptote \hat{V}_t can be identified ($J < 20$ kA), it increases linearly with current at a slope of 4.2 ± 1.1 volts/kA, i.e.,

there is a large domain in the lower right of Fig. 4-1 where the plasma has a constant resistance of approximately 0.004Ω independent of current and mass flow rate. Since the current conduction pattern during the quasi-steady acceleration phase remains essentially unchanged throughout this domain (as will be shown in the next chapter), the fixed resistance implies a fixed conductivity. For a fixed mass flow rate, increasing the current with a constant conductivity increases the thermal dissipation within the gas. However, because of the vulnerability of electrons to ionizing collisions on neutrals, almost all of the energy is deposited in this ionization sink, i.e., the bulk of the energy appears in increased ionization, rather than in an increase in temperature. Thus, the observed constant electrical conductivity appears insensitive to the fractional ionization or electron number density in this regime.

As the mass flow rate is increased for a given current, the number density drops out of the conductivity expression if coulomb collisions are assumed to dominate over electron-neutral collisions [85], and thus the observed constant conductivity again implies that the temperature is essentially unchanged.

Knowing the constant plasma resistance, an estimate of the plasma conductivity can be formulated from

$$R = \frac{l}{\sigma A} = \int_{r_c}^{r_a} \frac{1}{\sigma} \frac{dr}{2\pi r z(r)} \quad (6-11)$$

where z , the axial extent of the current conduction zone, is

assumed to vary linearly with r , in close approximation to the measured current contours shown in Chap. 7. Assuming a spatially uniform conductivity, and taking the minimum cathode attachment radius, above which at least 25 percent of the current can be found, as 0.25 cm, the conductivity becomes

$$\sigma = \frac{1}{2\pi R} \int_{0.25}^1 \frac{dr}{3r^2} + \frac{1}{2\pi R} \int_1^5 \frac{dr}{r(2.5 + 0.5r)} \quad (6-12)$$

$$= \frac{1}{2\pi R} (1.00 + 0.45) = \frac{0.23}{R} \approx 50 \frac{\text{mho}}{\text{cm}}$$

where the integration limits are in cm. This figure is accurate to approximately 40 percent due to the uncertainty in the resistance value and the lower integration limit on the first term of Eq. (6-12). Since the conductivity is essentially dependent only on the electron temperature, a rough estimate of this temperature can be made. With reference to recent calculations of the electrical conductivity of argon with an arbitrary degree of ionization [86], the minimum electron temperature indicated (that for complete single ionization) is $1.8 \text{ eV} \pm 0.5 \text{ eV}$. In addition, this reference indicates that the minimum fractional ionization which can support the observed conductivity is approximately 0.08, in which case the temperature is a maximum at about 5.2 eV. These limits are in good agreement with measurements in both pulsed accelerators [75] and steady state MPD arcs [41].

One other result from these voltage measurements is of interest. Recalling that the electromagnetic efficiency has

been defined [Eq. (6-6)] as the ratio of the acceleration voltage component to the total voltage, and that $V_b \propto J^3/\dot{m}$ from (6-3) while the total voltage V is approximately proportional to J as shown in Fig. 6-5, then

$$\eta \propto \frac{J^3/\dot{m}}{J} = \frac{J^2}{\dot{m}} \quad (6-13)$$

Thus, for a fixed mass flow rate, the efficiency should increase with the square of the current. From Fig. 6-6 and similar curves drawn for other arc currents, it is found that η does in fact increase in the predicted manner until the "starvation" region is entered. Beyond J_{\max} (given approximately by Eq. 6-10), the efficiency values are too high because the additional entrained mass is not included in the calculation. Although higher mass flow rates allow η to increase over a greater range of J , the efficiency at any given current is decreased, and the resulting maximum efficiency before extraneous mass ingestion occurs will be far less sensitive to J than is indicated by Eq. (6-13). Figure 6-10 displays this maximum efficiency as a function of current. The values are derived at each current from the ratio of calculated V_b to measured V at the two mass flow rates estimated as the limits of \dot{m}_g . Note that although the exact criteria for the onset of mass ingestion cannot as yet be established, an increase of η with J seems demonstrated. The rate of this increase, and the possibility of a limiting value, are not clearly established by these data, however, and extension of the voltage measurements to higher mass flow rates is indicated.

41 43 K71314 63

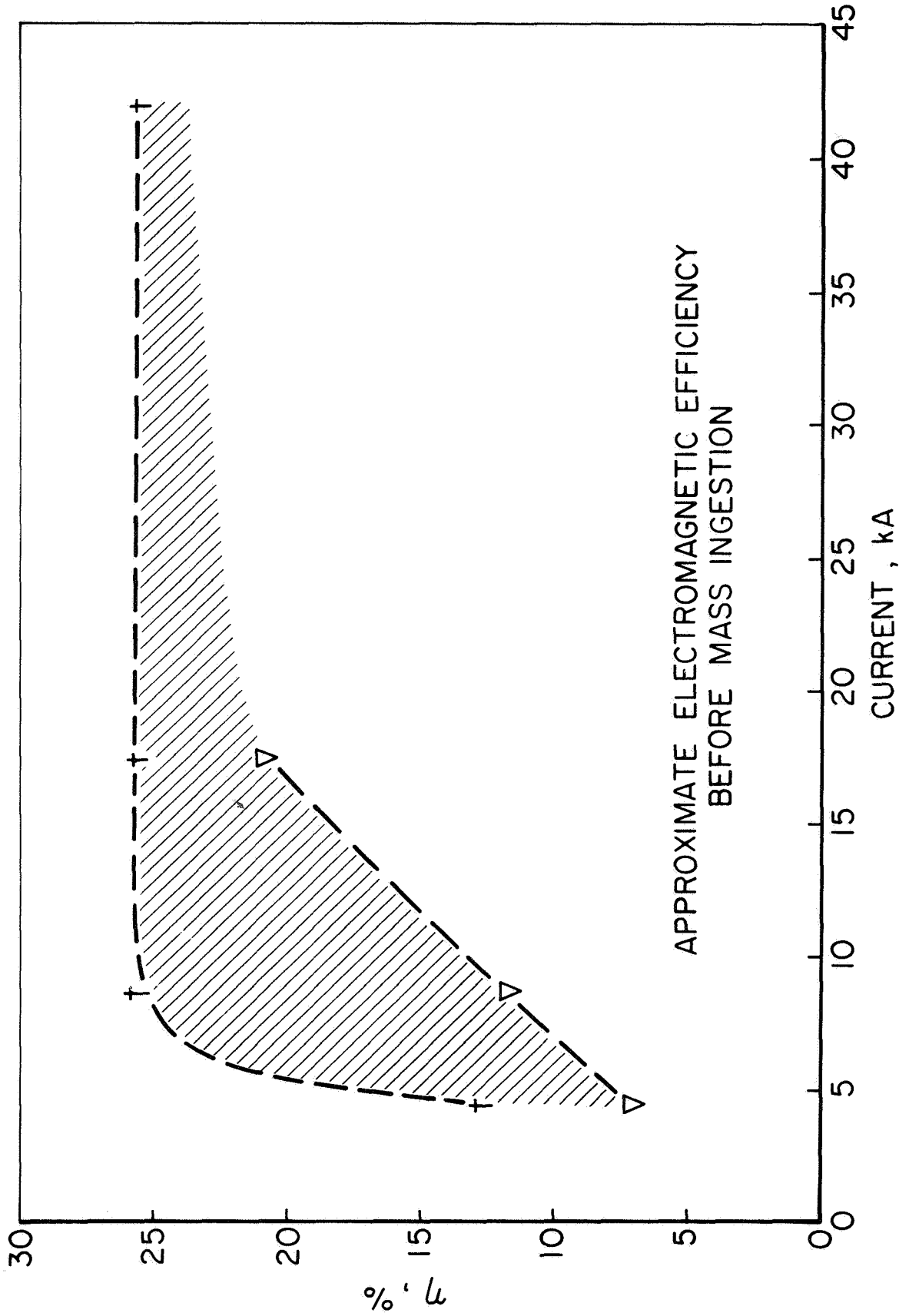


FIGURE 6-10

CHAPTER 7

RESULTS II: DISCHARGE STRUCTURE

I. INTRODUCTION

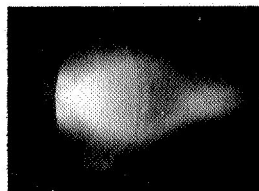
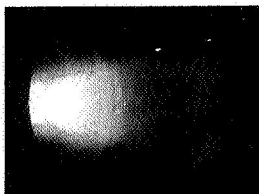
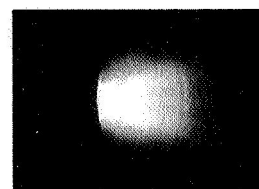
The preceding chapter described how terminal voltage measurements on the quasi-steady accelerator provide an indication of the acceleration mode and overall efficiency. Similiar techniques have been employed in steady state MPD experiments at considerably lower powers. In neither case, however, do such terminal data yield much insight into the details of the discharge structure and acceleration mechanisms. In the steady experiments, little more can be done to determine local plasma properties due to the environmental and probe size restrictions discussed previously; with the present quasi-steady operation, several techniques are available. Of these, the simplest and most direct are the photographic studies and magnetic field mappings which have been shown in other pulsed plasma experiments to yield reliable information about the overall discharge development and current distribution. This chapter describes the results of these two measurements.

II. PHOTOGRAPHIC STUDIES

Photographs of the discharge luminosity at various times, and with various operating conditions were taken with a Crown Graphic camera through a Kerr-cell shutter [78].

Two different shutters were used: For the three high-current, shorter pulses, a shutter with a 50 nsec nominal open time provided proper exposure with good resolution; for currents of 17.5 kA and lower, a 5 μ sec shutter was used in order to expose the film sufficiently. The 35 kV power supply for either shutter was triggered from an oscilloscope whose sweep was synchronized to the discharge by the Rogowski coil signal. The internal delayed trigger network of the oscilloscope allowed precise setting of the particular time interval which corresponded to the film exposure. The photographs were found to be most informative when taken from a perspective angle of about 45° to the centerline since the large anode orifice then allowed observation of the cathode tip as well as of part of the chamber interior.

A typical luminosity history from breakdown through the establishment of a stabilized phase is shown in Fig. 7-1 for a current of 17.5 kA and an argon mass flow rate of 5.9 g/sec. Figure 7-1a shows the discharge initiating in the form of several spokes from the base of the cathode cone to the interior rim of the anode. With reference to Fig. 5-14b (a perspective view of the discharge chamber at a slightly different angle), these spokes lie in r-z planes at azimuths bisecting adjacent mass injectors. By 10 μ sec (Fig. 7-1b), which is less than the rise time of the current to its flat-top value the spokes have disappeared and a nearly axisymmetric luminosity pattern is confined to the region in the vicinity

a) 2 μ secd) 30 μ secb) 10 μ sece) 40 μ secc) 20 μ secf) 140 μ sec

KERR CELL PHOTOGRAPHS OF DISCHARGE LUMINOSITY
TRANSITION TO STEADY PHASE

$J=17.5$ kA; $\dot{m} = 5.9$ g/sec

of the cathode. It is important to note that the cathode tip, which appears dark at 2 μ sec, is now very bright with a small attached luminous plume. Interpretation of this as the onset of thermionic emission agrees with the rapid overall voltage drop observed at this time (see Fig. 6-3). Figure 7-1c shows that by 20 μ sec, a large plasma ball is emerging from the chamber. Drawing on previous experience with completely unsteady discharges, this initial phase is interpreted as a "sweeping" of the initial resident mass in the chamber by a propagating current distribution. In this geometry, there is current pattern propagation in both the inward radial and axial outward directions which sweeps the plasma toward the center of the anode orifice.

In Figures 7-1d,e and f, this ejected plasma propagates further downstream leaving in its wake a luminosity distribution which remains unchanged for the balance of the pulse. Thus, based on the luminosity patterns, the discharge in the arc chamber and near exhaust appears stabilized from 30 μ sec until the end of the pulse at 160 μ sec.

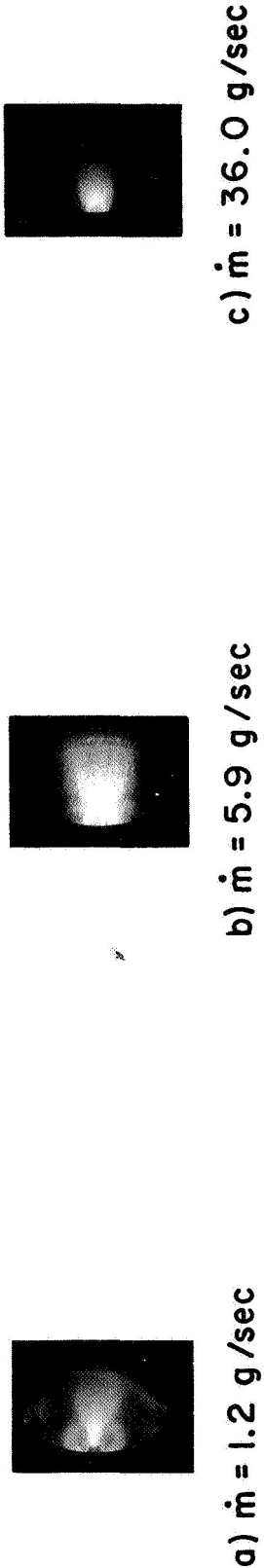
In its stabilized configuration, the discharge exhibits certain features which are characteristic of all operating conditions.

1. As in self-field MPD arcs at an order of magnitude lower current, the discharge is invariably axisymmetric within the resolution of all experimental techniques. In particular, there is no experimental evidence to suggest the presence of a spoke.

2. The tungsten cathode tip achieves a luminosity indicative of thermionic emission, a contention that is reinforced by observations of local melting and slight surface damage to the tip of the cathode.

3. A sharp demarcation line between light and dark exists at the upstream edge of the luminosity. The effect is most pronounced at the tightly confined region near the cathode tip and, as shown later, is not directly correlated with the current conduction pattern. There is a possibility that this line is indicative of a shock wave caused by the focussing action of the electromagnetic forces; but this hypothesis cannot be checked by any simple measurement.

Although these general features of the luminosity development are preserved when operating at conditions other than 17.5 kA and 5.9 g/sec, certain quantitative differences are noted. For fixed current the time for completion of the transient phase increases with the mass flow rate. Some details of the stabilized pattern are also affected by mass flow. Figure 7-2 shows a group of photographs each taken 80 μ sec after the 17.5 kA discharge initiated, but with different mass flows. Figure 7-2b displays the nominal condition discussed above; Fig. 7-2a,c show patterns for substantially lower and higher mass flow, respectively. It is seen that as the flow



STABILIZED EXHAUST LUMINOSITY PATTERNS FOR VARIOUS MASS FLOW RATES

$J = 17.5 \text{ kA}, t = 80 \mu\text{sec}$

FIGURE 7-2

rate is decreased into a regime where entrainment or erosion may occur, the cathode tip luminosity and the distinction between light and dark areas in front of the cathode become more distinct. In addition, as the mass flow rate is decreased from 36 g/sec, a new region of luminosity appears in the rear of the chamber which may be related to the need for an additional source of mass to sustain the discharge. This effect appears most intense at a mass flow rate of 5.9 g/sec, but is exhibited most clearly at the lowest flow rate as shown in Fig. 7-2a. A similar set of observations prevail when the mass flow rate is fixed and the discharge current is varied, decreased current at fixed mass flow rate corresponding to increased mass flow rate at fixed current and vice versa. That is, the discharge luminosity patterns appear to be influenced by the combination of current and mass flow rate, rather than by either separately, suggesting that the magnetic interaction parameter, β (see p. 114), is the pertinent variable. Referring to Fig. 4-1, lines of constant β are parallel to the displayed lines of constant specific impulse. Thus, for a fixed specific impulse, the low β regime toward the lower right may define one discharge mode, and the high β region in the upper left, quite another mode, which display the characteristics discussed above.

III. CONDUCTION CURRENT DISTRIBUTION

The current distribution in the arc chamber and exhaust plume and its variation with arc operating conditions were determined by magnetic probes. Briefly, these probes are small

multi-turn coils which generate a voltage across their wire leads proportional to the time rate of change of the magnetic flux threading the coil opening. Integration of this signal then provides a history of the magnetic field at the coil location. With an assumption of azimuthal symmetry, Ampere's law allows transformation of this measurement into the total current enclosed within a circle whose radius is equal to the probe position. Cross plotting a family of these local records then yields the current conduction pattern in the discharge at any given time.

Two sets of four magnetic probes each were used to determine the desired distributions over the discharge operating range. The first set utilized coils made by winding 17 turns of #32 Formvar wire into two layers on a 0.125-in. mandrel. The resulting probes have a rise time considerably less than 1 μ sec, but also have a relatively low sensitivity, limiting their use to currents above 30 kA. For probing the current range down to 4 kA, a more sensitive set of probes was made by winding 125 turns of #38 Formvar into 6 layers on a 0.25-in. mandrel. Although the rise time of these units is approximately 7 μ sec, this is tolerable since the rise time of the lower current pulses (17.5, 8.7, and 4.4 kA) is 15 μ sec, and local transients associated with the early phase of the discharge development have been found to scale with this rise time. Each probe was inserted into the end of a 2-ft. long closed glass tube to protect it from the discharge. Both sets

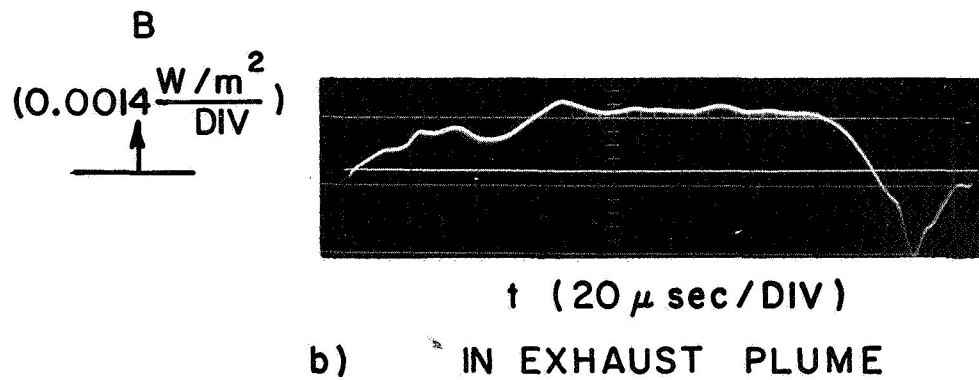
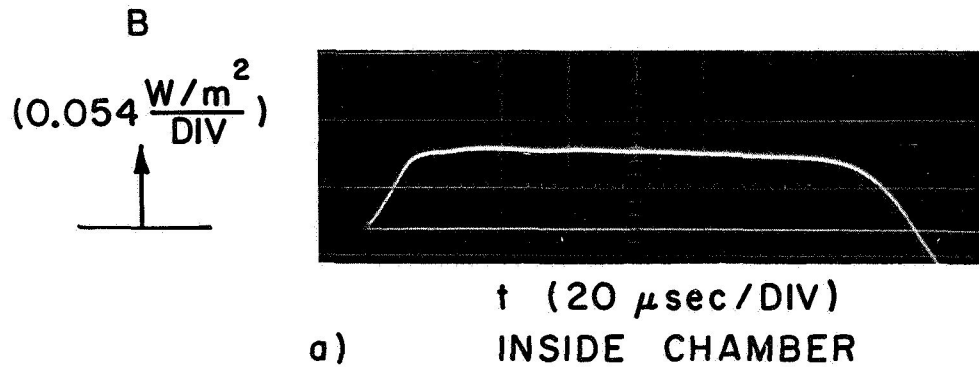
of probes were calibrated with an axisymmetric ringdown circuit consisting of several capacitors and a 2-in. long by 1-in. diameter aluminum post enclosed between two 8-in. diameter plates. The calibration factor was derived by a comparison of the probe output voltage with the magnetic field at the probe radius as calculated from the known current.

To facilitate acquiring a given matrix of data with the fewest possible shots, a given set of four probes was mounted on a movable carriage within the plexiglas tank and their outputs simultaneously recorded on two Tektronix Type 555 dual-beam oscilloscopes. A gear and pulley mechanism allowed remote placement of the probe assembly within the horizontal r-z plane. Two probes placed at equal radii but on opposite sides of the centerline showed that the discharge was axisymmetric to within 10 percent. The possible distortion of the exhaust plume development by a given probe obstacle and its consequent effect on the signal of any other probe was shown to be negligible by comparing two probe signals in different cases: In the first case, one probe was mounted just outside the anode orifice while a second probe was positioned at a smaller radius and extended into the arc chamber so that any plume distortions caused by it would be sensed by the outer probe. In the second case, this interior probe was removed leaving the undisturbed plasma to sweep over the outer probe. In both cases, the magnetic field records at the outer probe position were identical within the shot-to-shot reproducibility of the discharge (see below), indicating the absence of probe interplay. To restrict electro-

magnetic noise to a minimum, the coaxial leads from the probes were dressed tightly along the same ground plane described earlier. Integration of the signals was performed passively at the scope face with a time constant always 10 times longer than the current pulse.

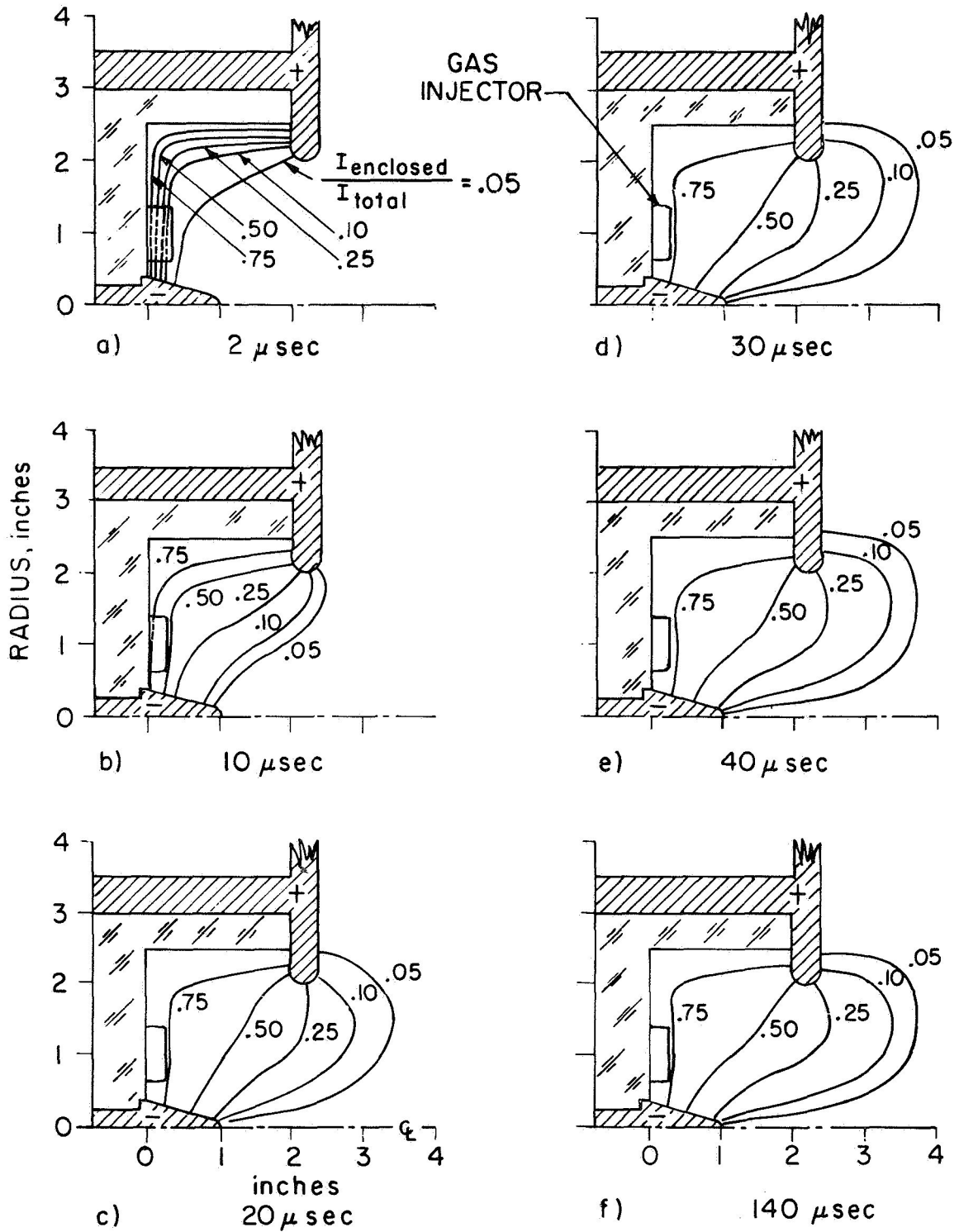
Typical oscillograms of the magnetic field history both within the arc chamber and in the exhaust plume are shown in Fig. 7-3. At these locations, the probes exhibit a steady increase in magnetic field to some plateau value which remains constant for the duration of the pulse. The slight decay in Fig. 7-3a is due to the integrator time constant and does not represent an actual decay in magnetic field strength inside the chamber. These oscillograms are indicative of the degree of reproducibility of these measurements. Inside the chamber, the smooth trace is reproducible to within 5 percent and only single discharges are necessary to achieve the desired data. Outside the chamber in the exhaust plume, the stabilized phase is reasonably smooth and reproducible (to approximately 10 percent), but the transient phase is distorted somewhat by random oscillations. In this latter case, several shots were taken at each position in order to determine an average field strength at any given time. The influence of the observed irreproducibility on the construction of the enclosed current contours will be shown after these contours are displayed.

The discharge development to its stabilized phase, in the form of enclosed current contours as reduced from the magnetic probe data, is shown in Fig. 7-4. Both the operating



TYPICAL MAGNETIC FIELD HISTORIES IN
 ACCELERATOR DISCHARGE

$$J = 17.5 \text{ kA}, \dot{m} = 5.9 \text{ g/sec}$$



ENCLOSED CURRENT CONTOURS SHOWING DISCHARGE
TRANSITION TO STABILIZED PHASE

$J = 17.5 \text{ kA}$, $\dot{m} = 5.9 \text{ g/sec}$

FIGURE 7-4

1
2
3
4
5
6
7
8
9
10
11
12
13
14
15
16
17
18
19
20
21
22
23
24
25
26
27
28
29
30
31
32
33
34
35
36
37
38
39
40
41
42
43
44
45
46
47
48
49
50
51
52
53
54
55
56
57
58
59
60
61
62
63
64
65
66
67
68
69
70
71
72
73
74
75
76
77
78
79
80
81
82
83
84
85
86
87
88
89
90
91
92
93
94
95
96
97
98
99
100

conditions ($J = 17.5$ kA, $\dot{m} = 5.9$ g/sec) and the sequence times are identical to the Kerr-cell data displayed in Fig. 7-1 to facilitate comparison between discharge luminosity and conduction current distribution. The enclosed current contours are plotted as percentages of the total current to expedite comparison among various operating conditions.

Figure 7-4a shows that in the breakdown phase, the current appears to closely follow the rear plexiglas insulator out to the chamber glass wall and along this wall to the inside of the anode lip. It should be recalled, however, that these data have been reduced with an assumption of azimuthal symmetry which obviously cannot exist in portions of the extreme rear of the arc chamber due to the mass injectors. Yet, magnetic probe records at locations adjacent to the rear insulator, but at a larger radius, verify the presence of virtually the entire current in this region. It is thus felt that the injectors poke small "holes" in the otherwise uniform current sheet, the resulting distortion indicated symbolically by the broken lines in Figs. 7-4a and b. Despite this effect, there were no irregularities in the data, such as large negative signals during the early times, to suggest the presence of spokes as observed in the luminosity pattern at this time (Fig. 7-1a). By $10 \mu\text{sec}$ (Fig. 7-4b), the discharge has propagated toward the chamber orifice, and the contours have spread somewhat indicating a decrease in the local current density. From experience with high-current density fronts propagating into ambient distributions of gas, this movement of the current front should be accompanied by a

sweeping of the ambient chamber gas toward the orifice. This is verified by the luminous concentration in the region near the cathode tip in Fig. 7-1b. In Fig. 7-4c, the contours have propagated out further but must be rapidly slowing since Figs. 7-4d through 7-4f exhibit a stabilized distribution of the current contours from 30 μ sec until the end of the pulse. The completion of the expulsion sequence of the initial ambient gas proceeds downstream of these contours as shown in the corresponding Kerr-cell frames.

The stabilized configuration displayed in Fig. 7-4f, exhibits several characteristic features:

1. Unlike most pulsed plasma accelerators where the luminosity provides a good indication of the high-current density regions, comparison of Fig. 7-1 with Fig. 7-4 reveals that there is little correlation here between the exhaust plume luminosity and the current pattern. In fact, the most luminous region (near the cathode tip) appears to coincide with only about 10 percent of the total current.

2. No significant amount of current extends more than one orifice diameter into the exhaust plume, either radially or axially.

3. Only that portion of the current which is attached to the cathode tip appears to bow out through the orifice and attach to the downstream edge of the anode.

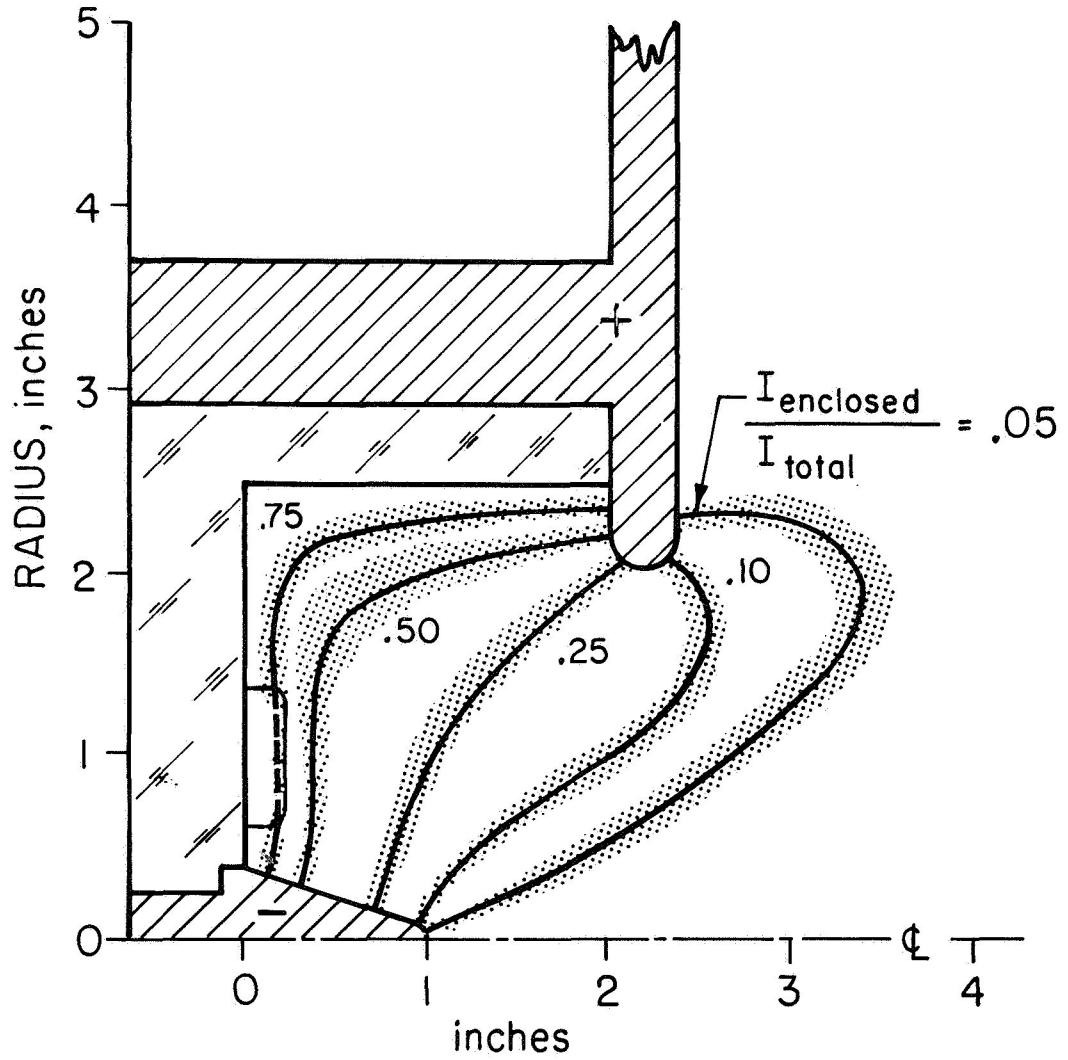
4. The remaining majority of the current chooses to distribute itself nearly uniformly throughout the arc chamber.

5. The entire exposed cathode surface participates in

the current conduction process. Estimates of the cathode surface local current density based on the measured contour locations indicate that this value is constant to within a factor of two.

The uncertainty in positioning the contours of enclosed current is shown in Fig. 7-5 for the stabilized discharge at a current of 4.4 kA and a mass flow rate of 36.0 g/sec. This uncertainty, shown by the shaded band surrounding the heavy contour line, represents the cumulative effect of shot-to-shot irreproducibility and the accuracy with which the data can be reduced from the oscilloscope traces. As indicated by Fig. 7-3b, a similar figure drawn for the transient phase would have wider (but not overlapping) uncertainty bands, especially in the near exhaust region.

Varying the operating conditions from the example case shown in Fig. 7-4 influences both the transient phase and the later stabilized phase. As was observed with the Kerr-cell photographs, it is again the combination of current and mass flow rate which determine the extent of this effect, rather than either of these parameters individually. For conditions of low magnetic interaction parameter β , i.e., toward the lower right in Fig. 4-1, the transition occurs in the same way as described above, but requires a longer time. However, for conditions of high β , i.e., conditions where mass starvation effects may become evident, the transition phase consists of a relatively high-current front travelling far down the

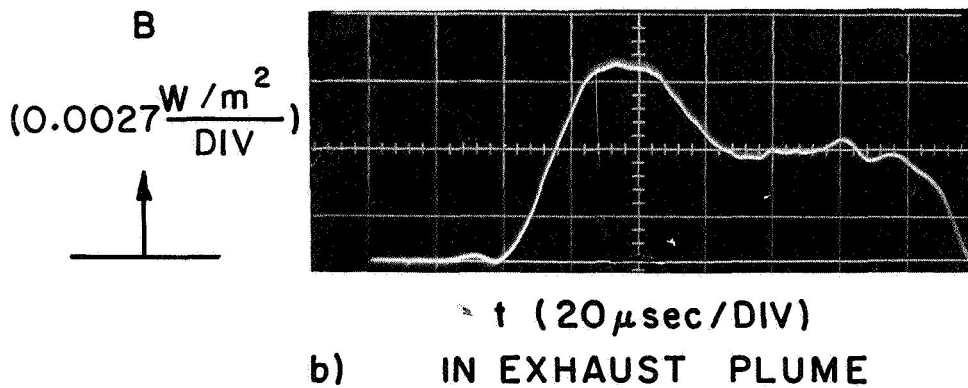
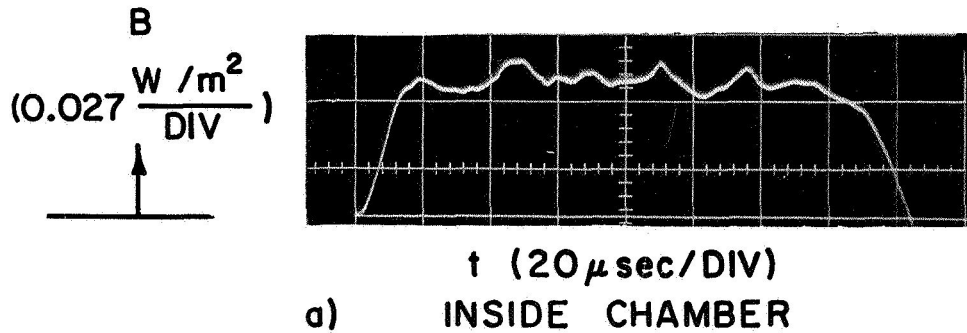


TYPICAL UNCERTAINTY IN STABILIZED CURRENT CONTOURS

$J = 4.4 \text{ kA}$, $\dot{m} = 36.0 \text{ g/sec}$

FIGURE 7-5

vacuum tank, unrolling behind it the lower current profiles characteristic of the stabilized state. The probe records of Fig. 7-6, taken with a total current of 17.5 kA and a mass flow rate of 1.2 g/sec, exhibit the magnetic field history for this type of transition. Inside the arc chamber, Fig. 7-6a, the magnetic field is less steady indicating the increased difficulty experienced by the discharge in conducting the necessary current, but the trace shows essentially the same behavior as in Fig. 7-3a where the mass flow rate was nearly 5 times greater. Out in the exhaust plume, however, the character of the signal has changed from a monotonic increase to the plateau value (Fig. 7-3b), to a large overshoot followed by a decay to the plateau value (Fig. 7-6b). These exhaust plume field histories were not recorded at the same position, which accounts for the difference in the arrival time of the signal. This overshoot type of transition manifests itself in the form of enclosed current contours which propagate rapidly both axially and radially along the anode face, overshoot their eventual equilibrium positions outside the chamber, and slowly return to them in a retrograde direction. For very high β conditions, the exhaust plume contours do not completely return to their equilibrium positions by the time of current reversal. However, even in this case, the contours in the arc chamber and near exhaust region, which constitute the majority of the total current, are stable so that the difference in the stabilized configuration for different operating conditions can be determined.



TYPICAL MAGNETIC FIELD HISTORIES IN
 ACCELERATOR DISCHARGE FOR MASS STARVATION

$$J = 17.5 \text{ kA}, \dot{m} = 1.2 \text{ g/sec}$$

The observations regarding the stabilized current distribution in Fig. 7-4 are in general valid for these other operating conditions; only absolute amounts appear to vary. For example, only about 25 percent of the total current extends out the anode orifice for any running condition except for mass starvation cases where up to 50 percent can flow to the outside face of the anode. Low β conditions generally result in current contours slightly withdrawn into the chamber whereas high β conditions yield contours slightly more extended downstream into the plume. Finally, as mass starvation conditions are reached, the current distribution on the cathode surface becomes peaked toward the cathode tip.

IV. DISCUSSION

The Kerr-cell and magnetic probe data provide the information necessary to determine the durations of the remaining unknown time constants and thus establish the degree to which the accelerator operates in a true quasi-steady mode. The time to reach a stabilized phase, τ_s , has been shown to be 20 to 30 μ sec for the 17.5 kA x 160 μ sec pulse. This time increases as β decreases and vice versa, remaining approximately at 15 percent of the total pulse length for this particular capacitor bank. The time until the onset of thermionic emission, τ_c , has been shown by both the voltage measurements and Kerr-cell photographs to be less than 10 percent of the total pulse length.

The time necessary to get additional mass through the discharge region after the initial mass distribution has been disturbed by the transient phase, τ_F , is related to the position of the enclosed current contours during the transient and stabilized phases. Since the current conduction region fills the entire arc chamber at all times, then the injected gas immediately enters into the acceleration zone. From the plots of the enclosed current contours, this zone is approximately $6(10^{-2})$ m long. Thus, assuming an average velocity through the zone of $6(10^3)$ m/sec implies $\tau_F \approx 10 \mu\text{sec}$. In this respect, it may be regarded as fortuitous that the discharge fills the chamber avoiding a long path between injection orifice and acceleration zone. However, the residence of substantial current near the rear chamber insulator may in fact be due to the discharge searching for additional mass.

With all characteristic times now evaluated, it is apparent that for each pulse employed, there exists a particular interval, usually the second half of the pulse or greater, which fulfills all of the requirements set forth in Chap. 4 for quasi-steady accelerators.

It is interesting to note that in all cases, the entire exposed cathode surface participates in the discharge. Thus, for purposes of the analytical thrust relation used throughout, the effective radius of attachment is the maximum material radius. This is the value used in calculations related to the operating range map (Fig. 4-1) and the voltage data analysis.

Since the cathode radius appears to be artificially restricting the size of the cathode attachment, it is interesting to speculate that smaller diameter cathodes may lead to a greater electromagnetic thrust component due to the increase in the logarithmic radius ratio term. This approach may be limited by the rapidly decreasing surface area and therefore increasing local current density which may lead to more severe erosion.

CHAPTER 8

SUMMARY AND FUTURE WORK

I. SUMMARY

The trend of the steady-state MPD arc program toward intermittent higher power operation, and the simultaneous progression of pulsed plasma thrusters toward longer-pulse operation, provides a basis for development of a quasi-steady accelerator, as defined in Chapter 4. One motivation for such development is an indication of high efficiency for self-field electromagnetic acceleration in the high power density range. Equally attractive are the ability to probe such an intense discharge without cooling problems or space limitations, the possibility of observing the operating characteristics of an electromagnetic accelerator in the power range projected for future electric propulsion missions, and the study of quasi-steady thrust generation techniques in their own right.

To implement the quasi-steady accelerator has required the synchronization of tailored pulses of mass flow and current. A shock tube mass injection system has been developed which provides steady argon flow rates of up to 50 g/sec for 3 msec with a risetime of 1 msec. This latter technique

preserves a 10^{-5} torr pressure in the dielectric vacuum chamber which allows the mean free path to be greater than the tank dimensions. Flattop current pulses ranging from 138 kA x 20 μ sec to 4.4 kA for 600 μ sec are provided by a 132 μ farad capacitor bank whose triggering is delayed relative to the mass pulse by a special gas discharge switch.

The resulting arc discharge has been shown to lapse into an operating mode where all pertinent arc processes are essentially steady, i.e., the rapid propagation of intense sweeping current sheets typical of short-pulse accelerators is followed by a diffuse steady current pattern through which the injected mass is accelerated. For all current and mass flow combinations, the initial transient period occupies less than half of the total test time. In addition, voltage measurements and Kerr-cell photographs have indicated that thermionic emission of electrons from the cathode, typical of the steady state MPD arcs prevails throughout the quasi-steady phase.

Terminal voltage measurements and time-resolved magnetic field distributions have been valuable in determining the arc acceleration characteristics. In particular, the voltage measurements show a current and mass flow dependence which is not in agreement with analytical estimates based on the ideally anticipated voltage components. At low mass flow rates, this discrepancy may be attributed to the ingestion and reacceleration of extraneous mass, perhaps vaporized

from the electrodes or insulators. At high mass flow rates, the voltage displays an insensitivity to the mass flow which cannot be explained by an ion-neutral slip hypothesis like that commonly invoked for the steady state accelerators. The maximum efficiency, as calculated from the voltage measurements at the lowest mass flow before erosion and entrainment effects become important, is found to increase steadily over the observable range, reaching a value of about 25 percent at 17.5 kA.

Magnetic field measurements show that the stabilized current zone completely fills the arc chamber and covers the exposed cathode surface with a nearly uniform current density. Yet, little of this distribution spreads outside the anode orifice and virtually none extends beyond one orifice diameter either radially or axially.

II. FUTURE WORK

Based on these first studies on the quasi-steady accelerator facility, many additional experiments and extensions of the primary measurements suggest themselves:

1. The voltage measurements should be extended in several directions: First, because the ionization energy, particle mass, and molecular composition play an important role in some theories of the acceleration process [44,47], the same matrix of measurements performed on argon should be repeated with other gases, e.g., xenon, which has a lower

ionization energy, and nitrogen, which requires expenditure of the dissociation energy before ionization can be achieved. Second, the same voltage measurements should be extended to higher mass flow rates to see whether the voltage efficiency will continue to increase as shown in Fig. 6-10 or whether some fundamental limit will be reached. This will require a substantial modification to the mass injection system to provide an order of magnitude higher flow rates. Third, since it has been shown that the discharge attachment at the cathode covers the entire exposed surface area, installing a smaller diameter cathode should increase the thrust by virtue of the logarithmic term in the electromagnetic thrust equation. This should be reflected in an increase in the acceleration voltage component and therefore in the total voltage.

2. A most important measurement for evaluating the acceleration characteristics is the exhaust velocity. If this could be determined for the various accelerated species, e.g., A^+ , A^{++} , A^0 , etc., it could resolve the contention of species coupling in the exhaust, indicate the severity of erosion, and provide independent information on the thrust. Steady state experiments are limited by their inability to install a probe directly in the exhaust plume. Thus, the measurement of velocity in these facilities is typically attempted by a) time of flight of plasma fluctuations between two optical sensors, which may not represent the actual

streaming velocity, b) the measured thrust divided by the supplied mass flow rate, which automatically incorporates any spurious effect caused by entrainment or erosion, and c) a Doppler shift determination involving large experimental apparatus and long exposure times. In the quasi-steady case, several other methods of velocity measurement may be considered, none of which can be simply applied. One of these is an ion energy analyzer, which consists of a gridded electric probe which screens out electrons and measures the flux of ions having an energy greater than an applied potential. The probe must be carefully designed, since limitations on grid spacings are determined by the local plasma properties. A second method consists of measuring the local $\vec{u} \times \vec{B}$ voltage generated by the ejected particle stream species passing through a small applied magnetic field, but here again, care must be exercised to maintain the plasma disturbance at a minimum. Attempts at time-resolved Doppler shift methods for velocity determination involve Kerr-cell shutters to expose the spectrographic equipment only during the stabilized phase, and it is highly questionable that sufficient light is available for the necessary short exposures.

3. The effect of electrode geometry on the voltage efficiency can be studied systematically. As discussed previously, the efficiency is related to the profile of E-UB through the acceleration zone, since JE-JUB represents

the energy dissipated electrothermally. Since U is small at the inlet to the acceleration zone, and B is small at the outlet, the profile of UB must be peaked. Thus, for high efficiency, E should also be peaked. The effect of empirical variation of the electrode geometry, by altering size of electrodes, anode to cathode spacing, and chamber and orifice configurations, can be monitored by the same sequence of measurements pursued earlier. Note that the present configuration may itself be one of relatively high efficiency since its electrostatic field profile has the desired characteristics of low magnitude at the inlet and outlet portions of the flow. This problem of electrode geometry optimization may also provide some interesting analytical possibilities, since there is an essential non-linearity associated with the establishment of the actual profiles of u , j , B , and E .

4. As the accelerator progresses toward a useful thruster, direct measurement of thrust becomes more imperative. This measurement is not only important for correlating the velocity and mass flow values for the steady phase, but also for determining the overall impulse bit when investigating the optimum quasi-steady accelerator. Thrust measurement for a small total impulse system usually involves a sophisticated counterbalanced pendulum or null-suspension, where extreme care must be taken to negate all disturbances from the electrical,

mechanical, and gas-flow connections, and from spurious interactions between the electromagnetic fields and the test facility [79]. Recently, a technique which utilizes a piezo crystal as the thrust transducer has been developed which may also be serviceable for this purpose [87].

REFERENCES

1. Marshall, J., "Performance of a hydromagnetic plasma gun," *The Phys. Fluids* 3, 134-135 (January-February 1960).
2. Gorowitz, B., Karras, T. W., and Gloersen, P., "Performance of an electrically triggered repetitively pulsed coaxial plasma engine," *AIAA J.* 4, 1027-1031 (June 1966).
3. Larson, A. V., Gooding, T. J., Hayworth, B. R., and Ashby, D. E. T. F., "An energy inventory in a coaxial plasma accelerator driven by a pulse line energy source," *AIAA J.* 3, 977-979 (May 1965).
4. Jahn, R. G., and von Jaskowsky, W., "Structure of a large-radius pinch discharge," *AIAA J.* 1, 1809-1814 (August 1963).
5. Jahn, R. G., and von Jaskowsky, W., "Current distributions in large-radius pinch discharges," *AIAA J.* 2, 1749-1753 (October 1964).
6. Burton, R. L., and Jahn, R. G., "Acceleration of plasma by a propagating current sheet," *The Phys. Fluids* 11, 1231-1237 (June 1968).
7. Duclos, D. P., Aronowitz, L., Fessenden, F. P., and Cartensen, P. B., "Diagnostic studies of a pinch plasma accelerator," *AIAA J.* 1, 2505-2513 (November 1963).
8. Glasstone, S., and Lovberg, R. H., Controlled Thermonuclear Reactions (D. Van Nostrand Co., Princeton, N. J., 1960) Chap. 7.
9. Jahn, R. G., von Jaskowsky, W., and Burton, R. L., "Ejection of a pinched plasma from an axial orifice," *AIAA J.* 3, 1862-1866 (October 1965).
10. "Dynamics of a pinch discharge driven by a high-current pulse-forming network," Ph.D. Thesis of N. A. Black, Aeronautical Engineering Report No. 778, Department of Aerospace and Mechanical Sciences, Princeton University, May 1966.
11. Hayworth, B. R., White, C. W., and Miller, A. R., "Energy storage capacitors for pulsed plasma thrusters," *J. Spacecraft and Rockets* 3, 1534-1536 (October 1966).
12. Eckbreth, A. C., Clark, K. E., and Jahn, R. G., "Current pattern stabilization in pulsed plasma accelerators," *AIAA J.* 6, 2125-2132 (November 1968).
13. Ducati, A. C., Giannini, G. M., and Muehlberger, E., "Experimental results in high-specific-impulse thermo-ionic acceleration," *AIAA J.* 2, 1452-1454 (August 1964).

REFERENCES-contd.

14. Grossman, W., Hess, R. V., and Hassan, H. A., "Experiments with a coaxial Hall current plasma accelerator," AIAA J. 3, 1034-1039 (June 1965).
15. John, R. R., Bennett, S., and Connors, J. F., "Experimental performance of a high-specific impulse arcjet engine," AIAA Paper 64-669 (September 1964).
16. Cann, G. L., and Harder, R. C., "Follow-on investigation of a steady state Hall current accelerator," Report No. NAS CR-54062 (30 October 1964).
17. Patrick, R. M., and Schneiderman, A. M., "Performance characteristics of a magnetic annular arc," AIAA J. 4, 283-290 (February 1966).
18. Brown, H., and Coates, G. L., "Application of nuclear electric propulsion to manned Mars mission," J. Spacecraft and Rockets 3, 1402-1408 (September 1966).
19. "Low acceleration space transportation system study," Final Report, Volume II: Technical Report, GE-ANSO Document No. 6300-260-2, October 1967.
20. Masey, A. C., Dugan, D. W., and Pitts, S. W., "Applications of combined electric, high-thrust propulsion systems," J. Spacecraft and Rockets 5, 785-791 (July 1968).
21. Black, N. A., and Jahn, R. G., "Dynamic efficiency of pulsed plasma accelerators," AIAA J. 3, 1209-1210 (June 1965).
22. Demetriades, S. T., Hamilton, G. L., Ziemer, R. W., and Lenn, P. D., "Three fluid nonequilibrium plasma accelerators," Progress of Astronautics and Aeronautics: Electric Propulsion Development (Ed. E. Stuhlinger) Vol. 9, p. 461, Academic Press, New York (1963).
23. Clark, K. E., and Jahn, R. G., "The magnetoplasmadynamic arcjet," Astronautica Acta 13, 315-325 (1967).
24. Nerheim, N. M., and Kelly, A. J., "A critical review of the state-of-the-art of the MPD thruster," AIAA Paper 67-688 (1967).
25. Noeske, H. O., "The coaxial MPD engine, a state-of-the-art review," AIAA Paper 66-242 (1966).
26. John, R. R., Bennett, S., and Connors, J. F., "Arcjet engine performance: experiment and theory," AIAA J. 1, 2517-2525 (1963).

REFERENCES-contd.

27. Hess, R. V., "Experiments and theory for continuous steady acceleration of low density plasmas," Proceedings of XI International Astronautical Congress, Springer-Verlag, Berlin, 1960.
28. Powers, W. E., and Patrick, R. M., "Magnetic annular arc," The Phys. Fluids 5, 1196-1206 (1962).
29. Patrick, R. M., and Powers, W. E., "Plasma flow in a magnetic arc nozzle," Third Symposium on Advanced Propulsion Concepts, Cinn., Ohio, October 1962. Gordon and Breach, New York, 1963, Vol. 1, 115-136.
30. Ducati, A. C., private communication.
31. Ducati, A. C., Giannini, G. M., and Muehlberger, E., "Recent progress in high-specific impulse thermo-ionic acceleration," AIAA Paper 65-96 (1965).
32. Arcjet technology research and development, Avco Corp., Research and Advanced Development Division, RAD-TR-65-37 (December 1965).
33. Mastrup, F. N., "Spectroscopic investigation of a hydrogen arcjet plume," AIAA J. 5, 159-161 (1967).
34. Jones, R. E., "Results of large vacuum facility tests of an MPD thruster," AIAA J. 4, 1455-1456 (1966).
35. Connolly, D. J., Sovie, R. J., Michels, C. J., and Burkhart, J. A., "Low environmental pressure MPD arc jets," AIAA J. 6, 1271-1276 (1968).
36. Cann, G. L., Harder, R. L., Moore, R. A., and Lenn, P. D., "Hall current accelerator," Electro-Optical Systems, EOS Report 5470-Final (February 1966).
37. Powers, W. E., "Measurements of the current density distribution in the exhaust of an MPD arcjet," AIAA J. 5, 545-550 (1967).
38. Larson, A. V., "Experiments on current rotations in an MPD engine," AIAA J. 6, 1001-1006 (1968).
39. Malliaris, A. C., "Oscillations in an MPD accelerator," AIAA J. 6, 1575-1577 (1968).
40. Hugel, H., Kruelle, G., and Peters, T., "Investigations on plasma thrusters with thermal and self-magnetic acceleration," AIAA J. 5, 551-558 (1967).

REFERENCES-contd.

41. Kelly, A. J., Nerheim, N. J., and Gardner, J. A., "Electron density and temperature measurements in the exhaust of an MPD source," AIAA J. 4, 291-295 (1966).
42. Hugel, H., "Self-magnetic effect in arcjet engines," AIAA J. 6, 1573-1575 (August 1968).
43. Jahn, R. G., Physics of Electric Propulsion, McGraw-Hill Book Company, New York, 1968, Chap. 8.
44. Stratton, T. F., "High current steady state coaxial plasma accelerators," AIAA J. 3, 1961-1963 (1965).
45. Jahn, R. G., "An electron's view of the MPD arcjet," Giannini Scientific Corp. Technical Report 5QS085-968 (August 1965).
46. Moore, R. A., Cann, G. L., and Gallagher, L. R., "High specific impulse thermal arc jet thruster technology," TR No. AFAPL-TR-65-48, Air Force Aero Propulsion Laboratory, June 1965, (EOS 5090-Phase I Final).
47. Bennett, S., John, R. R., Enos, G., and Tuchman, A., "Experimental investigation of the MPD arcjet," AIAA Paper 66-239 (1966).
48. Malliaris, A. C., and Libbey, D. R., "Velocities of neutral and ionic species in an MPD flow," AIAA Paper 69-109 (1969).
49. Fahleson, U. V., "Experiments with plasma moving through neutral gas," The Phys. Fluids 4, 123-127 (1961).
50. Alfven, H., "Collision between a nonionized gas and a magnetized plasma," Rev. Mod. Phys. 32, 710-713 (1960).
51. Lin, S. C., "Limiting velocity for a rotating plasma," The Phys. Fluids 4, 1277-1287 (1961).
52. Gloersen, P., Gorowitz, B., and Kenney, J. T., "Energy efficiency trends in a coaxial gun plasma engine," AIAA J. 4, 436-441 (March 1966).
53. Michels, C. J., Heighway, J. E., and Johansen, A. E., "Analytical and experimental performance of capacitor powered coaxial plasma guns," AIAA J. 4, 823-830 (May 1966).
54. Ashby, D. E. T. F., Gooding, T. J., Hayworth, B. R., and Larson, A. V., "Exhaust measurements on the plasma from a pulsed coaxial gun," AIAA J. 3, 1140-1142 (June 1965).
55. Lovberg, R. H., "Investigation of current-sheet microstructure," AIAA J. 4, 1215-1222 (July 1966).

REFERENCES-contd.

56. "Structure of the current sheet in a pinch discharge," Ph.D. Thesis of R. L. Burton, Aerospace and Mechanical Sciences Report No. 783, Princeton University, September 1966.
57. Gooding, T. J., Hayworth, B. R., and Lovberg, R. H., "Instabilities in a coaxial plasma gun," AIAA J. 1, 1289-1292 (June 1963).
58. Ashby, D. E. T. F., Liebing, L., Larson, A. V., and Gooding, T. J., "Quasi-steady-state pulsed plasma thrusters," AIAA J. 4, 831-835 (May 1966).
59. Jahn, R. G., and von Jaskowsky, W., "Pulsed electromagnetic gas acceleration," Aerospace and Mechanical Sciences Report No. 634d, Princeton University, July 1964.
60. Ashby, D. E. T. F., Gooding, T. J., Hayworth, B. R., and Larson, A. V., "Development of a coaxial plasma gun for space propulsion," General Dynamics/Convair Report CR-54245, Contract NAS 3-5759 (April 1965).
61. Ekdahl, C., Kribel, R., and Lovberg, R., "Internal measurements of plasma rotation in an MPD arc," AIAA Paper 67-655 (September 1967).
62. Jahn, R. G., von Jaskowsky, W., and Casini, A. L., "Gas-triggered pulse discharge switch," Rev. Sci. Instr. 36, 101 (1965).
63. von Engel, A., Ionized Gases, chap. 7, p. 172, Oxford University Press, Fair Lawn, N. J., 1955.
64. Schonhuber, J., "Breakdown below (Pd) min.," in Proceedings of the Seventh International Conference on Phenomena in Ionized Gases, Beograd 1965, I, 316-326, Grodevinska Knijga Publishing House, Beograd 1966.
65. Lovberg, R., "Magnetic probes," chap. 3 in Plasma Diagnostic Techniques, Huddleston, R. H., and Leonard, S. L. (eds.), Academic Press, New York, 1965.
66. Jahn, R. G., and Clark, K. E., "A large dielectric vacuum facility," AIAA J. 4, 1135 (June 1966).
67. "Current pattern and gas flow stabilization in pulsed plasma accelerators," Ph.D. Thesis of A. C. Eckbreth, Aerospace and Mechanical Sciences Report No. 857, Princeton University, December 1968.
68. Gooding, T. J., Maxwell Labs., Inc., San Diego, Calif., private communication.

REFERENCES-contd.

69. Valsamakis, E. A., "Ionization gauge for transient gas pressure measurements," *Rev. Sci. Instr.* 37, 1318-1320 (1966).
70. Karras, T., Gorowitz, B., and Gloersen, P., "Neutral mass density measurements in a repetitively pulsed coaxial plasma accelerator," *AIAA J.* 4, 1366-1369 (August 1966).
71. Jahn, R. G., and von Jaskowsky, W., "Pulsed electromagnetic gas acceleration," *Aerospace and Mechanical Sciences Report No. 634h*, Princeton University, January 1967.
72. "Energy transfer from a pulse network to a propagating current sheet," Ph.D. Thesis of P. J. Wilbur, *Aerospace and Mechanical Sciences Report No. 846*, Princeton University, September 1968.
73. Hayworth, B. R., Gooding, T. J., and Larson, A. V., "A pulse-line energy source for plasma accelerators," *Proc. 5th Symp. on Eng. Aspects of Magnetohydrodynamics*, M.I.T., p. 131 (1964).
74. Glass, I. I., and Hall, J. G., Shock tubes, *Handbook of Supersonic Aerodynamics*, Sec. 18, NAVORD Report 1488 (Vol. 6) December 1959.
75. "Pressure distribution in the structure of a propagating current sheet," Ph.D. Thesis of T. M. York, *Aerospace and Mechanical Sciences Report No. 853*, Princeton University, December 1968.
76. Milligan, M. W., "Nozzle characteristics in the transition regime between continuum and free molecular flow," *AIAA J.* 2, 1088-1092 (June 1964).
77. Malliaris, A. C., "Plasma acceleration in an electrical discharge by the self-induced magnetic field," *J. Appl. Phys.* 38, 9, 3611-3619 (August 1967).
78. Leonard, S. L., "Basic macroscopic measurements," in Plasma Diagnostic Techniques, edited by Huddleston, R. H., and Leonard, S. L., Academic Press, New York, 1965.
79. Guman, W. J., "Pulsed plasma technology in microthrusters," *Technical Report AFAPL-TR-68-132*, November 1968.
80. Oberth, R. C., Princeton University, private communication.
81. Malliaris, A. C., "Interaction of a high current electrical discharge with its self-induced magnetic field in the presence of gas flow," *ARL Report No. 67-0007*, January 1967.
82. Ducati, A. C., Jahn, R. G., Muehlberger, E., and Treat, R. P., "Exploratory electromagnetic thruster research," *Giannini Report No. TR 117-1513*, February 1968.

REFERENCES-contd.

83. Guman, W. J., and Truglio, W., "Surface effects in a pulsed plasma accelerator," AIAA J. 2, 1342-1343 (July 1964).
84. Kogelschatz, U., "Doppler shift measurements of axial and rotational velocities in an MPD arc," AIAA Paper 69-110 (1969).
85. Cambel, A. B., Plasma Physics and Magnetofluidmechanics, McGraw-Hill Book Company, New York, 1963, Chap. 7.
86. Nighan, W. L., "Electrical conductivity of partially ionized noble gases," The Phys. Fluids 12, 162-171 (January 1969).
87. Gilmour, S., Electro-Sciences Div., Sanders Associates, Inc., Buffalo, New York, private communication.